Integration of photoactivated molecular motors in complex systems for the development of active materials

Joakim Heiser

UNIVERSITÉ DE STRASBOURG

ÉCOLE DOCTORALE 222

UPR 22

THÈSE présentée par :

HEISER Joakim

soutenue le : **27 septembre 2021**

pour obtenir le grade de : **Docteur de l'université de Strasbourg**

Discipline/ Spécialité : Chimie moléculaire- chimie supramoléculaire

Intégration de moteurs moléculaires photo-activés dans des systèmes complexes pour le développement de matériaux actifs

THÈSE dirigée par :

M. GIUSEPPONE Nicolas	Professeur, Université de Strasbourg, France
Mme. MOULIN Émilie	Directeur de Recherche, CNRS, France

RAPPORTEURS :

Mme. SILVI Serena	Professeur associé, Université de Bologne, Italie
M. VIVES Guillaume	Maître de conférences, Sorbonne Université, France

Table of Content

Acknowledgements

I would like to thank Prof Nicolas Giuseppone and Dr Emilie Moulin, my thesis supervisors, for giving me the opportunity to work with them in the SAMS team. Their supervision allowed me to complete this thesis but also to learn a lot about the world of research, thus pushing me to pursue this path towards a PostDoc. I hope to have the opportunity to work with you again in the future.

I would also like to thank the two members of my thesis jury, Prof Serena Silvi and Dr Guillaume Vives, for taking the time to review my work. Their feedback was constructive and our conversation during the defence very interesting.

In particular, I would like to acknowledge Dr Andreas Vargas Jentzsch who was always available to discuss and share his knowledge. He is not only a table companion with whom one can discuss for hours, but also someone one can rely on to move forward.

I would like to thank my collaborators Dr Madeline Vauthier and Prof Eric Buhler for always being available for my problems and for answering my questions, thus allowing me to become familiar with their respective fields of research.

My thanks also go to Odile Gavat and Marie-Céline Samy-Arlaye for making the impossible possible with their help, expertise and daily presence.

I would also like to warmly thank the SAMS group as a whole, with more and more members from all over the world. I was able to have great discussions, share moments of conviviality and receive constant support. This adventure would not have been the same without you.

Special mention to Nicolas Capit who worked hard to find me incredible presents for the thesis potluck, I wish him good luck for the writing of his manuscript. To Alexis for our fruitful collaboration in the multi-gram synthesis of the molecular engine that gave us a hard time. To Christian and Raphaël for all our discussions where we remade the world. Finally, thanks to Martin Power whom I had the pleasure to supervise.

Finally, I would like to thank my family for always supporting me and believing in me, especially my incredible wife, without whom I would certainly not have got this far.

Abstract

In the race for miniaturisation, the development of molecular machines represents a major challenge. The discovery in 1999 by the group of Feringa of the unidirectional light-fuelled rotary molecular motor has been ground-breaking. This system based on a crowded alkene is remarkable i) for its autonomy, as it only needs to be irradiated in order to operate continuously, ii) for its rotation speed, which can reach the MHz range, and iii) for its ability to be integrated into complex materials (liquid crystal, MOF, ...), as it can be easily functionalised. One of the major issue remains the amplification of the motion generated by the rotation of the motor from the nanoscopic to the macroscopic scale. In this context, our team achieved to develop a contractile chemical gel integrating tetrafunctionalized molecular motors used as cross-linking centres and linked to each other by polymer chains. This system is thus capable of contracting under UV irradiation by twisting pairs of polymer chains together and storing the work produced by the motors in the form of tension. The aim of this thesis consisted in broadening the field of application of this tetra-functionalized motor by focusing on three axes.

The first one consisted in scaling-up the synthesis of the tetrafunctionalized and orthogonally protected molecular motor in order to facilitate its obtention. We managed to form 40 g of products in more than 12 synthetic steps.

The second one was to limit the degradation of our systems and to pave the way for the development of more complex structures integrating new modulating units, that were previously incompatible with UV irradiation, by seeking to increase the wavelength used during the irradiation of our gels. To do so, we studied the impact of adding a porphyrin-based photosensitizer to our molecular motors, first in solution and then in gel. We demonstrated that a triplet energy transfer did take place between the motor and the photosensitizer, which allowed us to carry out the first gel contractions using visible light.

Finally, the third axis focused on the development of a new mode of propulsion for nano-swimmers based on the rotation of molecular motors attached on the surface of nano-objects. To this end, we first developed and then characterised Janus nanoparticles functionalised by our motors. We demonstrated the formation of electrostatic interactions between the surface of the particles and the motors by using Zeta potential measurements and fluorescence experiments. Finally, the preliminary results using static light scattering experiments showed the existence of a ballistic component in the movement of these objects under UV irradiation.

Abbreviations and Symbols

°	degree
°C	degree Celsius
A	adenine
Ac	acetate
ATP	adenosine triphosphate
BBr_3	boron tribromide
c	concentration
C	cytosine
Cal	calorie
$CBPQT^{4+}$	cyclobis(paraquat-*p*-phénylène) tétracationique
$CDCl_3$	deuterated chloroform
CD_3OD	deuterated methanol
CH_2Cl_2	dichloromethane
C_x	carbon number x
cm	centimetre
CMP	Chimie Macromoléculaire de Précision
CuBr	Copper bromide
D_H	diffusion coefficient
dA	deoxyribonucleotide
Da	dalton
DCE	dichloroethane
DCM	dichloromethane
DIAD	diisopropyl azodicarboxylate
DMF	*N*,*N*-dimethylformamide
DNA	deoxyribonucleic acid
DFT	density functional theory
DLS	dynamic light scattering
dn/dc	refractive index over concentration
EDC	1-ethyl-3-(3-dimethylaminopropyl) carbodiimide
eq	equilibrium
eq.	equivalent
Et	ethyl
ET	energy transfer
EtOAc	ethyl acetate
EtOH	ethanol
Et_3N	triethylamine
e^-	electron
Fmoc	fluorenylmethoxycarbonyl
g	gram
G	guanine
h	hour
HCl	hydrochloric acid

HOBt	hydroxybenzotriazole
hν	photon
HOMO orbital	highest occupied molecular
HPLC	high performance liquid chromatography
Hz	hertz
H^+	proton
H_2O	water
I	scattered intensity
I_f	scattered intensity
I_f^0	initial intensity
ICS	Institut Charles Sadron
ISC	intersystem crossing
iso	isomerization
iPr_3Si	tris(triisopropylsilyl)silane
J	coupling constant
JNPs	Janus nanoparticles
K	kelvin
k	kilo
k_q	extinction coefficient
k_x	rate constant of x
kCal	kilocalorie
$KHCO_3$	potassium bicarbonate
kHz	kilohertz
kJ	kiloJoul
K_2CO_3	potassium carbonate
L	litre
l	length
LC	liquid crystal
LCE	liquid crystalline elastomer
LED	light emitting diode
LMSC	Laboratoire Matière et Systèmes Complexes
LUMO	lowest unoccupied molecular orbital
M	molar
m	metre
Me	methyl
MeI	methyl iodide
MeOH	methanol
Me_3SnOH	trimethyltin hydroxide
MHz	megahertz
mg	milligram
min	minute
mins	minutes
mL	millilitre
mm	millimetre
mM	millimolar
mmol	millimolar
MnO_2	manganese dioxide
mol	molar
mol.%	molar fraction

ms	millisecond
MS	mass spectrometre
mV	millivolt
mW	milliwatt
MW	microwave
M_W	molar weigh
n	number of
n-BuLi	*n*-butyllithium
NaN_3	sodium azide
NaOH	sodium hydroxide
Na_2SO_4	sodium sulfide
nm	nanometre
NMR	nuclear magnetic resonance
NH_2NH_2	hydrazine
NP	nanoparticles
Ns	nanosecond
P	irradiation power
pA	picoampere
PD	polydispersity
Pd	palladium
$Pd(OAc)_2$	palladium(II)-acetate
Pd-TPP	palladium(II)-tetraphenylporphyrin
PEG	polyethylene glycol
PF_6^-	hexafluorophosphate
PLGA	poly(lactic-co-glycolic acid)
PMB	*para*-methoxy benzyl
PMDTA	pentamethyl-diethylenetriamine
PPA	polyphosphoric acid
PPh_3	triphenylphosphine
ppm	part-per-million
PSS	polystyrene sulphonate
P_2S_5	phosphorous pentasulfide
q	scattering wave vector
rA	ribonucleotide
ref	reference
redox	reduction-oxidation
R_G	average radius of gyration
RNA	ribonucleic acid
RT	room temperature
s	second
S_x	singlet excited stated number x
SAMS	Synthèse et Auto-assemblage Moléculaires et Supramoléculaires
s-BuLi	*sec*-butyllithium
$SOCl_2$	thionyl chloride
SLS	static light scattering
STM	scanning tunnelling microscope
T	temperature
T	thymine
T_1	first triplet excited state
TBAF	tetrabutylammonium fluoride
TBDMS	*tert*-butyldimethylsilyl

TBS	*tert*-butyldimethylsilyl
*t*Bu	*tert*-butyl
TEG	triethylene glycol
TEM	transmission electron microscopy
THF	tetrahydrofuran
TLC	thin layer chromatography
TMEDA	tetramethylethylenediamine
TPP	tetraphenylporphyrin
Ts	tosyl
UPLC	ultra-performance liquid chromatography
UV	ultra-violet
V	volt
Vis	visible
vs.	versus
W	watt
wt.%	weight fraction
δ	chemical shift
Δ	heating
ΔG	Gibbs energy
λ	wavelength
θ	measurement angle
µg	microgram
µL	microlitre
µm	micrometre
µM	micromolar
µHz	microhertz
µmol	micromolar
τ	life-time
[X]	concentration of compound X

General Introduction and Objectives

Feringa's molecular motor consists of a crowded alkene capable of unidirectional rotational motion when placed under light irradiation. This system is particularly interesting as it generates continuous work as long as it is supplied with energy. Since it has been published in 1999 (**Figure 1.A**),[1] it has been at the heart of a tremendous race to develop new structures,[2,3] which are increasingly fast (up to MHz) and complex.[4] Its incredible potential for the elaboration of new photo-active materials and the simplicity of its design were awarded by a Nobel Prize in Chemistry in 2016.[5] Today, many systems have been developed, but one of the major challenges remains the use and storage of the work that this motor unit is capable of producing. Indeed, as long as this machine remains isolated in solution, no work can be collected. It is therefore essential to integrate it into a larger structure in order to take full advantage of the displacement generated. It is in this context that our team succeeded in developing a chemical gel in which tetrafunctionalized molecular motors are linked to each other by polymer chains while serving as cross-linking points (**Figure 1**.**B**).[6] Thus, upon UV irradiation, rotary molecular motors will generate a winding of pairs of polymer chains which results macroscopically in a contraction of the material. This approach therefore enables the work to be stored via an increase in the tension of the chains, but does not allow it to be recovered unless a covalent bond in the system is irreversibly broken. The solution developed by our team consists of adding a so-called modulator unit based on tetrafunctionalized diarylethene (**Figure 1.C**).[7] Indeed, this modulator, also used as a cross-linking centre, is capable, under visible light, of setting up axes of free rotation allowing the unwinding of the polymer chains and thus a return of the material to its original form.

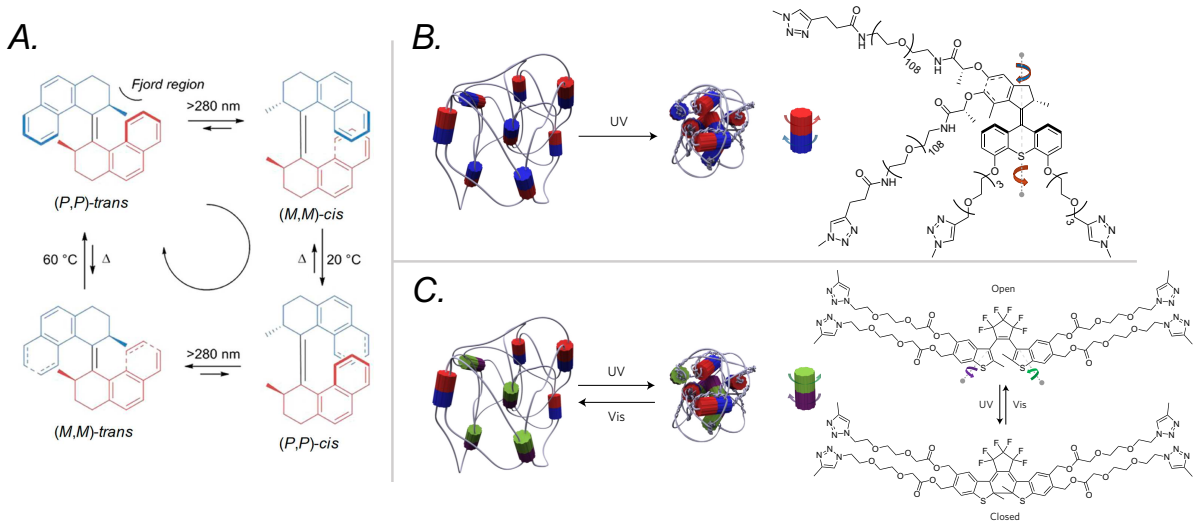

Figure 1. A. Molecular structure and mechanism of the first alkene-based motor. Adapted from ref 1. Scheme of an irreversible **B.** and reversible **C.** contractile gel bearing respectively the corresponding tetrafunctionalized molecular motor and diarylethene-based modulator. Adapted from ref 6 and 7.

The aim of this thesis is in the continuity of the work carried out by our team and can be divided into three main areas.
The first one consisted in the large-scale synthesis of the tetrafunctionalized and orthogonally protected molecular motor (**Figure 2**). It was therefore a question of taking the protocols already developed and published in order to push them even further, with the objective of synthesizing 40 g of final product ready to be used.[8]

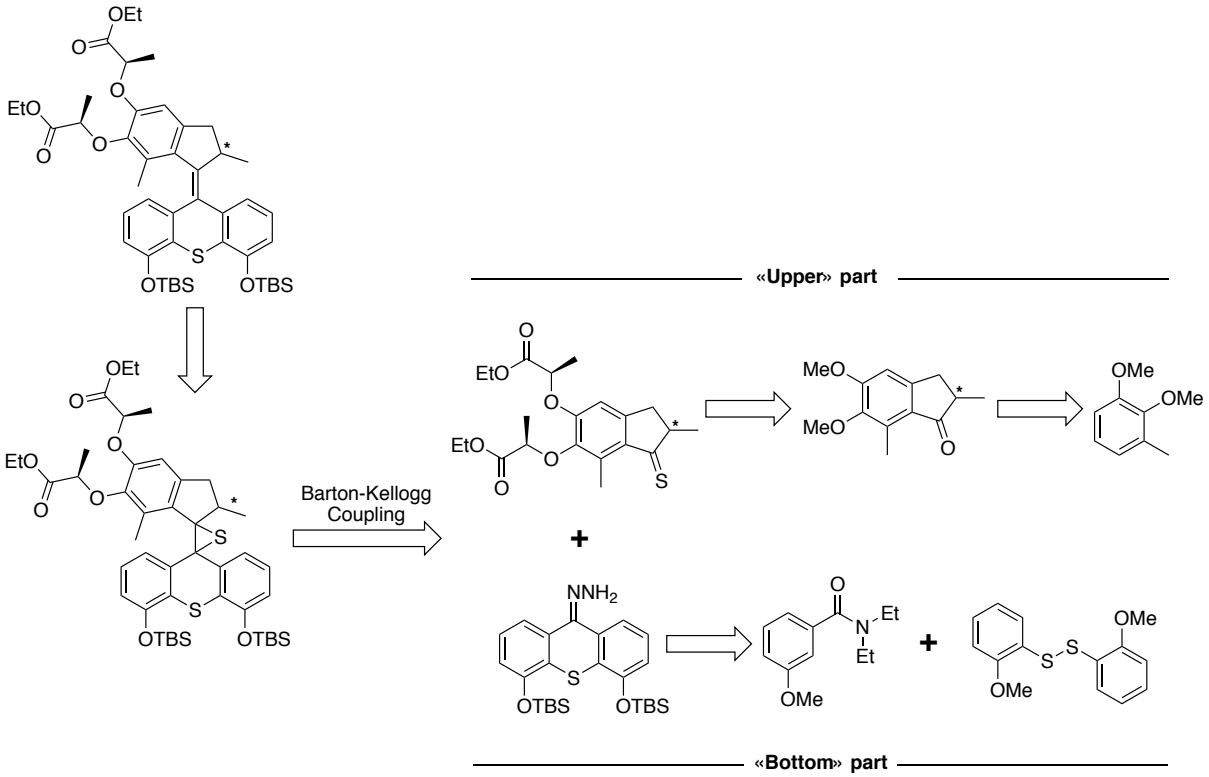

Figure 2 Retrosynthetic scheme of the tetrafunctionalized molecular motor.

The second part focused on pursuing the research on the contractile gel by seeking to increase the wavelength of irradiation so as to avoid the use of UV light in order to limit degradation and to widen the field of usable modulators. The work of the group of Feringa has been of great help in this respect, as it has already been demonstrated that a molecular motor is capable of functioning via energy transfer from a porphyrin-based photosensitizer (**Figure *3*A**).[9] Thus, my objective was to study the application of this approach to our system and to investigate the influence of different parameters such as light intensity and photosensitizer concentration on the contraction rate.
Finally, the last part of the project enlarged this initial topic by coupling our molecular motors polymer conjugates to access nano-swimmers. This project is the result of a collaboration between organic chemists, polymer chemists and physicists (SAMS and CMP Strasbourg, LMSC Paris) and aims to implement a novel form of propulsion by functionalizing Janus nanoparticles with molecular motors (**Figure 3B**). The main idea consists in taking advantage of their rotation[10] so as to induce a ballistic motion similar to that of living micro-organisms.[11] Here,

we will look at the development of these structures and then detail all the characterisations that have been carried out to determine the properties of these systems.

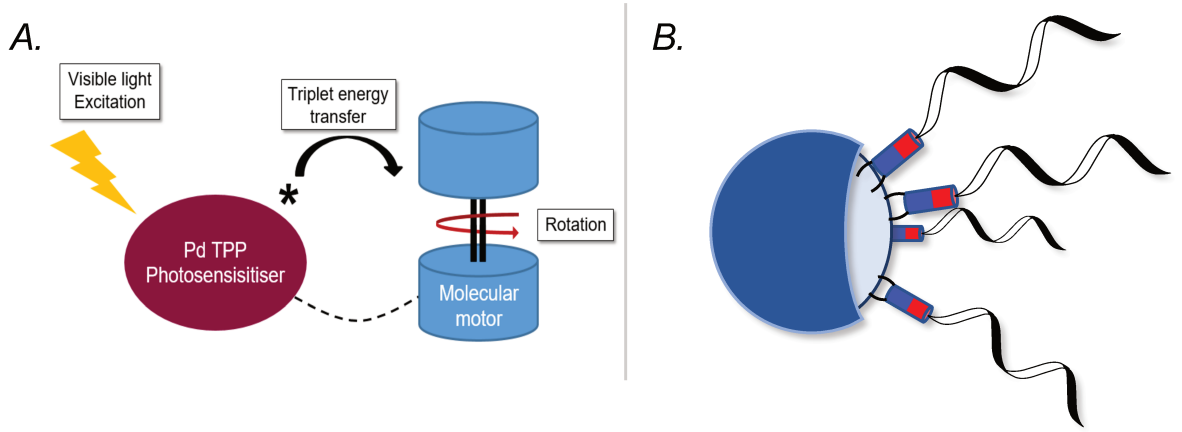

Figure 3. A. Schematic representation of the energy transfer from the porphyrin-based photosensitizer towards the motor. Adapted from ref 9. **B.** Scheme depicting the design of the propeller based on Janus particle functionalized by molecular motors bearing helical polymer chains.

Chapter I. Bibliographic Introduction

Since the development of the first steam engine in 1712 by Thomas Newcomen, the emergence of combustion and then electric motors has carried mankind through the industrial revolution into the modern era. Today, these systems are present in absolutely every aspect of our lives and are becoming increasingly complex. Initiated by R. P. Feynman in his December 1959 lecture entitled "There's plenty of room at the bottom,[12] the race for miniaturisation has since become a major challenge for the development of new technologies. Over time, two opposite strategies have emerged. The first one consists in the size reduction of pre-existing systems, also known as *top-down*. However, this approach remains limited by implementation processes and, above all, by changes in the behaviour of materials at smaller length scales. The second method, so-called *bottom-up*, overcomes these limitations by focusing on the development of nanometric units that can be operated selectively, while their integration into complex materials enable their exploitation at larger scales.

Commonly, a motor can be described as a structure capable of converting an energy into a mechanical energy. At the nanoscopic scale, a molecular motor is characterised by a periodic and non-reversible evolution. It is capable of providing continuous work in the form of translation or rotation as long as it is supplied with energy.[13] It should be distinguished from a molecular switch, which is defined by its ability to move reversibly from one thermodynamically (meta)stable state to another under the action of a given external stimulus, but whose work is necessarily cancelled if the system returns to its initial state.[3]

The integration of motor units is absolutely crucial in order to make practical use of the generated work. This step is all the more important as it allows, through clever design, to confer new properties to the combined sub-units. Thus, it is possible to create materials that behave macroscopically like a motor even from simple molecular switches and vice versa. A good example of such cross-over would be the development of Ikeda's photoactivated motor, based on a liquid-crystalline elastomer incorporating azobenzene derivatives (**Figure I.1**).[14] Such achievement arises from a spatiotemporal desymmetrization, *i.e.* where the activation of the involved switches is shifted in time and/or space.

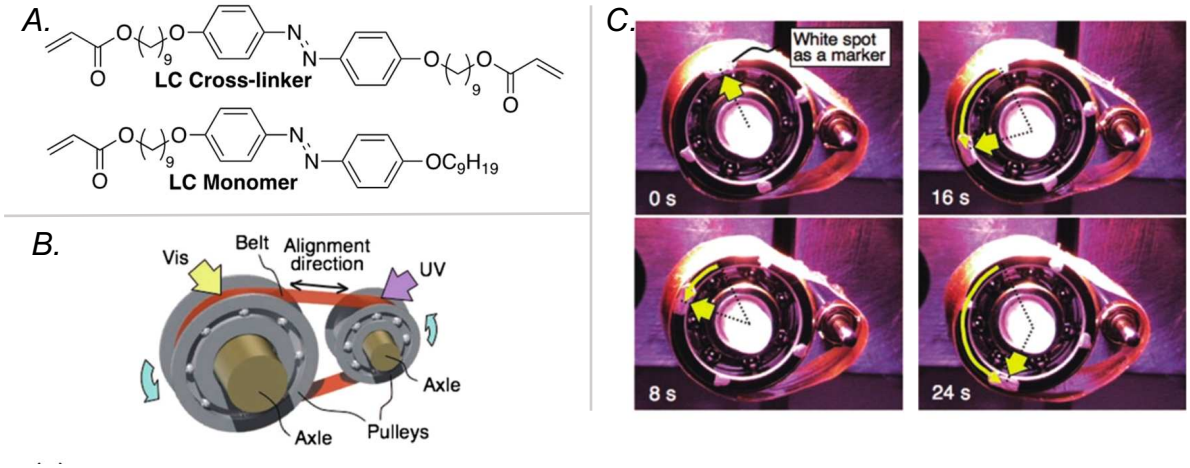

Figure I.1 A. Molecular structure of azobenzene-based cross-linker and monomer. **B.** Scheme depicting the liquid-crystalline elastomer (LCE) light fuelled motor: a belt made of LCE is fixed on two pulleys and is irradiated simultaneously at two different spots with respectively visible and UV light. The contraction-expansion of the material allows its rotation around the axles. **c.** Snapshots of the LCE film rotation over time. Adapted from ref 14.

These properties have encouraged chemists to focus on the development of functional motor units to form increasingly complex systems and novel materials.[15] In this respect, nature is an inexhaustible source of examples, since many metabolisms are based on the integration of motors to perform vital tasks, ranging from DNA synthesis with polymerase, to the manufacture of peptides via the ribosome.[16] Three systems particularly stand out, the motion of kinesin along microtubules, sodium/potassium pumps and ATP synthase. These systems have indeed inspired the development of the first artificial molecular motors, respectively Seeman's nanowalker,[17] Stoddart's supramolecular pump[18] and Feringa's unidirectional rotary motor.[1] The work of the latter two, as well as that of Jean-Pierre Sauvage, has been rewarded in 2016 with the Nobel Prize in Chemistry, granted precisely for "the design and synthesis of molecular machines".[19]

We will now present the operating principle of these various artificial motor units before focusing more specifically on Feringa's unidirectional motor and providing some examples of its implementation into complex systems.

I.1. Molecular walkers

In nature, nanowalkers are at the core of essential biological functions. The myosin superfamily is crucial for the mechanism of muscle contraction,[20] and the kinesin group is responsible of the transport of vesicles and organelles within the cells.[21] These protein motors share many similarities that can be drawn on. Their movement is progressive as well as directional. In the case of kinesin, it moves stepwise along microtubules whose polarity dictates the direction of the motion. Both are chemically powered by the hydrolysis of adenosine triphosphate (ATP).

In 2004, N. C. Seeman and W. B. Sherman developed the first prototype of a DNA-based artificial nanowalker.[17] This work marked the beginning of a frenetic development in the field[22] in order to gain in precision, by addition of dyes on the surface,[23] efficiency, by reducing the amount of fuel needed,[24] or surface variety, by working on carbon nanotubes.[25] Cargo could eventually also be transported from one point in space to another[25] and a one-pot multi-step synthesis mediated by a molecular walker has also been described.[26] Overall, there appears to be no general mechanism, with each system having its own approach. In some cases the path taken by the walker is destroyed after it passes through,[27,28] in others, the motion can be autonomous[29] and/or fuelled by light via built-in photoswitches[30] or photosensitizers.[31]

However, a trend could be pictured by the following example describing the motion of a tripod spider on a DNA surface following a planned pathway (**Figure I.2**).[28] The leg moves by diffusion until it reaches a substrate on the surface with which it will interact. As a result, a step is achieved. Once docked, it needs to be released while ensuring that the walker does not backtrack. To do so, it is possible to directly modify the substrate in contact with the leg or to add a competitor to the walker that will dislodge it. Here, a DNA enzyme cuts the substrate in half, thereby reducing its affinity with the spider leg (**Figure I.2B**). The surface is thus used as fuel and considered as "altered", so that the walker can then only move forward. In order to maintain the integrity of the surface, it is also possible to add a competing molecule to the substrate which will then bind to the leg (**Figure I.2C**). A degradation of this agent coupled with a difference in energy level between the initial state and the next step allows the equilibrium to be shifted towards motion.[24,32] In this case, the degradation of this competing unit acts as a driving force.

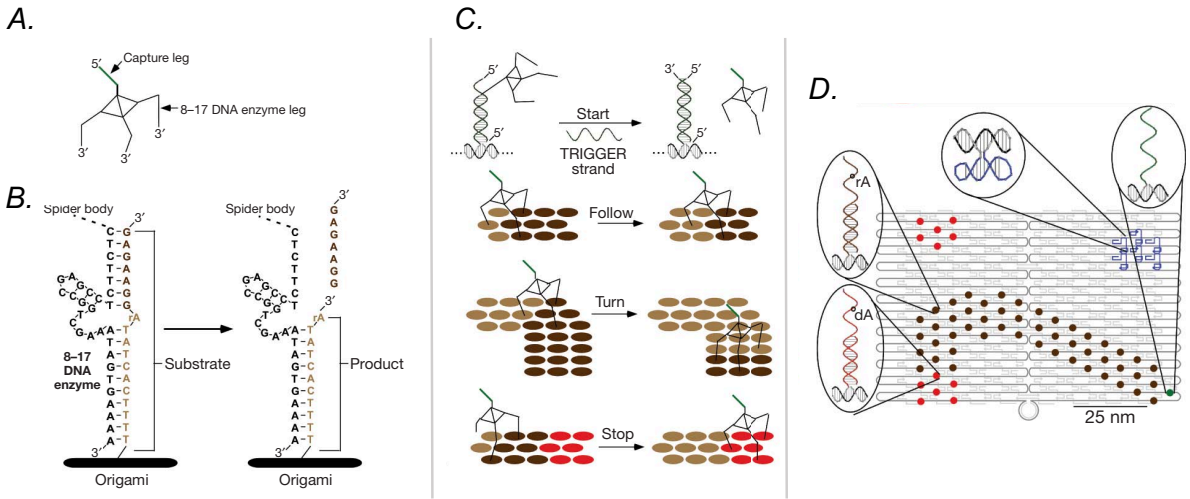

Figure I.2 A. Scheme depicting the tripod spider structure. Both capture and enzyme leg are made of a single-strand DNA. The former is used to anchor the structure on the surface at the start. **B.** Structure of one of the legs, it contains a deoxyribozyme enzyme capable of cleaving the complementary substrate at the RNA base position. **C.** To initiate the motion, a trigger DNA strand is added so as to release the tripode by liberating the capture leg from its anchor. The machine will start a stepwise motion following the path of unreacted substrates until it reaches a stopper made of a complementary strand without any RNA base

to cleave. **D.** Representation of the origami DNA map of the tripod pathway and schemes of its surface at different position: start/substrate/stopper/non functionalized. Adapted from ref 28.

In general, the majority of nanowalkers described in the literature uses DNA origami as track considering that it is a well-known and easily customisable carrier but their size and complexity make their integration difficult. The first described system based on relatively small organic molecule was elaborated by D. Leigh's team.[33,34] Orthogonal stations are distributed alternatively along an axle (**Figure I.4**). The first one is based on a hydrazone and can be cleaved under acidic conditions. Conversely, the second dissociates in a basic medium and is buit on a disulphide bridge. Thus, a walker unit capable of attaching to both of these stations can evolve along the thread according to pH changes. However, a simple alternation of acid and basic conditions results in a random distribution of the mobile unit along the axle. Indeed, as the stability of the different products is relatively similar (with the exception of the *1,4-C*$_5$ compound which results in the torsion of the main axle and is therefore less favourable), there is no driving force to move the walker forward (**Figure I.4A**). Therefore, the addition of a kinetically controlled step via a redox reaction has been used to induce an equilibrium shift in favour of the final product, *i.e.* 3,4-C$_5$ (**Figure I.4B**). Indeed, a bis-thiol intermediate is first formed by full reduction of the disulphide bridge (**Figure I.4C**). Its subsequent oxidation completely regenerates the disulphide function without setting up an equilibrium. Two alternatives are thus possible, either the mobile unit returns to its initial position or it switches station, the final ratio depends on the kinetic constant associated with each reaction.

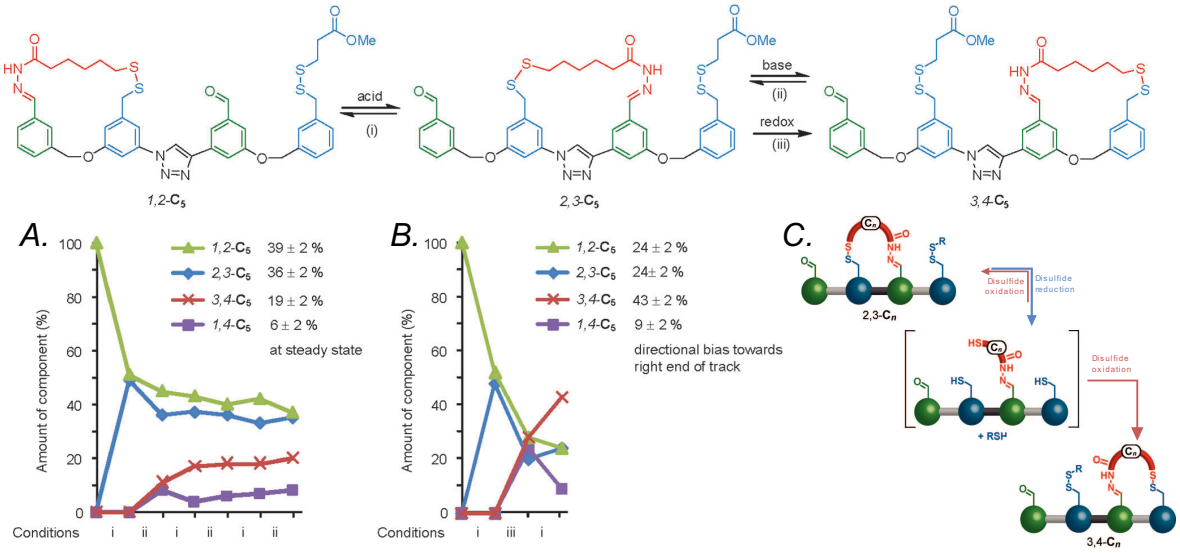

Figure I.3 Molecular structure of the walker (hydrazone station, disulfide bridge station, linker and walking unit) at different stages of motion without (acid/base) **A.** and with (acid/redox) **B.** directional bias, along with their corresponding products distribution. **C.** Schematic representation of the redox step involving the bis-thiol. Adapted from ref 22.

Such an approach where the energy level of each state is constant but the energy barriers are changing, depending on the position of the moving object, is known as an **information ratchet**. Conversely, a system, where the thermodynamic energy minima of each state are changing, is called an **energy ratchet**.

An example illustrating this second concept was also developed by D. Leigh's team.[35] Its structure is very similar to the previous system but this time incorporates a stilbene in the centre of the axle (**Figure I.4**). The presence of a double bond allows for a control of the system via its photoisomerisation at 365 nm (E --> Z) and 500 nm (Z --> E). It is thus possible to direct the movement of the walker by alternating isomerisation and acid-base conditions. Indeed, the implementation of cycle constraints modifies the energy levels of each state which are no longer equivalent, thereby shifting the equilibrium towards the most stable form.

A more recent and simpler approach has also been developed by the same team.[36] It consists in taking advantage of the presence of an energy minimum located at the end of a footholds sequence with equivalent energy levels placed in line. The walker will then move randomly along the thread until it reaches the energy sink where it will be trapped, and thus unable to go backtrack. This entrapment acts as a driving force. However, the longer the chain, the longer the time needed to reach the final station. This last system, by the presence of a thermodynamic trap, is quite similar by its principle to the molecular pumps described by Sir J. F. Stoddart, which we will discuss hereafter.

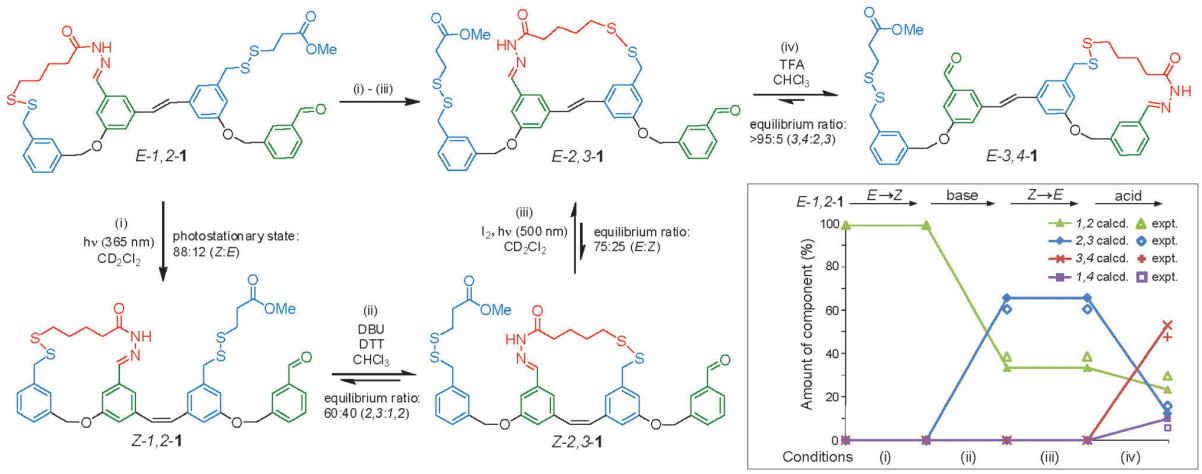

Figure I.4 Molecular structure of the light-fuelled molecular walker (hydrazone station, disulfide bridge station, alkene linker and walking unit) at different stages of motion with the corresponding products distribution. Adapted from ref 22.

I.2. Molecular pump and supramolecular motors

Molecular pumps are ubiquitous in nature in the form of active enzymes placed in cell membrane in the case of K^+/Na^+-ATPase,[37] but also in the mitochondrial membrane in the form of the proton pump known as quinone oxidoreductase.[38] These biological machineries are specialised in ion transport and are especially capable of counteracting a concentration

gradient. To do so, they rely on the hydrolysis of ATP which provide them with the energy required to move away from thermodynamic equilibrium. These systems are intricate, and artificially mimicking their mechanism requires the development of complex architectures. A family of structures, known as rotaxanes has emerged in this field and has now been extensively studied.

I.2.1. Rotaxane-based molecular pump

A rotaxane is a molecule consisting of a macrocycle threaded around a linear axle. The latter is fitted on both sides with stoppers that block the unthreading of the ring by inducing an important steric hindrance. For this reason, even though ring and axle are not directly linked together the breakage of a covalent bond is necessary to separate both units. Such interaction is known as **mechanical bond**.[39]

First described in 1967 by I. Harrison and S. Harrison, the "statistical" approach used towards rotaxanes was inherently inefficient with a 6% yield.[40] It consisted in adding stoppers to the thread, while hoping that it had randomly slipped through a macrocycle. In 1969, G. Schiff published the first "directed" synthesis of rotaxanes by covalently attaching the ring to the chain before adding the stoppers and releasing the macrocycle.[41] This approach did not rely on randomness anymore and paved the way towards the elaboration of many complex structures through the template effect.[42]

By design, a rotaxane allows the macrocycle to move freely along the axle. It is nevertheless possible to fix its position by adding a station that will act as a thermodynamic trap. Indeed, by implemeting supramolecular interactions (ionic, H bond, π-π stacking, ...) between the mobile unit and the thread, the energy level of the system can be locally lowered. If a second identical station is added, the macrocycle will then constantly move from one energy sink to an other without any particular preferences, behaving like a shuttle as first described by Stoddart in 1991 (**Figure I.6A**).[43] The addition of an asymmetry in these stations allows discrimination in order to promote one over the other. In the case of stimuli-sensitive stations, either by light,[44] H^+/e^-,[45] or even heat[46], it becomes possible to control the spatio-temporal evolution of the shuttle by modifying the affinity between these units.[47]

However, even in these cases a rotaxane is still comparable to a simple molecular switch as, by definition, the motion of the macrocycle is restricted to the axle and can only move from one station to another. This is in contrast with the pseudo-rotaxane, which is a very similar system but whose main difference lies in the absence of terminal stoppers.[48] Besides, if only one stopper remains, the obtained structure is called a semirotaxane.[49] In both cases, the macrocycle is able to leave or rejoin the thread depending on its affinity to the present stations in comparaison to its solvatation. Overall, this behaviour can be somewhat assimilated to that of a host-guest system where the equilibrium is controled by the thermodynamic energy levels of the associated and dissociated states.

The first example of unidirectionnal system was ingeniously designed by the group of A. Credi in 2012 who developed a prototype molecular pump. Initially powered by the combination of light and chemical agent (*i.e.* K^+),[50] it quickly evolved to depend solely on light irradiation

(**Figure I.6B**).[51] This system allows the unidirectional motion of a crown ether along an axle. The thread is composed of three parts. A central secondary ammonium acts as a thermodynamic trap through the establishment of H-bonds. This unit is then linked to an azobenzene on one side and a methylcyclopentyl on the other. The latter can be considered as a pseudo-stopper, since it limits the passage of the macrocycle without preventing it completely. Thus, a pseudo-rotaxane can be obtained with the preferential passage of the macrocycle through the azobenzene as long as it is in its initial form (E^+). However, after photoisomerisation (Z^+), the generated steric hindrance tends to destabilise the structure, leading to an increase in the associated energy level, and thereby to the departure of the macrocycle. As the kinetic barrier to cross on the switch side becomes much more important with the change of conformation, the passage through the cyclopentyl becomes more favourable. Overall, this molecular machine combines energy and information ratchet to provide work in the form of unidirectional translational motion. It is also autonomous as both photoisomerizations can occur in the same wavelength range (i. e. $\lambda > 400$ nm) inducing a continuous flow of macrocycles over time.

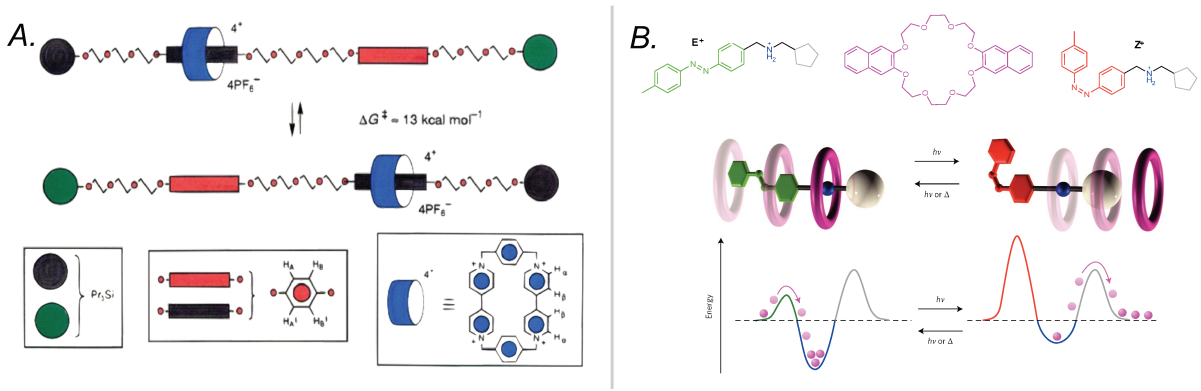

Figure I.5 A. Schematic representation of a two-station rotaxane made of hydroquinones linked together by a polyether chain terminated by two triisopropylsilyl units acting as stoppers. The macrocycle composed of two bipyridines linked by 1,4-phenylene units can randomly move from one station to the other. Adapted from ref 43. **B.** Molecular structure of the macrocycle as well as of the molecular pump (amine station, methylcyclopentyl stopper) before (**E**$^+$) and after (**Z**$^+$) irradiation. The scheme depicts how the ring threads through the azobenzene moiety and dethreads from the methylcyclopentyl. The corresponding energy diagram illustrates the effect of the photoisomerization on the energy levels and kinetic barriers of the system. Adapted from ref 51.

Stoddart's group also developed a system based on a combination of information and energy ratchet whose operation is no longer powered by light but by alternating redox reactions (**Figure I.6A**). It consists in a highly electron-deficient macrocycle (cyclobis(paraquat-p-phenylene) ($CBPQT^{4+}$))[52] and an asymmetric axle (D^+) comprising a central electron-donating station (1,5-dioxynaphthalene (DNP)) linked by polyether chains to an uncharged group (2-isopropylphenyl) on one side and a positively charged group (3,5-dimethylpyridinium) on the other.[53] Due to electronic repulsion, the macrocycle preferentially threads through the uncharged side until the central DNP where it is stabilised. Then, by reduction, the charge of the mobile unit is lowered, shifting the equilibrium in favour of the pseudo-rotaxane

dissociation. At the same time, this change in charge limits the repulsion between $CBPQT^{2+}$ and the pyridinium group. The energy barrier associated with the passage of the macrocycle through this stopper is then lower than passing trough the uncharged isopropylphenyl, leading to an oriented successive translation. The obtained unidirectional motion can be cycled by oxidation of the system to renew charges.

Overall, in both systems presented before, the release of the mobile units into the starting solution necessarily cancels out the work produced. A compartimentalisation similar to that of living systems would allow to counteract the concentration gradient and store the work produced. Such an approach has been implemented by Stoddart's group through the coupling of the previous molecular pump prototype[53] with a semi-rotaxane acting as a carrier.[54] This new system, although quite similar to the one described above, differs in the nature of its central station as well as in the overall organisation of its various components (**Figure I.6B**).[18] First of all, a bis-charged viologen is used as station since, when reduced, it can set up strong radical-radical interactions with $CBPQT^{4+}$ and, inversely, strong Coulomb repulsion when oxidized. Therefore, when both ring and threads are in their respective reduced form the macrocycle can cross the pyridinium-based pseudo-stopper to reach the thermodynamical equilibrium at a lower energy level.[55] Oxidation of the system regenerates the Coulomb thrust which destabilizes by repulsion the structure between the macrocycle and the charged stopper as well as the viologen station. As a consequence, the ring moves away and falls into a kinetical trap by passing through the uncharged isopropylphenyl derivative. It is then locked between this pseudo-stopper and the bulky bisisopropylphenyl moiety terminating the polyethylene chain. A second reduction of the system generates competition between a new macrocycle from the solution and the one already trapped to reach the energy sink. The difference in the kinetic energy barriers works in favour of the former thanks to the difference in charge between the pseudo-stoppers. A second oxidation then pushes this new macrocycle to join the first one on the carrier. The system thus counteracts the concentration gradient and is consequently able to move away from the thermodynamic equilibrium state in a perennial way. However, further redox cycles do not allow the addition of supplementary macrocycles because of the important repulsion between the trapped rings that increases their thermodynamic energy level and thereby lowers the kinetic barrier, in the reduced state, to reach the viologen station. A lengthening of the storage chain circumvents this problem and the implementation of a second identical pump,[56] replacing the bisisopropylphenyl stopper, doubles the overall efficiency of the system.[57]

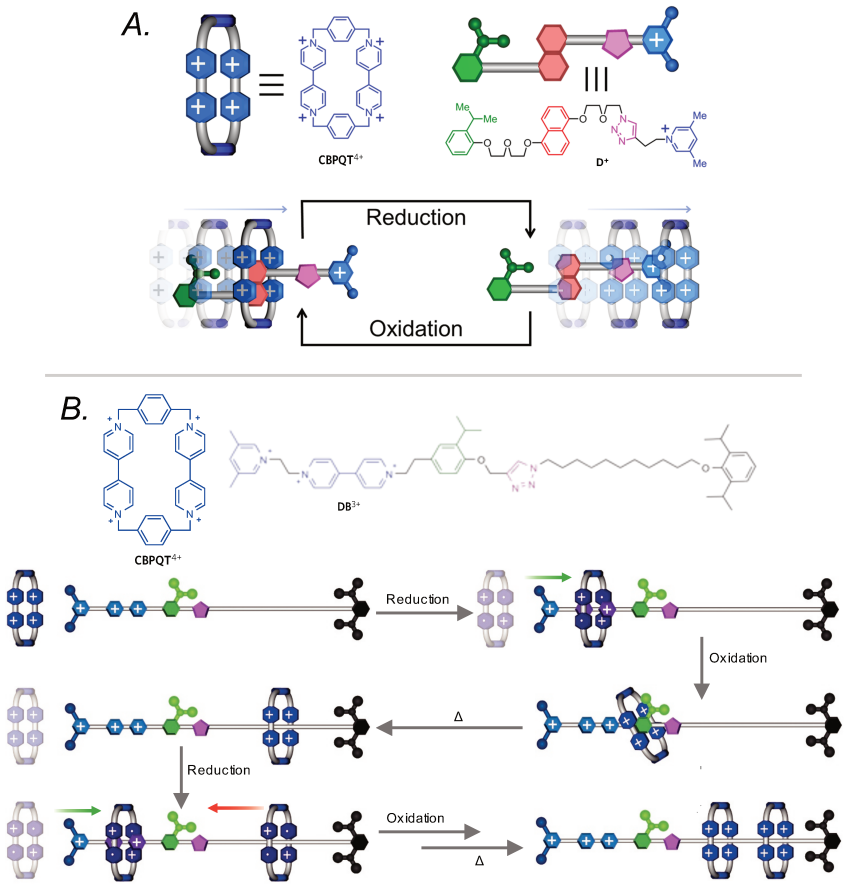

Figure I.6 A. Structure of the macrocycle (**CBPQT^{4+}**) and the molecular pump (**D^{+}**) (2-isopropylphenyl stopper, 1,5-dioxynaphthalene station, triazole linker and 3,5-dimethylpyridinium stopper). The schematic representation of the system shows how the directionality of the system is controled by the alternance of redox reactions. Adapted from ref 53. **B.** Molecular structure of the artificial pump composed of the macrocycle (**CBPQT^{4+}**) and the molecular pump (**DB^{3+}**) (3,5-dimethylpyridinium stopper, viologen station, 2-isopropylphenyl stopper, triazole linker, bisisopropylphenyl stopper). The associated scheme depicts the threading of the first and second macrocycle by alternating redox reactions. Adapted from ref 18.

I.2.2. Catenane-based molecular motors

Rotaxanes are not the only structures integrating mechanical bonds that have been used in the development of molecular motors. Catenanes, which are defined as molecules incorporating at least two interlocking rings so that their separation requires the breaking of a covalent bond,[39] have also been thoroughly investigated. First synthesised in 1960 by E. J. Wasserman using a statistical approach,[58] G. Schiff and A. Lüttringhaus detailed the first covalent-directed synthesis in 1964.[59] However the main achievement came from the group of J. P. Sauvage who greatly facilitated their access with the development of an efficient coordination-directed approach, *i.e.* using metal centres to pre-organise the framework.[60–62] Thanks to this strategy, a wide variety of systems could be elaborated[63] ranging from structural curiosities, such as Solomon's rings,[64] to their integration on surfaces, in Langmuir monolayers,[65] as well as in materials, such as active gels.[66]

Similarly to rotaxanes, it is possible to control the position of the rings in relation to each other by the addition of energy sink. The best known example was described by the group of J. P. Sauvage and consists in the incorporation of a phenanthroline and a terpyridine stations into each of the loops so that they can coordinate to a central copper atom (**Figure I.8A**).[67] The nature of the involved sites in this interaction depends on the degree of oxidation of the metal which modifies the geometry of the formed complex. Thus, copper(II) preferentially binds to terpyridines and copper(I) to phenanthrolines. As a result, a modification of the relative position of the rings is observed as a function of the redox conditions. However, as the direction of rotation of the rings remains random, the system can only be considered as a switch and not as a molecular motor.

The team of D. Leigh was the first to achieve a unidirectional rotation by developing a complex [3]catenane structure (**Figure I.8B**).[68] It consists of two sliding rings containing four benzyl amide moieties, threaded around a third and larger macrocycle, equipped with four different stations. Thanks to the formation of H-bonds of varying strength, the sliding ring interacts preferentially with the fumaramide (A), the methylated fumaramide (B), the succinic amide ester (C) and the amide (D) according to their decreasing order of stabilization. As a result, only sites with the lowest energy level, namely (A) and (B), are initially populated. Since the (A) group was placed in the vicinity of a benzophenone acting as a photosensitizer, it can be selectively isomerized (*E* --> *Z*) at 350 nm. Destabilised, the macrocycle will then move to the third most favourable station, *i.e.* the succinic amide ester (C). However, to reach it, it is necessary to move counter-clockwise due to the presence of the second ring in position (B), blocking the pathway in the clockwise direction. A second irradiation at 254 nm results in the photoisomerization (*E* --> *Z*) of station (B), forcing the macrocycle to interact with the last available station, namely amide (D). Again, only a counter-clockwise movement is possible. The third step consists in restoring the initial *E* configuration of stations (A) and (B), either by irradiating in the visible spectrum or simply by heating at 100 °C. With the two best interaction sites available again, the two rings promptly re-attach to them. However, as the rings block the path of each other, they can only join the nearest station. The ring at (C) joins position (B) and the one at (D) links to site (A). A new series of irradiations at 350 nm and then at 254 nm followed by heating leads to a return to the initial state. Overall, a unidirectional rotation of 360° of the two macrocycles is achieved.

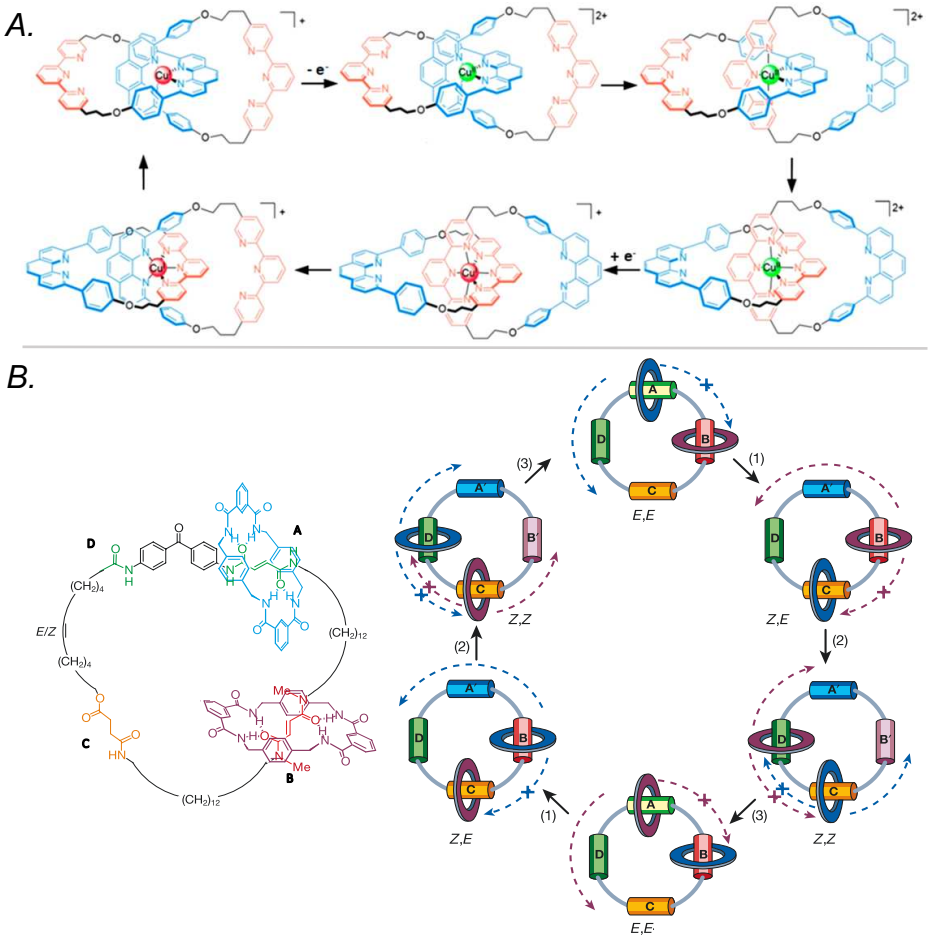

Figure I.7 A. Molecular structure of the system (terpyridine/phenanthroline) at different steps. The motion is initiated by the oxidation/reduction of the metal centre which destabilizes the configuration of the catenane. After a two-step rearrangement, a new thermodynamic equilibrium is reached. Adapted from ref 3. **B.** Molecular structure of the [3]catenane-based supramolecular motor made of a fumaramide group (A), a methylated fumaramide (B), a succinic amide ester (C) and an amide (D). The schematic representation shows the different intermediates formed after an irradiation at 350 nm (1), an irradiation at 254 nm (2) and heating at 100 °C (3), as well as the possible motion of the macrocycles. Adapted from ref 68.

This supramolecular motor was later simplified and improved by limiting the number of steps and especially by making it reversible (**Figure I.8A**).[69] A single benzyl amide ring is threaded through a macrocycle that now has only two stations composed of a fumaramide and a succinic amide ester. A *tert*-butyldimethylsilyl ether and a trityl group were placed on either side of the interaction sites to act as orthogonally removable stoppers. Selective deprotection followed by corresponding reprotection allows the mobile unit to be shifted towards the fumaramide, which is the most stable station. This rotation can only occur in one direction as the other branch remains blocked by the orthogonal protecting group. Irradiation at 254 nm isomerises the double bond and strongly reduces the affinity of this site for the ring. Finally, a new deprotection-reprotection cycle allows the shuttle to return to its initial position, thus completing the 360° unidirectional rotation. It is important to note that the stoppers cleavage sequence is essential since it controls the direction of rotation and confers reversibility to the

system. Later, the fumaramide station is reactivated by heating or with visible light irradiation in order to start a new revolution.

Although functional, these two supramolecular motors require an important number of external interventions (change of redox conditions/irradiation at different wavelengths) to complete a single rotational cycle, which makes them of little practical use. A third chemically-fuelled catenane-based molecular motor has been developed, again by the same team, which differs from the other two precisely by its ability to operate autonomously.

A benzyl amide ring is threaded around a macrocycle containing two fumaramide stations and two identical fluorenylmethoxycarbonyl (Fmoc) stoppers (**Figure I.8B**).[70] The latter are constantly cleaved and reformed, due to the presence of Fmoc-Cl (protection), trimethylamine (deprotection) and $KHCO_3$ (pH stabiliser) in solution. The deprotection kinetic is constant, regardless of the position, but this is not the case for the protection reaction. Indeed, due to the size of the reagent, the steric hindrance caused by the proximity of the macrocycle imposes to cross a more important energy barrier. An asymmetry is therefore observed between the two stoppers, where the one present near the ring is more often dissociated than the one far from it. Such a process is characteristic of an information ratchet mechanism. Consequently, during its Brownian displacements along the macrocycle, the shuttle has a greater probability of reaching the second station in the clockwise direction. The same bias will then occur once more, resulting in an overall unidirectional rotation of the system over a period of 12h.

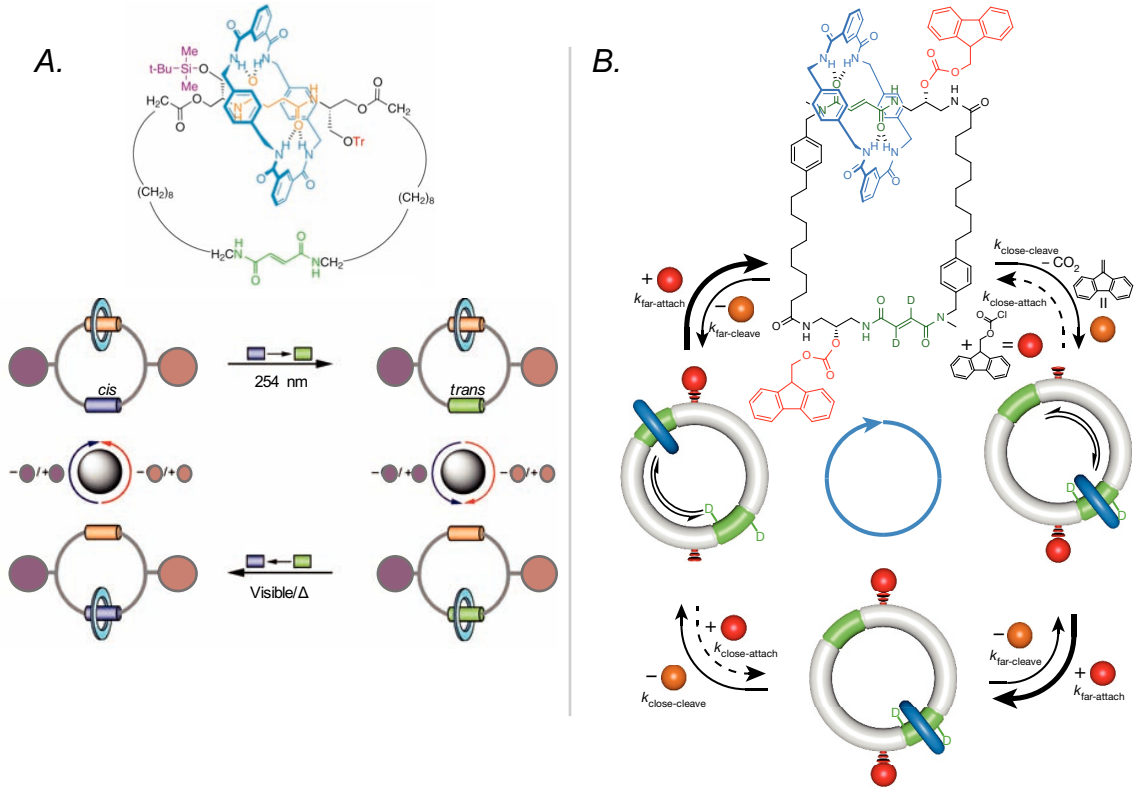

Figure I.8 A. Molecular structure of the catenane-based motor (fumaramide station/succinic amide ester station/tert-butyldimethylsilyl stopper/trityl stopper). The scheme depicts the different intermediates after

the activation/deactivation of the station by photoisomerisation and the protection/deprotection of the stoppers. Adapted from ref 69. **B.** Molecular structure of the molecular motor (fumaramide station/Fmoc stopper/benzamide ring) and schematic representation of the rotation intermediates. The stopper close to the ring is more likely to be dissociated due to steric hindrance, thus favouring the clockwise motion. Adapted from ref 70.

Overall, rotaxanes and catenanes are two families of compounds capable of respectively opposing a concentration gradient and setting up a rotational motion. However, due to the complexity of these molecules and the difficulties of their implementation, molecular pumps and supramolecular motors have not yet been integrated into larger structures that would allow the work generated to be usefully exploited to perform novel functions. In contrast, the simpler design of rotary unimolecular motors has led to their integration into a wide variety of systems.

I.3. Molecular rotary motors

ATP synthase is one of the most significant biological systems.[71] This enzyme is indeed responsible for the synthesis of adenosine triphosphate, which serves as a fuel for many essential functions, ranging from DNA, RNA and protein synthesis to muscle contraction and even vesicle as well as ion transport. It is a unidirectional rotary molecular motor, chemically powered by a proton gradient.[72] It has inspired the development of artificial unidirectional systems by setting up simple criteria: continuous cycling motion under specific energy input and progressive work output.[3] From these requirements, a number of molecular machines have been developed, which they can be divided into two categories, those whose movement revolves around a single covalent bond and those based on double bonds.[2]

I.3.1. Single bond-based rotary motors

Rotation is an intrinsic property of the single covalent bond. Depending on the surrounding steric hindrance, it can reach speeds of up to a dozen picoseconds per cycle in the case of ethane, putting our current measurement techniques to the test.[73] Although fast, a random rotation is not enough to produce work and inducing non-reversible unidirectionality in the movement is necessary to reach a molecular motor. The first prototypes were developed by Kelly's team in 1999 with a phosgene-fuelled unimolecular ratchet, based on the coupling of a helicene with a triptycene (**Figure I.10A**).[74,75] It was capable of unidirectional motion but remained limited to a single rotation of 120°. Other attempts were reported by the team of Mock and Ochwat in the following years (**Figure I.10B**).[76] Based on a tricarboxylate oscillating between two anhydride forms and powered by an acylketenimine, this system generated a continuous rotation of 180°. However by its principle, this device acted more like a switch going constantly back and forth rather than a motor as, after a first unidirectional rotation, a second one systematically cancelled any work produced.

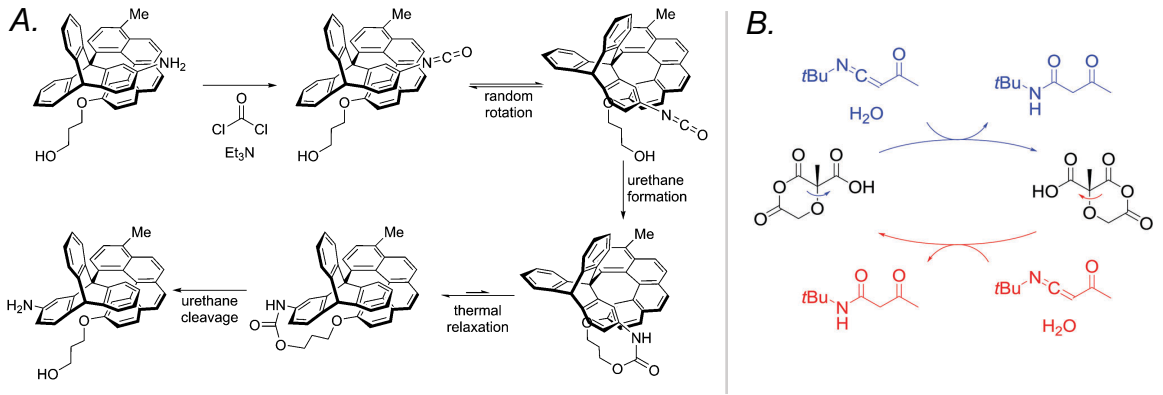

Figure I.9 A. Molecular structure of the molecular motor developed by the group of Kelly. The formation of an isocyanate is followed by a thermal rotation and the subsequent formation of a urethane moiety. A thermal relaxation allows the unidirectional rotation of the triptycene towards a more stable conformation. Cleavage of the urethane bond allows to recover the starting amine. Adapted from ref 74. **B.** Molecular structure of the oscillating anhydride pseudo-motor fuelled with acylketenimine. A back and forth motion is continuously generated but no work is produced. Adapted from ref 2.

It was not until 2005 that the first example of a functional molecular motor rotating around a single covalent bond was published by the group of Feringa (**Figure I.10A**).[77] The system is based on a tri-*ortho* substituted bisaryl. The upper part is functionalized with two phenols covered with orthogonal protecting groups (allyl and *para*-methoxy benzyl (PMB)) and the bottom part with a single carboxylic acid. Due to the high steric hindrance inherent to this family of compounds, free rotation around the central bond is impossible at room temperature. Both stator and rotor are blocked and thus cannot racemize, allowing to differentiate the two atropoisomers. Selective deprotection of the PMB group followed by lactonization of the phenol with the neighbouring carboxylic acid forms a cyclic intermediate. An asymmetric reduction of this function leads to a ring-opening reaction by preferentially generating the atropoisomer of choice. Reprotection of the phenol coupled with an oxidation of the alcohol allows the regeneration of the consumed moieties. Selective cleavage of the allyl protecting group followed by another asymmetric ring-opening of the spontaneously formed lactone, as well as a second protection/oxidation cycle allows to recover the starting isomer after performing a 360° unidirectional rotation. The rotation can be achieve in both directions since the chirality of the reducing agent ((*S*/*R*)-2-methyl-CBS-oxazaborolidine) dictates the unidirectionality and thus allows to pass from one atropoisomer to the other with great efficiency (>90% unidirectionality). However, this system relies on a large number of steps. Up to 10 reactions, including deprotection, lactonization, reduction, oxidation and reprotection, must be carried out to complete a single cycle. The overall yield is therefore necessarily low, reaching a maximum of 21% in this case.

In 2016, the same group developed a different molecular motor, powered this time by the oxidation/reduction of palladium (**Figure I.10B**).[78] A bisaryl, functionalized with a bromine and a sulfoxide placed on the rotor and stator respectively, is again characterized by the formation of stable atropoisomers at room temperature. The sulphur group, in the presence of Palladium(II), promotes activation of the C-H bond to form a palladacycle. This intermediate

is distinguished by a significant decrease in the energy barrier of the rotation around the central bond, allowing the transition from one isomer to the other. DFT calculations have shown that one of the atropoisomers is thermodynamically more stable than the other. This difference in stability is due to the geometry of the metal centre and is imposed by the asymmetric sulphur moiety. Followed by the reductive elimination of the complex and the subsequent regeneration of the C-H bond, the equilibrium shift induces an overall 180° clockwise rotation. The second half of the cycle follows a similar pathway involving the C-Br bond which interacts specifically with Palladium(0) via an oxidative addition. After cyclisation, isomerisation and a ring-opening reaction the initial product is recovered. Overall, a unidirectional 360° rotation is achieved. Despite a simplified process compared to the previous example, this system still requires four separate steps and is not autonomous. However, the authors hope to establish reaction conditions that allow for continuous motion using the palladium formed *in situ*, but such a system has not been described to date.

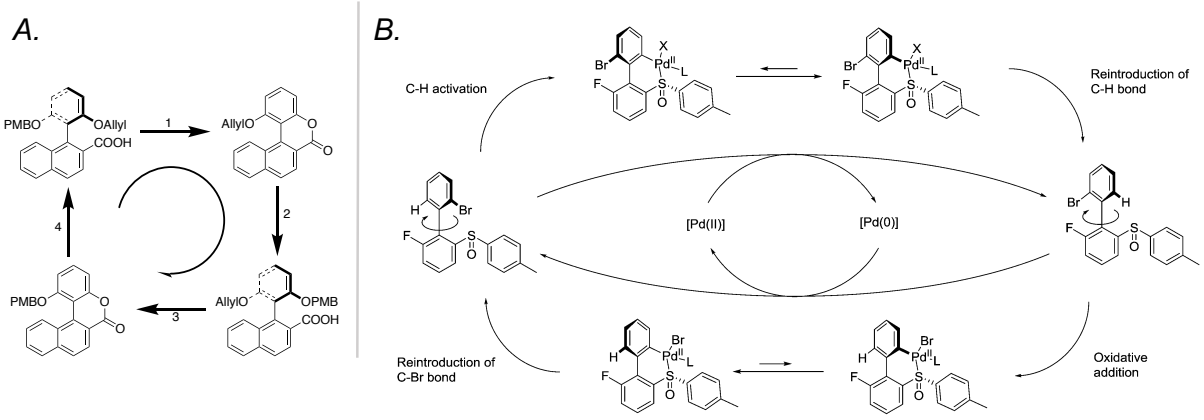

Figure I.10 A. Molecular structure of a single covalent bond molecular motor: (1) PMB deprotection and spontaneous lactonization. (2) Asymmetric reduction, alcohol oxidation and phenol protection. (3) Allyl deprotection and spontaneous lactonization. (4) Asymmetric reduction, alcohol oxidation and phenol protection. Adapted from ref 77. **B.** Molecular structure of a palladium-based rotary motor at different successive steps. The motion is powered by the redox property of Palladium which interacts with the C-H or C-Br bonds to form a palladacycle intermediate allowing to switch from one atropoisomer to the other. The motion is directed by the asymmetric sulfide group. Adapted from ref 78.

Finally, another interesting example of single bond-based molecular motor has been developed by the group of Sykes in 2011 and relies on butylmethyl sulphide (**Figure I.11A**).[79] This system is bound to a surface at the sulphur atom and is particularly remarkable for its ability to operate via electrical rather than chemical energy. Although achiral in the gaseous or liquid state, attachment to a surface via one of the non-bonding doublets of the sulphur leads to the formation of two enantiomers. A simple thermal rotation does not show any particular directionality. However, excitation of this rotor by a scanning tunnelling microscope (STM) tip promotes one direction by increasing its rotational speed relative to the other. This difference is of the order of 5% and is directly caused by the asymmetry of the STM tip.

In 2013, a second electrically powered system has been developed by Hla *et al.*, it is constructed from a borate-based tripod stator fixed on a gold surface and linked, via a ruthenium atom, to a five-armed rotor, bearing four ferrocenes and one tolyl (**Figure I.11B**).[80] Unlike previous examples, this motor does not involve rotation around a single covalent bond but around the central metal-cyclopentadienyl axis. The presence of a truncated arm induces an asymmetric sawtooth profile in the ground state potential energies. The application of a voltage with the help of a STM tip in the vicinity of a given subunit of the rotor causes the rotor to rotate in the corresponding direction. The system is therefore capable of clockwise or counter-clockwise motion depending on the nature of the excited arm.

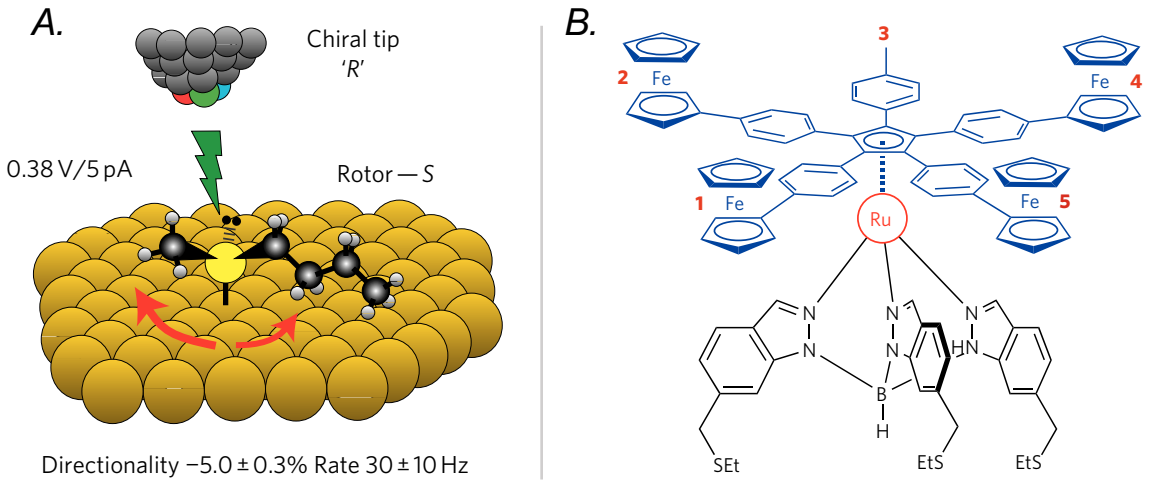

Figure I.11 A. Scheme depicting the butylmethyl sulphide-based motor. The rotation is triggered by a chiral STM tip. Adapted from ref 79. **B.** Molecular structure of the five arms-based motor whose directionality is controlled by the position of the STM tip: above the allyl group the rotation occurs clockwise, above one of the ferrocenes the motion is counter-clockwise. Adapted from ref 80.

Ultimately, molecular motors based on rotation around a single covalent bond are quite difficult to build and quite impractical to use. To date, the few functional systems are chemically require the setting up of specific reaction conditions at each step of the cycle. They are therefore not autonomous, which makes their integration into complex systems all the less attractive, to the extent that none has yet been reported. But above all, they suffer from the comparison with molecular machines based on rotation around double bonds, whose operation is simultaneously faster, more efficient and more practical.

I.3.2. Double bond-based rotary motors

The double bond is at the heart of the mechanism of these molecular motors. An alkene combines both σ and π interactions and is characterised by an extremely slow rotational speed. Indeed, moving away from the initial planar configuration requires breaking of the π bond. Therefore, the corresponding kinetic energy barrier is too high to be overcome at room temperature, allowing the separation of the E and Z stereoisomers. First synthesized in 1843

by Laurent,[81] stilbene consists of two aromatic rings linked together by a double bond. This compound is capable of photoisomerisation, *i.e.* switching from one isomer to the other when exposed to light. The *trans* --> *cis* isomerization typically takes place under UV irradiation and the reversed *cis* --> *trans* occurs usually within the visible range. However, irradiation of stilbene can also lead to reversible cyclisation to form a dihydrophenanthrene.[82] Despite a quantum yield of 0.1, the presence of oxygen or any other oxidising agent can result in the irreversible oxidation of this intermediate, shifting the equilibrium and degrading the photoswitch. This side reaction can easily be avoided by substituting the *ortho* positions of the two aromatic centres. An indirect consequence is the generation of steric hindrance in the vicinity of the double bond, a zone called the fjord region. This overcrowding results in a deformation of the bond by imposing a torsion angle between the different groups which adopt either a left-handed (M) or a right-handed (P) helicity. The addition of chiral moieties close to this area can influence the relative stability of the resulting helices and may favour one over the other.

Taking advantage of the energy levels difference, the group of Feringa developed in 1999 the first molecular motor, which consists in two identical tetrahydrophenanthrenes linked together by a double bond and functionalized in *ortho* position by two methyl groups with the same absolute configuration (*R*) (**Figure I.12A**).[1] The system initially adopts a (P,P)-*trans* organization, which is thermodynamically the most stable (**Figure I.12B**). Under UV irradiation at 280 nm, a reversible photoisomerisation forms the (M,M)-*cis* intermediate. Due to the steric hindrance induced by the equatorial methyl moieties, a thermal helix inversion (THI) spontaneously occurs to revert to the more stable (P,P)-*cis* configuration. Subsequent photoisomerisation at 280 nm results in another photoequilibrium in favour of a second unstable intermediate, the (M,M)-*trans*. Once again, in order to release the steric strain and return the methyls to their respective axial position, another thermal inversion takes place. Although thermodynamically favoured, the latter requires the crossing of a significantly higher energy barrier resulting in the need to heat the medium to 60°C. The (P,P)-*trans* is thus regenerated after a 360° rotation in four steps. Overall, light fuels the system by pushing it out of equilibrium, while the chiral groups impose the unidirectionality which allows to return to the most stable state. The motor is therefore autonomous and works continuously as long as it is irradiated.

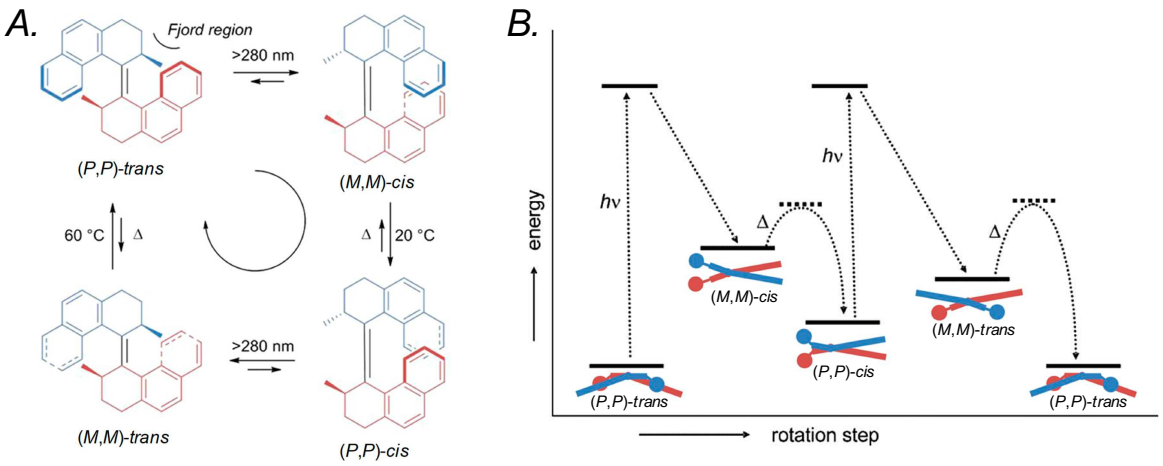

Figure I.12 A. Molecular structure and mechanism of the first light-driven unidirectional motor. **B.** Energy profile of each intermediate and their corresponding top view. Adapted from ref 3 and 2.

The design of this first molecular motor device highlighted a number of questions regarding its operation, limitations and potential that have been continually explored to this day. The first aspect examined concerned the asymmetry between the two thermal helix inversions. Indeed, one takes place at room temperature while the other requires significant heating. To limit this phenomenon, the structure of the lower part of the system (stator) has been replaced by a more symmetrical assembly while the upper part (rotor) remains the same (**Figure I.13A**).[83] This new type of system involving only one chiral centre is considered as the second generation of light-driven molecular motors.[84] The overall mechanism of rotation is identical: two photoisomerisations and two thermal helix inversion steps. The very close energy levels of the unstable *cis* and *trans* forms lead to in similar kinetic barriers. Additionally, the distinction between stator and rotor makes the system very interesting for asymmetric functionalisations, paving the way for the elaboration of more complex structures.

Subsequently, two additional variations were developed with the aim of generating a rotation with the minimum of chiral information. Thus, in 2015 the third generation was built around the coupling of two rotors with a single stator, carrying a pseudo-chiral carbon (**Figure I.13B**).[85] This structure, which is a fusion of two molecular motors, does not have a true asymmetric centre since a plane of symmetry is present. Similarly to the previous generation of motors, the key factor is the difference in steric strain between the stable and unstable forms caused by the presence of a bulky moiety. As a result, during the photoisomerisation of this system, the shift of the methyl group from the axial to the equatorial position causes an increase in the energy level of the isomer formed. This difference is sufficient for a thermal helix inversion to take place, allowing a return to the initial state after a unidirectional 180° rotation. Interestingly, the design of this molecule allows the two molecular motors to rotate in opposite directions, reminiscent of the movement of the wheels of a car.

In 2018, the fourth generation of molecular machines pushed the boundaries even further by using a completely achiral motor. The unidirectionality of the rotation is directed, in this case, by an additional molecule (**Figure I.13C**).[86] Upon photoisomerization at 365 nm, the thiourea

moieties of the motors are brought together, so that they can interact with the phosphate of the substrate via the formation of H-bonds. Without this chiral unit, the two possible isomers have identical energy levels and thermal helix relaxation occurs rapidly and randomly in both directions. The proximity of this bulky unit allows to differentiate the energy levels through the implementation of steric hindrance. One form is thus preferred, shifting the equilibrium in its favour. The asset of this system lies in its ability to change the rotation directionality of the motor without having to modify it synthetically, which was necessary until now.[87] It only requires changing the chirality of the phosphate present in solution.

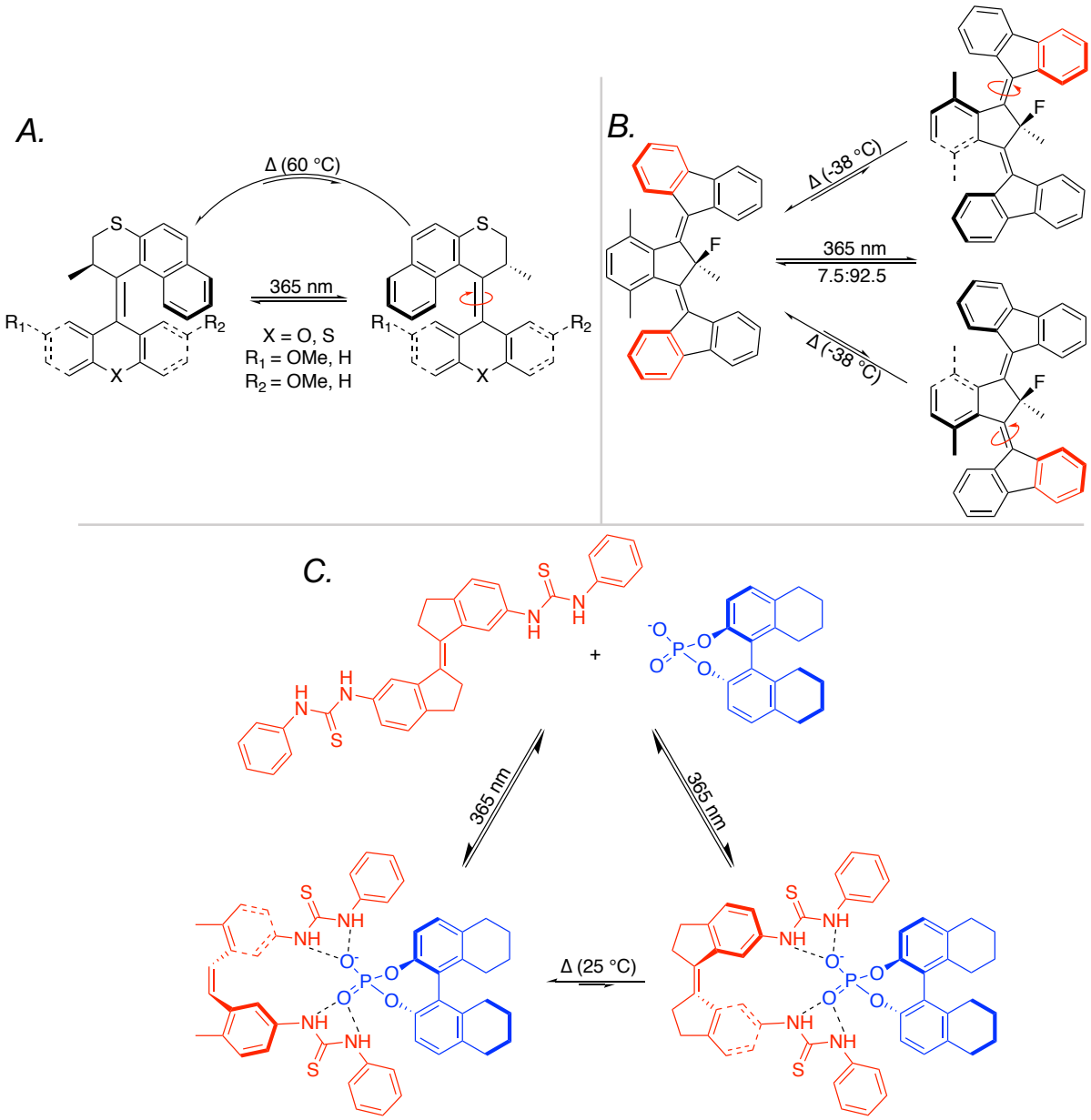

Figure I.13 Molecular structure of the **A.** second, **B.** third and **C.** fourth generation of light-driven motor and their corresponding intermediates.

One of the most studied property of molecular motors centred around a double bond is their speed of rotation. Indeed, a machine of interest must be able to operate at a rate compatible with the task at hand. This is one of the major drawbacks of non-autonomous systems since each cycle requires external inputs to modify the reaction conditions (wavelength, reactants, electrical potential). This problem is even more present in chemically powered systems, especially when purification of the motor is required between each step. In this respect, light is a powerful tool because it is easily controlled in time and/or space and it is not invasive. In the case of crowded alkenes, the rotational speed is undeniably related to the light intensity since photoisomerization pushes the system out of equilibrium. However it is not the kinetically limiting step as this process is extremely fast (in the picosecond time scale).[88,89] It is the helix inversion that limits the overall speed of rotation with its dependence on the size of the energy barrier to be crossed. The larger the barrier, the slower the thermal step, so it is essential to try to lower it as much as possible. To do so, two approaches have been developed. The first one consists in further destabilising the unstable intermediate formed following a photoisomerisation by increasing the size of the chiral group.[90] The second involves lowering the energy level of the transition state by limiting the steric hindrance within the fjord region.[91,92] Thus, switching from a rotor based on a 6-carbon ring to a 5-carbon one dramatically increases the speed of rotation.[93] Similarly, the addition of a bridging heteroatom on the stator also improves the system performance.[94] In the end, the group of Feringa developed molecular motors capable of operating in the MHz regime (**Figure I.14**).[4] Finally, external parameters can also influence the speed of rotation. In addition to the temperature of the medium, the viscosity of the solvent plays an important role in the thermal helix inversion[95] and, to a lesser extent, in the photoisomerisation step.[96] The higher the viscosity, the more energy is required to rearrange the solvent and the slower the system is. This effect is even further amplified with the addition of rigid and bulky moieties on the motor.[10]

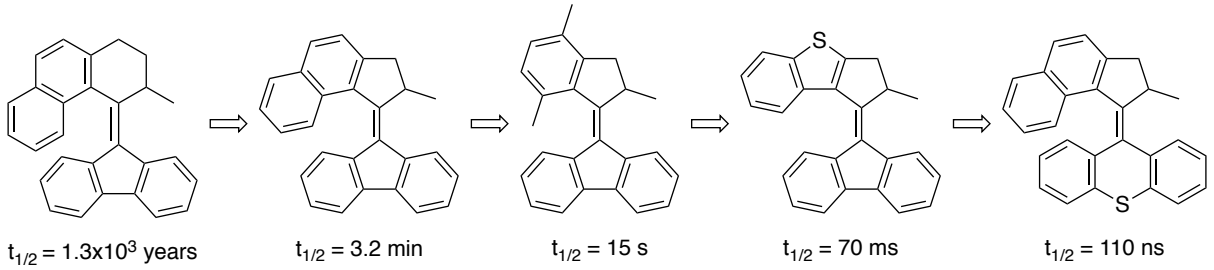

Figure I.14. Molecular structure of different motor units ranged according to their rotational speed. $t_{1/2}$ corresponds to the half-life of the unstable isomer at 25°C generated by photoisomerization and is inversely related to the rotation rate.

Besides the team of Feringa, two other research groups have succeeded in elaborating molecular motors centred on a double bond and powered by light, *i.e.* the imine and hemithioindigo-based derivatives, developed by J. M. Lehn and H. Dube, respectively. Initially conceptually designed in 2006,[97] the operation of imine motors was only validated experimentally in 2014 (**Figure I.15A**).[98] This system uses mainly diaryl-*N*-alkyl imines which

are known not to isomerise at room temperature. After a first photoisomerisation step, two orthogonal thermal relaxation modes can occur. The first one is a ring inversion and is similar to what is observed in C=C systems. It involves a unidirectional rotation of 180°, a complete turn thus requires a subsequent photoisomerization and thermal relaxation. The second process corresponds to the in-plane nitrogen inversion. Specific to imines, it allows a unidirectional rotation of 360°. These two mechanisms are in competition with each other but it is possible to favour one over the other by adjusting the structure of the motor. The ring inversion mechanism is indeed dependent on the flexibility of the stator as too much rigidity will considerably increase the corresponding energy barrier. Synthetically highly accessible, these molecular machines therefore open the way to the future development of a whole new variety of systems.

On the other hand, the hemithioindigo-based motor was developed in 2015 by the team of H. Dube (**Figure I.15B**).[99] Its operation remains very similar to that of Feringa. The same alternating photoisomerisation/thermal relaxation steps are thus present and the unidirectionality is ensured by the presence of a chiral sulphoxide placed on the stator. The major interest of this structure lies in its capacity to operate at higher wavelengths (> 400 nm), thus being less harmful for the system as well as its environment, and to possess a relatively low relaxation kinetic barrier, which translates into high rotation speeds (kHz range).

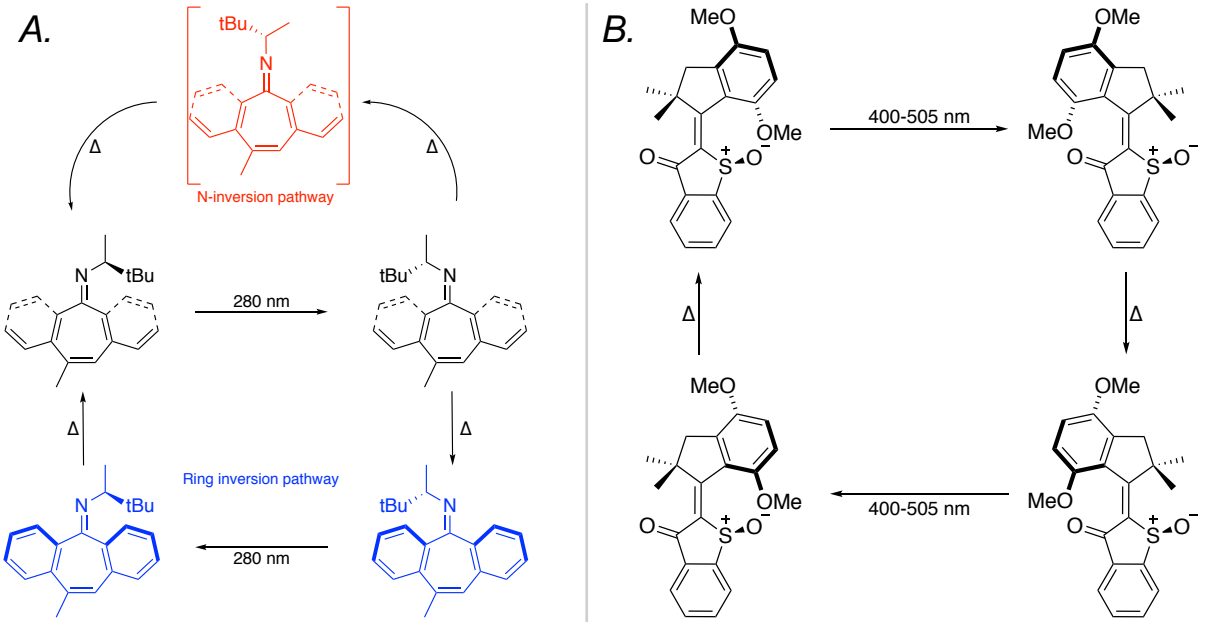

Figure I.15. Molecular structure of the **A.** imine-based and **B.** hemithioindigo-based motors and their corresponding intermediates.

We have seen that researchers have developed a large variety of molecular motors with various performances. One main characteristic of these motors is their ability to perform a task when supplied with energy. In order to retrieve the work output produce by these motors at the molecular scale, scientists have considered their integration into complex systems at higher length scales.

I.4. Integration of molecular motors

A molecular motor is characterised by setting up a continuous motion while producing work as long as it is supplied with energy. However, isolated in solution, the work of a machine is difficult to exploit in a useful manner. To this end, it is necessary to organize it within a system capable of using, coordinating and even amplifying the work produced to achieve novel functions. Nature is full of magnificent examples of molecular machinery accomplishing tasks that are fundamental to the proper functioning of living organisms. Whether it is muscle contraction with myosin, peptide, DNA and ATP synthesis or even K^+/Na^+ pump each of these motors operates in an environment where it is perfectly integrated. In this context, Feringa's motors are particularly well adapted as they can be functionalised asymmetrically, need only light to function and their rotation speed can be adjusted to match the desired task.

In this section we will present a list of some of the most prominent examples, ranging from the nano- to the macroscale, involving collective motion of molecular motors that are embedded into a larger structure and synchronised in time and/or space to perform novel tasks and functions.[100]

At the nanoscale, the controlled transport of objects is a major challenge for the elaboration of organised systems. To do so, different approaches have been developed such as nanowalkers presented previously, but also “nanocars”. These nanodevices consist of wheels linked together by a rigid chassis that can move on a surface.[101] Initially, these systems were passive and limited to oriented movement driven by Brownian motion. In 2006, a first active car was designed by J. M. Tour's team in which a motor is incorporated into the central axle, allowing a unidirectional skipping motion of the structure at each rotation (**Figure I.16A**).[102] Despite its ingenuity, no real movement could be observed, most certainly due to strong interactions between the surface and the nanocar. In 2011, Feringa's team developed the first functional prototype capable of travelling unidirectionally on a surface (**Figure I.16B**).[103] It incorporates four molecular motors used as wheels, substituting the fullerenes usually employed until now. Powered by an electrical voltage created by the tip of a scanning tunnelling microscope, the movement follows a rotational process identical to that induced by light irradiation. The directionality is controlled by the nature of the different chiral centres and the distribution of their absolute configuration along the structure results in different types of motion. It is thus possible to move the system in a straight line in the case of the meso-(*R*,*S*,*R*,*S*) isomer or along a curved path with the meso-(*R*,*R*,*R*,*R*) structure. Conversely, the meso-(*R*,*S*,*S*,*R*) form does not generate any movement since motors work in opposition to each other. Nowadays, international nanocar races are regularly organised, where research teams are competing to develop the fastest system.[104] We can certainly expect many new and more innovative designs to emerge in the future.

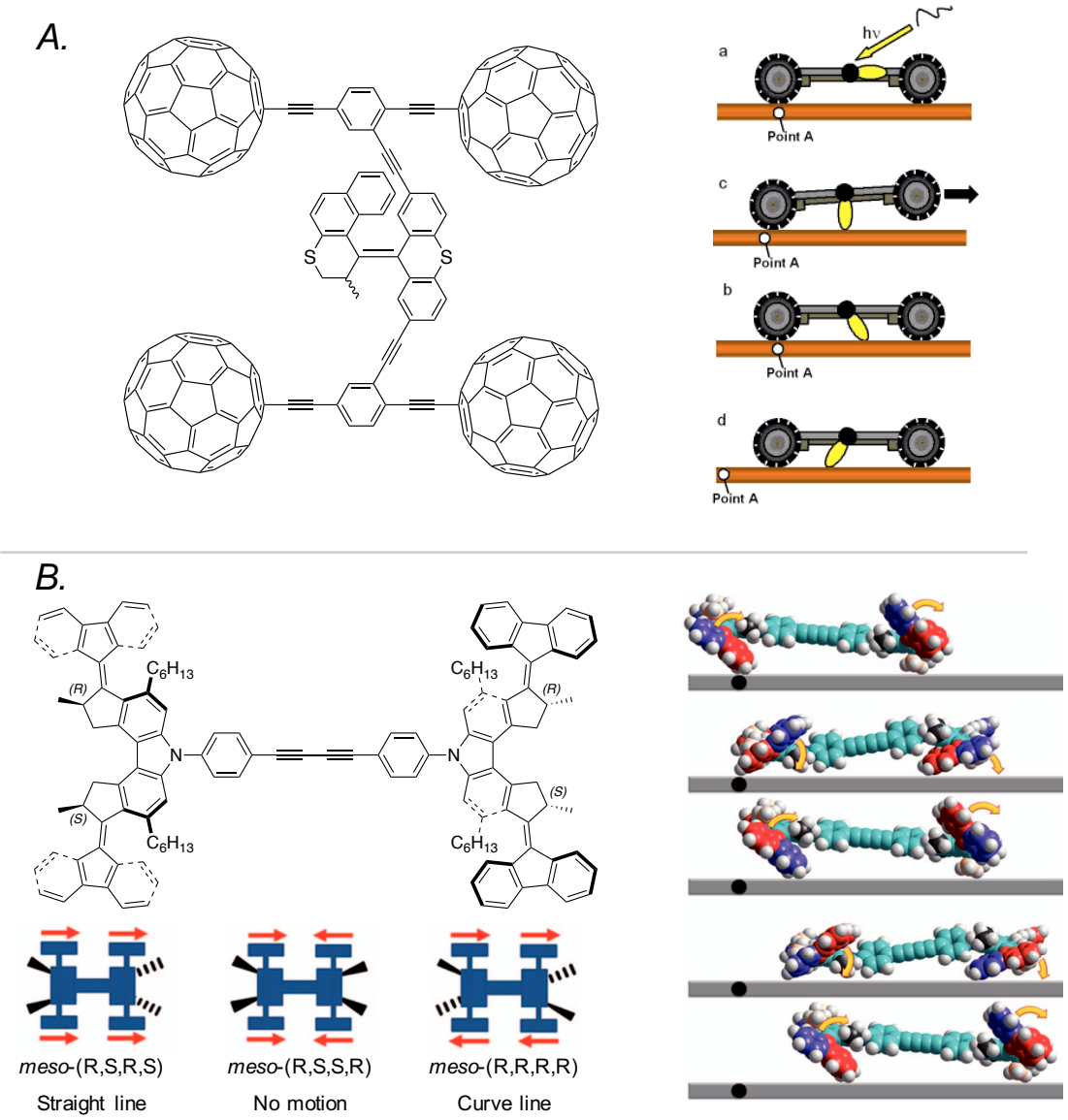

Figure I.16 A. Molecular structure of the first nanocar incorporating a molecular motor in the central axle and its corresponding propulsion scheme when fuelled under 365 nm light irradiation. The motor was supposed to generate a skipping motion propelling the structure forward. Adapted from ref 102. **B.** Molecular structure of the tetra-motor-based nanocar and representation of the corresponding model when powered by the scanning tunnelling microscope. The configuration of the various chiral centres dictates the overall motion of the system. Adapted from ref 103.

Inducing movement at a higher length scale is more complex and requires the organisation of a set of molecular motors in such a way that their tiny displacements can be combined and amplified. In this context, liquid crystals are of major interest, since they are characterised by highly organised phases that are sensitive to the slightest disturbance. Thus, in 2006 the group of Feringa showed that in the case of a cholesteric liquid crystals film, the presence of a 1 wt.% enantiopure molecular motor as dopant is sufficient to orient the helicity of the nematic phase (**Figure I.17**).[105] When placed under UV irradiation, photo-isomerization pushes the motor

towards a photostationary state that results in a change of its overall helicity. This local shift leads to a reorganization of the whole system. This local change induces a clockwise rotation of the LC film that can be visualised macroscopically with a small glass rod. After 10 minutes, the movement gradually ceases, as the system has reached a steady state. A subsequent stop of the irradiation allows the motor to return to its stable state by thermal helix inversion and to recover its initial helicity. Consequently, a second reorganisation of the liquid crystal takes place, this time resulting in an anti-clockwise rotation until a new equilibrium is reached.

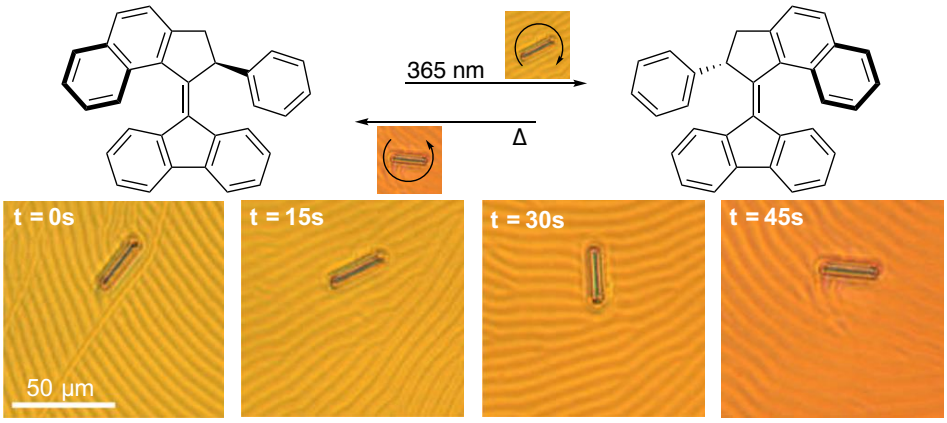

Figure I.17. Molecular structure of the motor used as dopant in a LC film before and after UV irradiation. Optical microscope pictures show the motion of a small glass rode on a cholesteric liquid crystal film at different time while irradiating. Adapted from ref 105.

Self-organising systems are also sensitive to small changes in size and/or shape, and are therefore ideal for observing the motion of molecular motors on a macroscopic scale. In 2018, team of Feringa synthesized an amphiphilic motor functionalized by lipophilic dodecyl chains on the rotor and two hydrophilic carboxyl moieties on the stator (**Figure I.18**).[106] In water, this molecule self-assembles into hierarchical nanofibers containing only 5 wt.% of motors. Placed in an aqueous solution containing $CaCl_2$, these supramolecular structures can stack with each other to form centimetre-sized macroscopic fibrillar edifices. Extensive UV irradiation resulted in a photostationary state where the motors are mainly photoisomerized into unstable isomers. Their different shape disorganises the alignment of fibres, resulting in a local increase of the occupied volume and consequently in a reduction of its length. Macroscopically, a torsion of the thread up to an angle of 90° is observed on the most irradiated side. Interruption of the illumination coupled with heating causes the reformation of the starting isomer, allowing the material to recover its initial shape over a course of three hours. Although slow, this photo-actuation has been proven effective both in water and in the open air. However, re-irradiation of the system results in a twist of only 45°. This difference seems to be attributed to the instability of the supramolecular string at high temperatures. Nevertheless, this photoactivated muscle can lift loads in the milligram range and move them with precision in space.

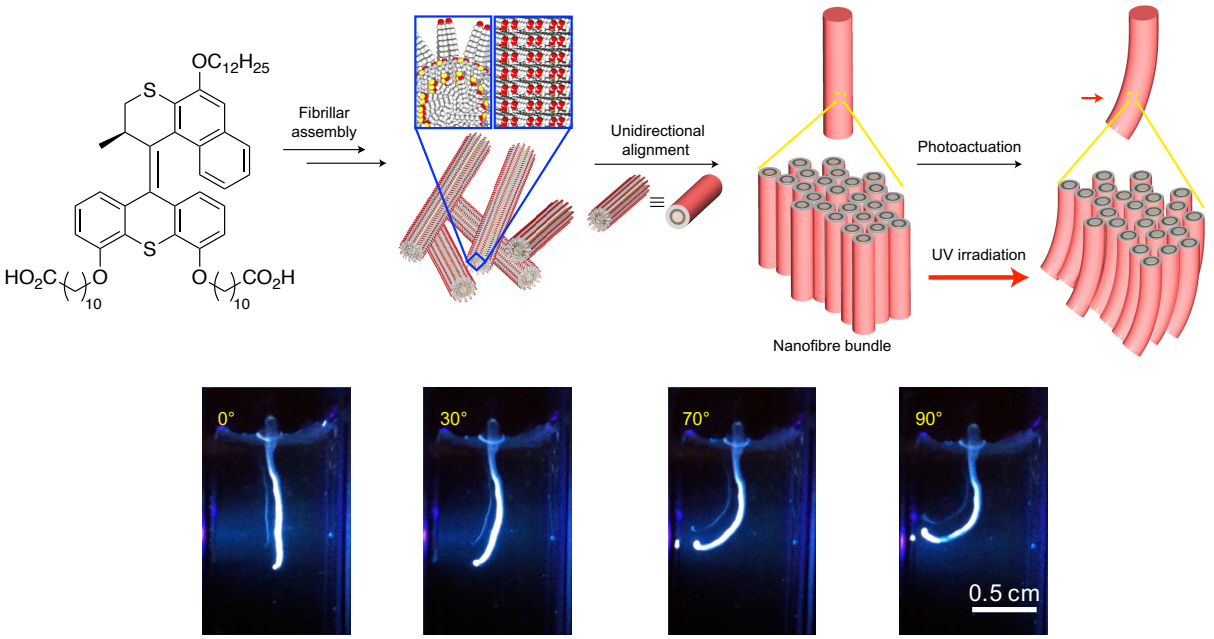

Figure I.18. Molecular structure of the amphiphilic motor and schematic representation of its self-assembly at the micro and macro scale. The snapshots show the actuation of the material in water and its progressive torsion toward the light source within a time frame of 60s. Adapted from ref 106.

At this point it should be noted that the aforementioned examples, although ingenious, do not ultimately take advantage of the work produced by the molecular motors. In both cases, the crowded alkene is placed in a photostationary state and it is the change in the physico-chemical properties of the different isomers that generates a motion. As the return to the initial state is followed by a loss of the generated work, the motor could almost be considered as a simple photoswitch operating between a stable and a metastable state. In this regard, our group has developed a system capable of macroscopic motion while simultaneously storing the work produced by the motor (**Figure I.19**).[6] To do so, a tetrafunctionalized second-generation motor derivative, characterised by two fixation points placed on both the rotor and the stator, was synthesised. This unit was then integrated into a covalent polymer network as cross-linking point, leading to the formation of a centimetre-sized chemical gel. When placed under UV irradiation, the unidirectional rotation of the motors drives the system out of equilibrium causing the polymer chains to wind around each other. This coiling results in a decrease of the apparent chain length which causes a macroscopic contraction of the material. At each cycle, work is stored in the form of mechanical tension through the twisting of the polymers. However, a prolonged exposure to UV light causes excessive strain which results in the rupture of the network.

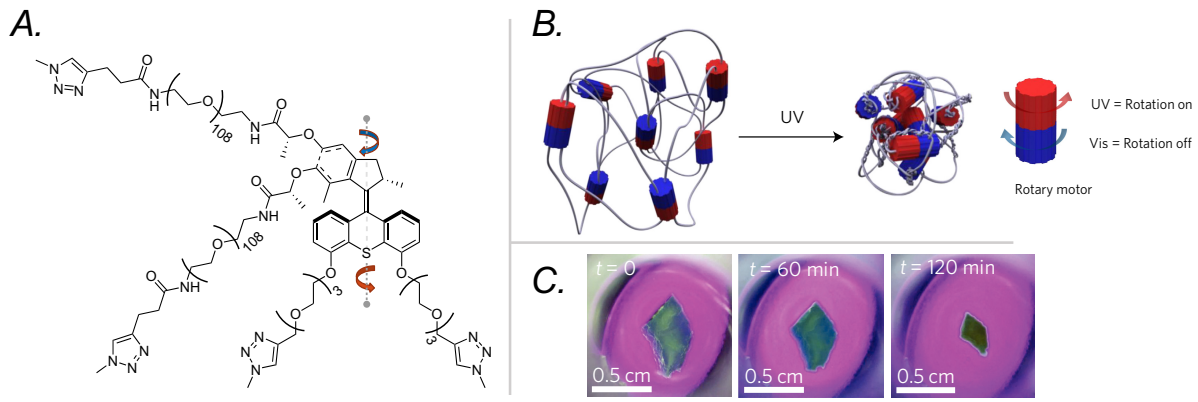

Figure I.19 A. Molecular structure of the tetrafunctionalized motor within the chemical gel. **B.** Schematic representation of the contraction of a gel upon UV irradiation. **C.** Snapshots of the contraction over time. Adapted from ref 6.

One major limitation of this system lies in its inability to release the stored energy except by its own degradation. A solution has therefore been developed, which consists in integrating a so-called "modulator unit" to make the contraction reversible (**Figure I.20**).[7] To this end, a tetrafunctionalized diarylethene derivative was incorporated into the network as a new cross-linking centre. This well-known photoswitch is characterised by the formation of freely rotating bonds in its open form that allows the polymer chains to gradually untwist, thus releasing the stored energy. This sigma bond can also be selectively blocked by cyclisation upon UV irradiation. Thus, at these wavelength, when the modulators are closed and the motors turn, the gel contracts while it returns to its original shape when placed under visible light. Such a system is definitely promising as an actuating unit in the development of soft robotics.

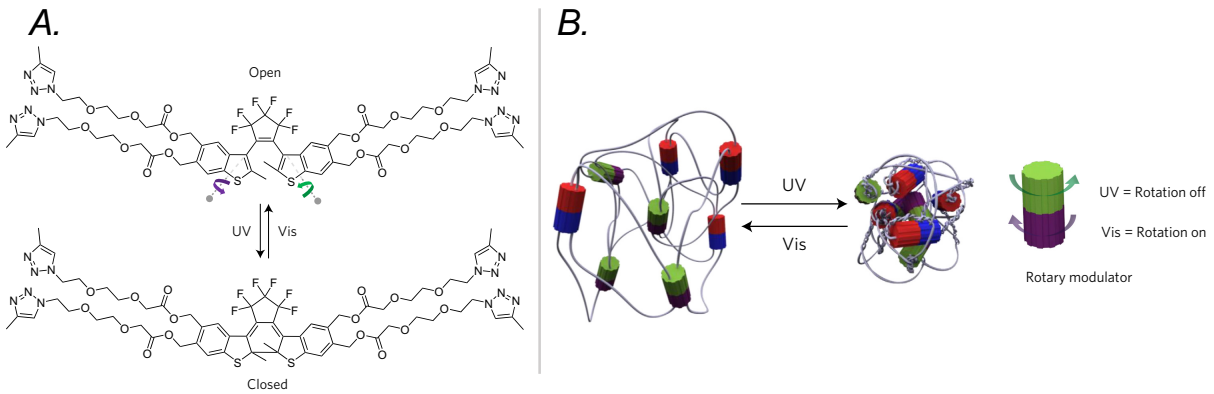

Figure I.20 A. Molecular structure of the tetrafunctionalized diarylethene in its open and closed form. **B.** Scheme depicting the reversible contraction of the gel upon UV and visible light irradiation. Adapted from ref 7.

The chemistry of molecular machinery is a relatively new field but is clearly in full expansion. Many developments have been carried out to design new motor units and much effort is put

into developing structures that take advantage of the full potential of these nanoscopic devices. In this context, Feringa's crowded alkene-based motor is a powerful and versatile tool. Requiring nothing more than light irradiation to operate, it can easily be incorporated into a variety of systems, ranging from liquid crystals to self-assemblies and, of course, polymers.

My work during this thesis focused on the exploitation of this tetra-functionalized motor through two different topics. The first one consisted in developing contractile gels operating at higher wavelengths, in order to limit the degradation inherent to the use of UV but, above all, to make our system compatible with a wider range of modulators of interest. The second part of my research aimed at propelling nanoobjects with light. For that, in collaboration with two other groups, we designed a system consisting of molecular motors anchored on Janus nanoparticles and studied their motion mainly by light scattering experiments.

Chapter II. **Motor Synthesis and Scale-Up**

II.1. Introduction

Since the discovery of the first light-fuelled rotary molecular motors by the team of Pr. Ben L. Feringa in 1999,[1] the molecular structure of this artificial system has been continuously improved over time. As mentioned in the bibliographic introduction, the main feature of interest has been the speed of rotation. But its exploitation in functional devices depends as much, if not more, on its ability to be functionalized. Indeed, a motor isolated in solution greatly limits its potential use. Conversely, its integration into a larger system via covalent or supramolecular interactions offers a much wider range of applications. Thus, most of the examples we have previously presented required the presence of two to four attachment points. For this purpose, the second generation of molecular motors is particularly suitable. Indeed, the natural asymmetry between the stator and the rotor greatly facilitates the implementation of orthogonal groups and the rotation speeds are generally quite high, reaching up to the MHz range.[4]

The light-driven motor, that has been used during my thesis, is adapted from this second generation. Fast responsiveness is indeed essential for the development of smart materials. However, as it has already been discussed in the general introduction in order to incorporate this molecule into a network our system needs to carry four reactive moieties. To do so, two carboxylic acids and two phenols, placed respectively on the rotor and the stator, have been incorporated (**Figure II.1**). These groups are initially orthogonally protected, thus allowing an asymmetric functionalisation of this molecule. So far polyethylene glycol chains has been predominantly used to functionalize the motor, since they are quite flexible and soluble in most solvents. Modification of the nature of the polymer chain and its influence on the properties of the resulting material are currently investigated in our group.[6,7] Formation of a light-responsive chemical gel occurs after click reaction between the functionalized motor, which acts as reticulating units. Overall, our system was shown to require the presence of around 1 mg per gel of molecular motors in order to have a good responsiveness to light. As the synthesis of handleable materials typically requires a significant amount of motors, we decided to embark in an extensive scale-up of the motor. This work was performed in collaboration with Alexis Perrot, PhD student in our group. Our objective was to obtain at least 40 g of protected molecular motor before functionalization with polymer chains, which is almost twenty times more than the first scale-up previously published by our group.[8]

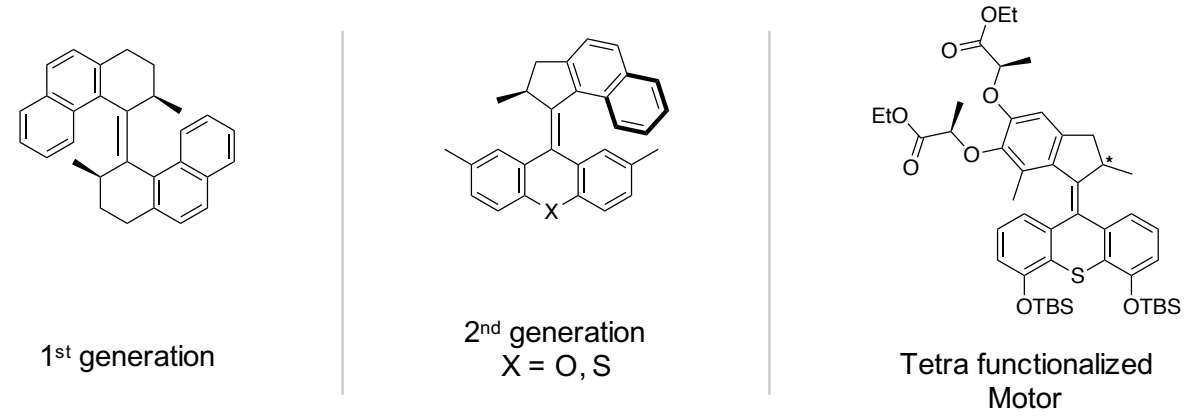

Figure II.1 Molecular structure of the 1st and the 2nd generation motor and the tetra functionalized motor developed by our research group.

II.2. Synthesis

II.2.1. Retrosynthetic Scheme

The synthesis of the orthogonally protected molecular motor is convergent, arising from a Barton-Kellogg coupling as main step between the upper and bottom parts (**Figure II.2**).

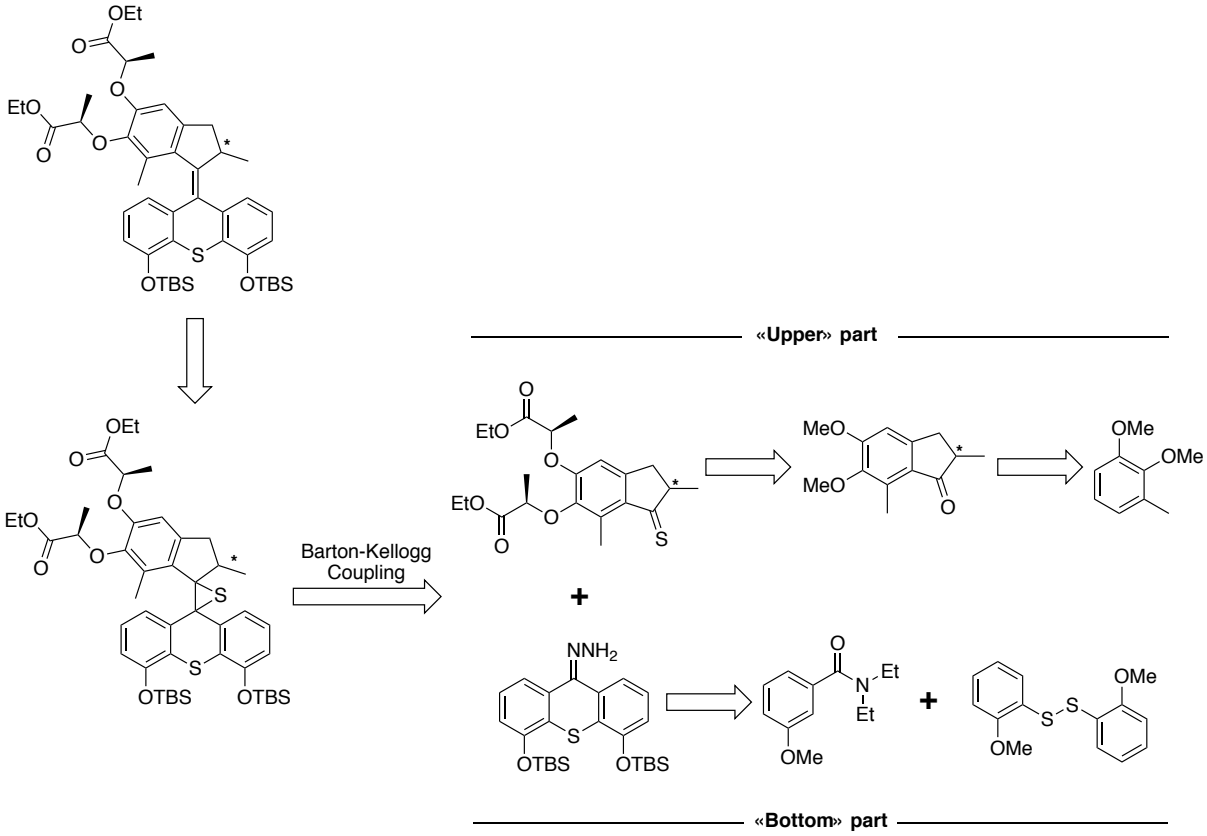

Figure II.2 Retro-synthesis of the orthogonally protected molecular motor.

The upper part was obtained via a Mitsunobu reaction on a dihydroxyindenone, itself formed after a Friedel-Crafts type reaction from dimethoxytoluene. On the other hand, the lower part was formed by a Snieckus reaction between a disulfide and a methoxybenzamide. The episulfide resulting from the coupling reaction is inert to UV and must then be reduced in order to form the expected light-fuelled rotary system. However, the latter is far less stable over time, as the central double bond tends to get oxidised. Therefore, the motor is usually stored under its episulfide form. In addition, as the configuration of the stereogenic centre present on the motor controls the direction of the rotation, it is fundamental to completely separate the diastereomers in order to isolate optically pure compounds. This separation is done on the episulfide via a silica gel chromatography column, thanks to the presence of two chiral centres on the side chains. Their presence avoid the use of a preparative HPLC or a chiral column chromatography, which are both quite expensive and in most cases poorly adapted to a multigram-scale project. Functionalization of the molecular motor with polymer chains occurs through successive deprotection and coupling reactions of this orthogonally protected molecular motor. These reactions can also be performed on the episulfide precursor in order to access a reference compound inert to UV irradiation.
All the synthetic work will now be detailed starting from the bottom and upper parts, before focusing on the Barton-Kellogg coupling and the consecutive reduction and deprotections. Further functionalization with appropriate chains will be presented in the next chapters.

II.2.2. Synthesis of the stator

The lower part of the motor was obtained by a seven-step convergent synthesis (**Scheme II.1**), starting with the oxidation of 2-methoxythiophenol. This reaction tool place in water, using iodine dispersed in MeOH as oxidant. The reaction proceeded overnight at room temperature and resulted in the formation of around 280 g of the bis-methoxyphenyl disulfide **1** in four consecutive batches in quantitative yield.
In parallel, 3-hydroxybenzoic acid was converted to hydroxybenzamide **2** in two consecutive steps. First, the carboxylic acid was treated with a large excess of thionyl chloride, which was also used as a solvent, and heated at reflux for 4 h. This approach led to the formation of a highly reactive acyl chloride which could be easily isolated by evaporation, removing the remaining reagent/solvent and the by-products, *i.e.* hydrogen chloride and sulphur dioxide.
This intermediate could then be used without further purification in the nucleophilic substitution reaction with diethylamine, which took place in DMF at 0 °C. Overall, about 140 g of hydroxybenzamide **2** was formed in three consecutive reactions in an almost quantitative yield.
Protection of the phenolic moiety was then carried out overnight in acetone using iodomethane and potassium carbonate at room temperature to give around 147 g of the corresponding methoxybenzamide **3** in two batches in quantitative yield.

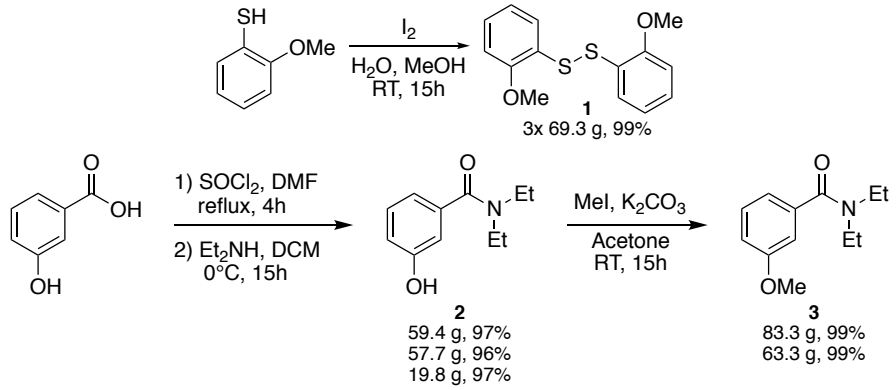

Scheme II.1 Synthesis of disulfide **1** and benzamide **3** precursors.

These two precursors were finally condensed together in a directed *ortho*-metallation, also known as the Snieckus reaction (**Scheme II.2**). First, an aryllithium intermediate was formed by the addition of *sec*-butyllithium and tetramethylethylenediamine in THF at -78°C for 2 h. The methoxy and amide groups are well known to facilitate lithiation in the *ortho* position, making the reaction highly regioselective. Next, disulfide **1** was added to the newly created nucleophile to form 56.6 g of thioether-amide **4** in three pots in a reasonable yield. A ring closure reaction at -78°C in THF with slow addition of *n*-butyllithium led to the formation of about 98 g of the ketone **5**. The regioselectivity of this cyclization reaction is enhanced by the proximity of the methoxy moiety from the benzamide ring. Some impurities remained present in the mixture, hence a measured yield over 100%. Fortunately, the following reaction is quite selective, thus no further purification was performed.

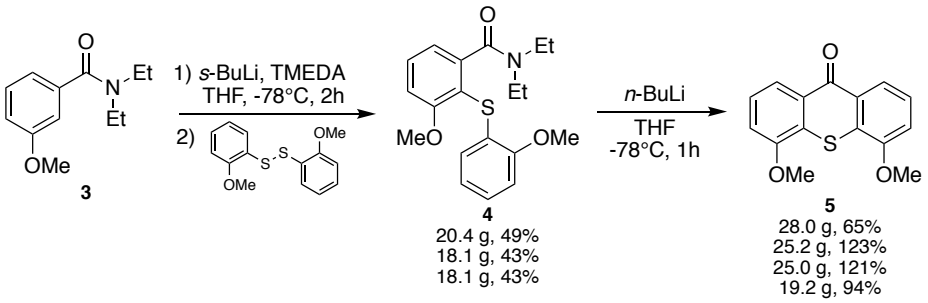

Scheme II.2 Synthesis of ketone **4** through a Snieckus reaction followed by a ring closure step to form **5**.

With the main stator architecture created, the methoxy groups were replaced by *tert*-butyldimethylsilyl ethers (**Scheme II.3**) to allow orthogonal protection with the rotor and thus more complex functionalizations of the final molecular motor. To this end, the two phenols were first deprotected using BBr_3 at 0°C. The resulting intermediate was isolated by simple evaporation and then solubilised in THF before being stirred overnight at room temperature in the presence of *tert*-butyldimethylsilyl chloride and imidazole. After purification on a silica gel chromatography column, around 86 g of the protected ketone **6** was obtained in good yield in two batches. Finally, the ketone was converted into a hydrazone according to a two-step process. In the first step, a thioketone was formed using P_2S_5 at 65°C for one hour. This

molecule is sensitive to light and air, so it is essential to keep the reaction mixture under inert gas and start the next reaction as soon as possible. The crude was thus simply washed with dichloromethane before being dissolved in ethanol. Hydrazine was then added at 0°C and the mixture was stirred for a further hour. An alumina gel chromatography column afforded around 43 g of hydrazone **7** over four batches in moderate yield, ready for use in the Barton-Kellogg coupling.

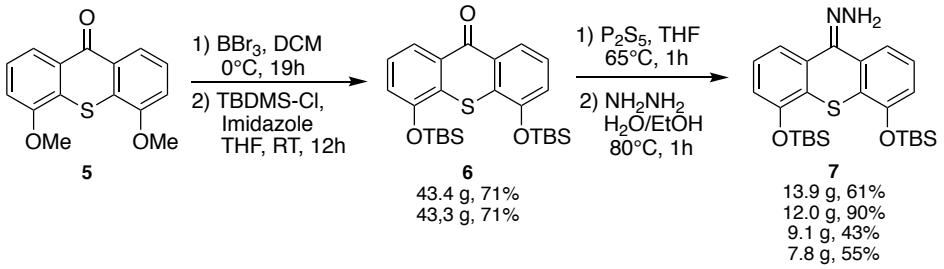

Scheme II.3 Synthesis of TBS protected ketone **6** and of hydrazone **7**.

II.2.3. Synthesis of the rotor

The synthesis of the upper part of the motor was achieved in four steps (**Scheme II.4**). The first one was a Friedel-Crafts type reaction where 2,3-dimethoxytoluene and methacrylic acid are mixed together in polyphosphoric acid (PPA) at 70°C. Due to the important viscosity of the PPA, even at high temperature, a mechanical stirring was required. After recrystallisation 102 g of indanone **8** was obtained as a racemic mixture in good yield.

The two methyl ethers could thereafter be removed in the presence of boron tribromide in dichloromethane at 0°C. The slow addition of methanol at -78°C allowed removal of impurities and of the excess of reactant through the formation of volatile trimethyl borate and hydrogen bromide. Thus, a total of 98 g of bis-phenol indenone **9** was collected from three simultaneous pots with an almost quantitative global yield.

The following reaction consisted in the introduction of a chiral moiety in the system in order to create diastereomers which, unlike simple enantiomers, can eventually be separated through non-chiral chromatography. Such approach is novel compared to synthetic routes developed by the group of Feringa who relies mostly on chiral chromatography or preparative HPLC. Indeed, it is essential to isolate enantiopure compounds as the configuration of the stereocenter at the vicinity of the ketone completely controls the unidirectionality of the rotation. In our synthetic approach, (*L*)-lactic ethyl ester was condensed on the bis-phenol via a Mitsunobu reaction, using diisopropyl azodicarboxylate (DIAD) and triphenylphosphine as reagents. This synthetic procedure allowed the formation of around 40 g of bis-ester **10**, with a modest yield of 40%, mainly due to the purification protocol. Indeed, triphenylphosphine oxide and DIAD derivatives are very difficult to remove from the crude and took several crystallisations and multiple silica gel chromatography columns were necessary to obtain the product with a satisfactory purity.

The isolated ketone could then be converted, in the presence of phosphorus pentasulfide in toluene at 80°C, into 21 g of the thioketone **11** in three pots with a good yield. Purification by silica gel chromatography was required but difficult to perform since the obtained product is sensitive to both air and light. This last step is albeit necessary in order to achieve an efficient Barton-Kellogg coupling, as it increases the electrophilicity of this precursor.

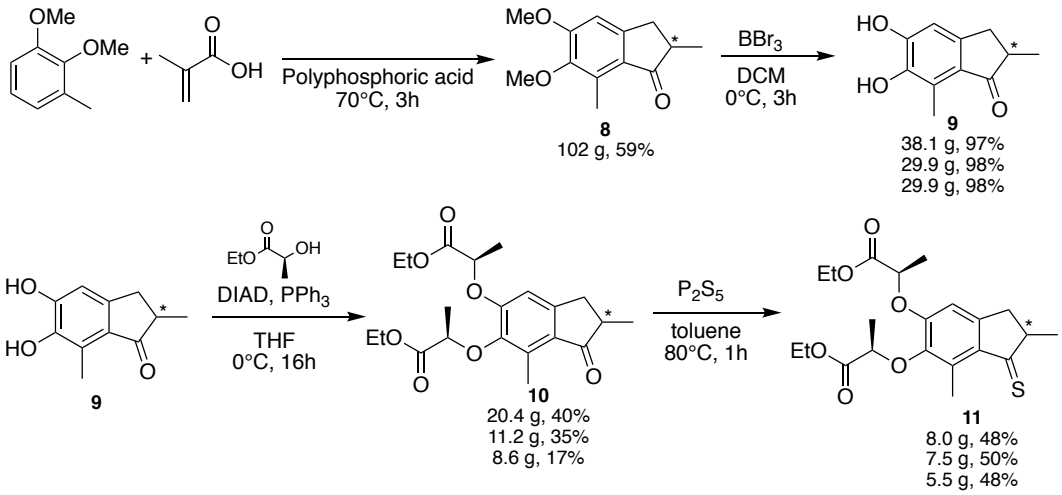

Scheme II.4 Synthesis of the upper part of the motor after cyclisation, deprotection, functionalization and activation.

II.2.4. Barton-Kellogg coupling

The Barton-Kellogg coupling is the key reaction of this synthesis (**Scheme II.5**). It allows the formation of an episulfide through the reaction of a hydrazone with a thioketone. In our case, the stator and the rotor are brought together to obtain the central structure of the molecular motor. The first step consisted in the oxidation of hydrazone **7** into a diazo compound by adding Manganese (IV) oxide in THF at 0°C for one hour. In order to minimise the presence of water in the system, sodium sulphate was also placed in excess. The newly formed diazo derivative was then filtered and transferred using a homemade cannula with cotton wool attached to one end into a second flask containing freshly prepared thioketone **11** solubilised in THF. This step was particularly complicated by the fact that both precursors are sensitive to air and light, so it was necessary to coordinate their synthesis in order to make them react with each other as quickly as possible. The reaction mixture was then stirred overnight at room temperature to form episulfide **12**. At this stage, the two diastereomers (*R*,*R*,*R*) and (*R*,*R*,*S*) were obtained as a racemic mixture. Thanks to the presence of chiral auxiliaries on the rotor, 20 g of each diastereomer were obtained in four pots and isolated through a non-chiral silica gel chromatography column with a good overall yield of 70% over the two steps.

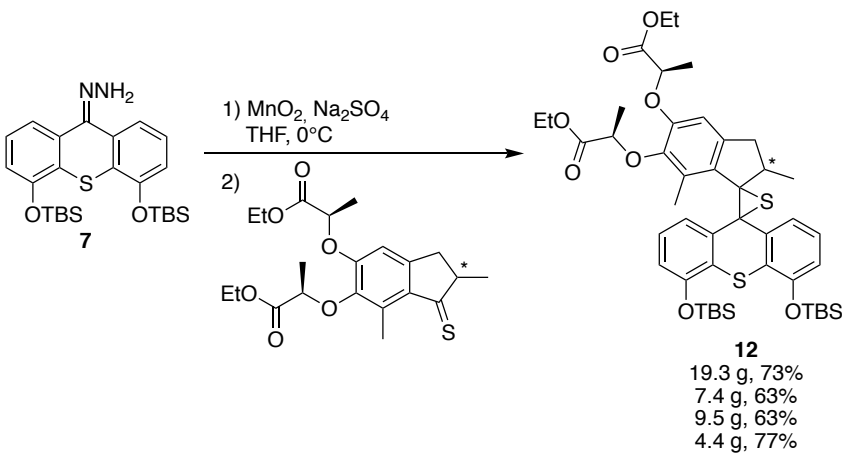

Scheme II.5 Synthesis of episulfide **12** through Barton-Kellogg coupling.

At this point it is important to note that the following reactions are no longer part of the scale-up. As mentioned earlier, the motor is usually stored in its episulfide form, so the scale of the following steps was adapted depending on the objective of each project.

II.2.5. Reduction and deprotections

With the main architecture finally constructed, it was then necessary to reduce the episulfide **12** into an alkene in order to obtain a light responsive molecular motor (**Scheme II.6**). This was achieved by adding triphenylphosphine which, after a day at reflux in toluene, captured the sulphur atom of episulfide **11** forming triphenylphosphine sulphide. As a result, up to 867 mg of tetra-protected motor (*R*,*R*,*R*) **13** were obtained in a very good yield.

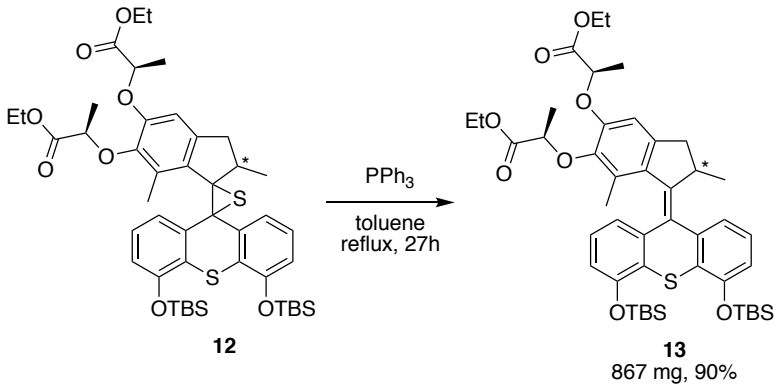

Scheme II.6 Synthesis of tetra-protected motor **13** by reduction of the episulfide bridge.

The resulting motor **13** is orthogonally protected on its upper and bottom parts with two ethyl esters on the rotor and two *tert*-butyldimethylsilyl ethers on the stator. This orthogonality allows to selectively deprotect one of them preferentially depending on the nature of the project. For this reason, two different approaches have been developed to deal with each scenario (**Scheme II.*7***).

The first method involved deprotection of the phenols after addition of tetrabutylammonium fluoride in THF at 0°C. Due to the high affinity between fluorine and silicon atoms, this reaction is fast, selective and quantitative, allowing the isolation of 162 mg of product **14** by silica gel chromatography column. Following a potential functionalization of this compound, the saponification reaction generally occurred in a mixture of THF and MeOH after addition of sodium hydroxide, while stirring at 40°C overnight and resulted in the formation of the bis-carboxylic acid **16**, usually with excellent yield. The purification protocol for this step depends mainly on the nature of the attached groups but in most cases simple liquid-liquid extraction was sufficient to isolate the product of interest.

The second method, which was used in this thesis, consists in hydrolysing first the esters using trimethyltin hydroxide in dichloroethane. This reagent is a milder alternative to the usual basic conditions which are less selective and would therefore lead to the deprotection of the silyl ethers. After heating to 100°C by microwave for six hours, 92 mg of bis-carboxylic acid **15** were obtained in quantitative yield. After possible functionalisation of this upper part, through amidation in most cases, the next step consisted in deprotecting the phenol groups using TBAF at 0°C in THF allowing the formation of 35 mg of compound **16** in quantitative yield.

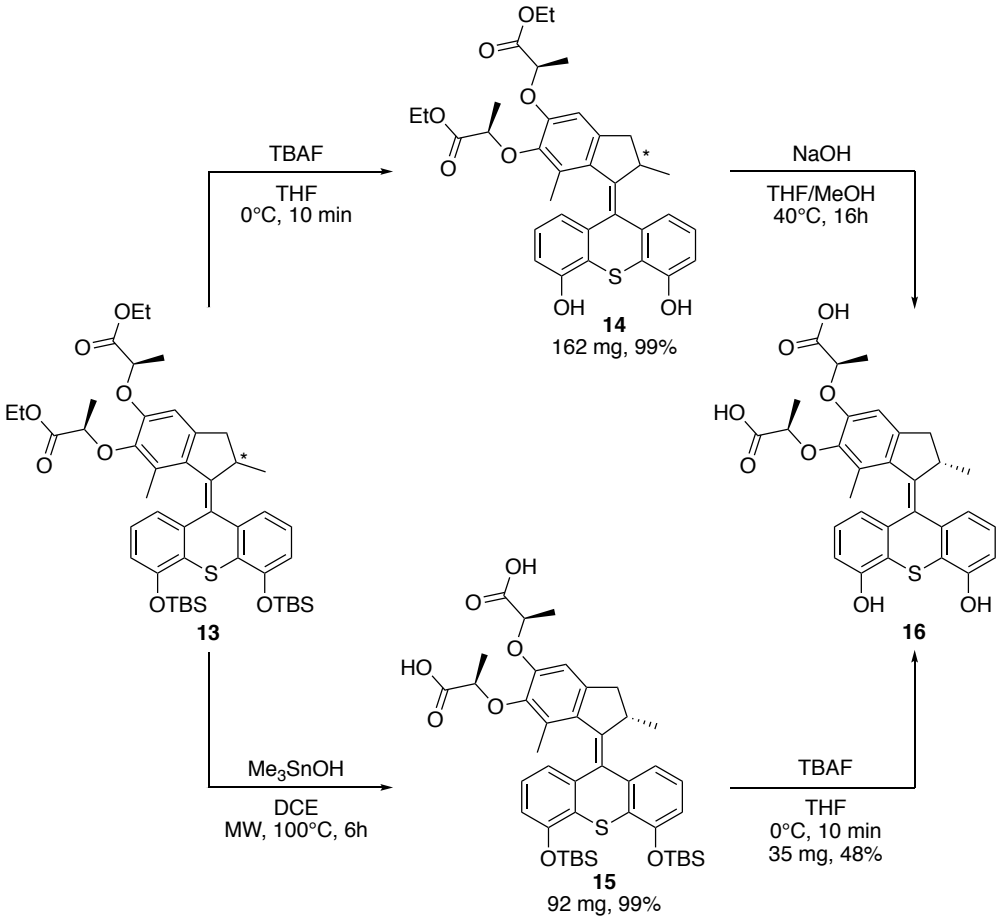

Scheme II.7 Orthogonal deprotection of the tetra-protected motor.

Overall, the synthetic scale-up of the orthogonally protected molecular motor resulted in the obtention of more than 40 g of ready-to-use episulfide **12**, which is 20 times more than what was previously reported. The resulting motor **13** constitutes the key building block for the development of new light sensitive systems and materials targeted during the course of my PhD.

Chapter III. Visible light induced gel contraction

III.1. Introduction

As highlighted in the bibliographic introduction, light-powered machines stand out by their autonomy, such as in A. Credi's molecular pump,[50] but also by their high rotational speed for Feringa's crowded alkenes, the fastest of which can reach the MHz range.[4] Light is a particularly powerful tool as it is non-invasive and yet easily controlled in time, space and intensity. In the case of double-bond motors, UV irradiation is usually required to generate motion. At these wavelengths, the light is energetic enough to cause a number of undesirable effects. Damage can occur either at the molecular machine or in its environment through the formation of free radicals and their subsequent photo-oxidation.[107,108] Besides their incompatibility with biological environments, UVs are not selective since they interact with a wide range of chemical functions, resulting in a low penetration coefficient in most materials. In the case of the contractile gels developed by our team,[6,7] this translates into degradation of the polymer network as well as incompatibility with certain modulators of interest such as spiropyran[109] or spirooxazine[110]. On the other hand, visible light is harmless, available over a wide wavelength range and selective. It can more easily penetrate materials and is compatible with biological media. However, it remains less energetic, which means that strategies must be developed to enable the rotation of motor units at higher wavelengths.[111]

To this end, we initially thought making use of the well-known two-photons excitation approach (**Figure III.*1*A**).[112,113] However, this method requires powerful laser equipments that are not easily available. Another strategy would consist in modifying the molecular motor structure so as to reduce the HOMO-LUMO gap to more than 400 nm (**Figure III.1B**), which has been achieved with Feringa's oxindole-[114] and Dube's hemithioindigo-based motor.[115] Concerning the more conventional overcrowded alkene-based motor, a red-shift of the excitation could also be obtained by adding donor-acceptor substituents,[116] by extending the aromatic core[117] or by interacting with a transition metal centre.[118] Yet, such approach implies heavy synthetic modifications of the structure of the pre-existing motor and an excitation limited to the blue region of the visible spectrum.[119] Therefore, a third method involving the addition of a photosensitizer has been explored (**Figure III.1C**). A photosensitizer is a chromophore characterized by its ability to transfer its excited state to a nearby substrate by an inter- or intra-molecular process before reverting unaltered to its ground state. It often implies a triplet-excited state because of their inherent prolonged lifetime, hence increasing probability of interaction with close-by substrates. This alternative offers a wider absorption range by matching the selected excited-state energy level of the substrate with a suitable chromophore, and greatly reduces the amount of synthetic work, since it is sufficient to add a photosensitizing agent in solution to observe its effects. Inspired by the pioneering work of Feringa's team,[9,120] the addition of a porphyrin-based photosensitizer and the corresponding

intermolecular triplet-state energy transfer to molecular motors was investigated at first in solution and then integrated into a contractile gel.

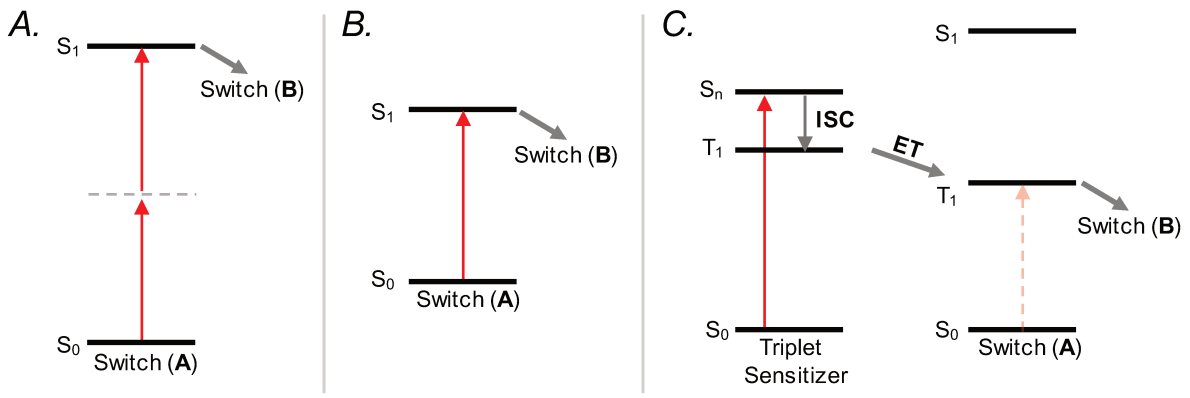

Figure III.1. Diagrams illustrating the different approaches to reduce energy input in order to trigger isomerisation. **A.** Two-photon excitation. **B.** HOMO-LUMO gap reduction by modification of the motor structure. **C.** Triplet sensitizer energy transfer where the excitation is followed by an intersystem crossing (ISC) and then eventually by an energy transfer (ET). Adapted from ref 111.

III.2. Results and Discussion

III.2.1. System design

Taking into account the encouraging results reported by Feringa's team as well as structural similarities shared between their motors and those integrated in our gels,[6,7] we also chose to use Pd(II)-tetraphenylporphyrin **17** (Pd-TPP) as a photosensitizer. This fairly common chromophore can easily be synthesised from the commercially available tetraphenylporphyrin (**Scheme III.1**).

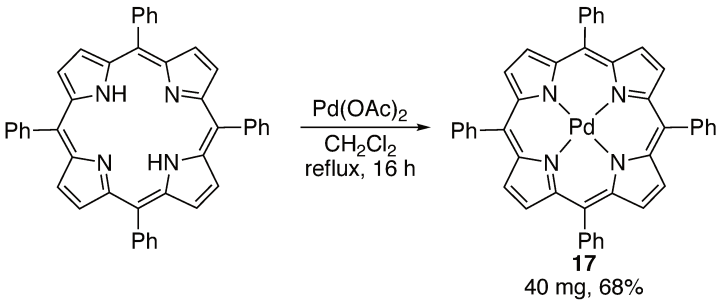

Scheme III.1 Synthesis of Pd-tetraphenylporphyrin **17**.

This compound is characterized by two strong absorption peaks at 400 nm and 530 nm, corresponding to the Soret peak and the Q-band respectively (**Figure III.2A**). They are both able to bring this porphyrin to a triplet excited-state remarkable for its relatively long lifetime (≤ 2 ms) and an energy level close to that of the triplet excited-state of Feringa's motor (178 kJ.mol^{-1} for Pd-TPP & 182 kJ.mol^{-1} for the motor).[9,121] This proximity allows an efficient

energy transfer from the photosensitizing agent to the motor which, in turn, is able to reach its first triplet excited state, leading to the formation of an unstable form (**Figure III.2B**). By thermal helix inversion a new stable isomer is obtained. Again, a Pd-TPP triggered photoisomerization followed by a second thermal relaxation completes the rotational cycle by reforming the starting isomer **(Figure III.2C**).

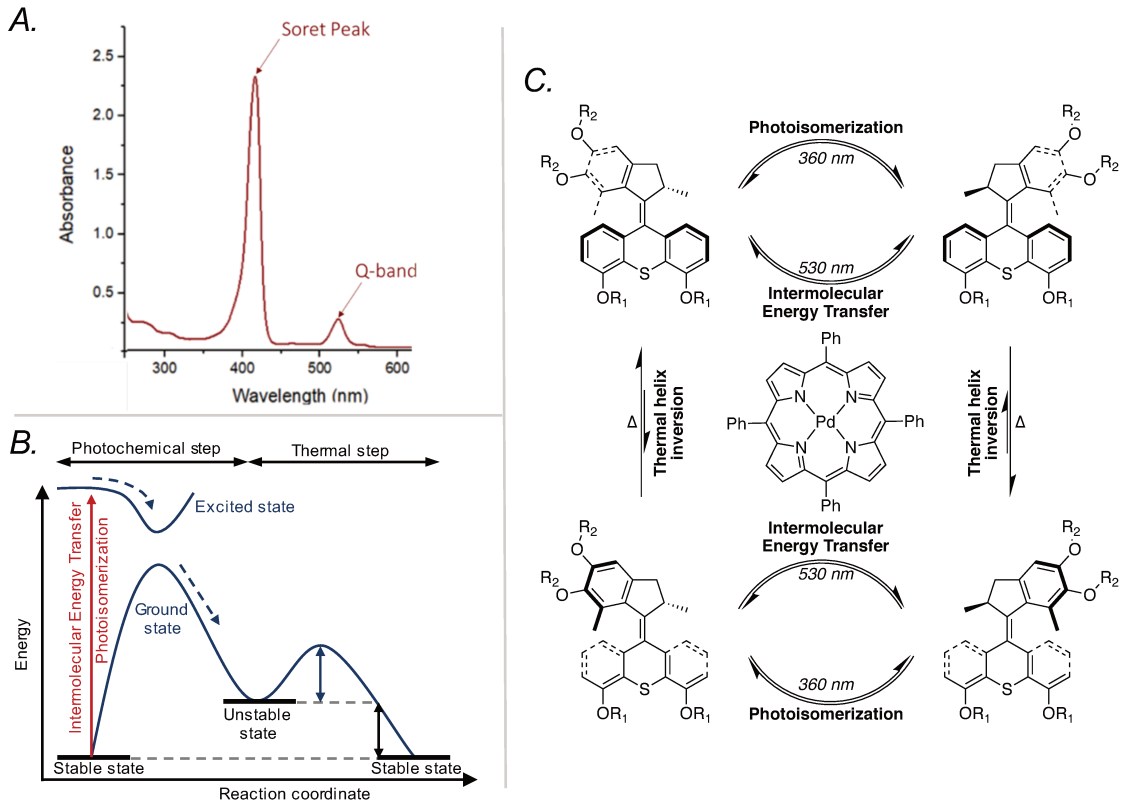

Figure III.2 A. Pd-TPP absorption spectrum (10 µM in $CHCl_3$). **B.** Simplified energy diagram of a motor. Adapted from ref 6. **C.** Mechanisms of the motor rotational cycle in the absence of presence of Pd-TPP as photosensitizer. R1 and R2 can either be protecting groups (*i.e.* TBS and Et) or PEG polymer chains.

Although already described in the case of isolated molecules in solution, this process may still present some discrepancies due to the effect of the multiple ether bridges, used here as linkers, on the energy levels of the tetra-functionalized motor. Furthermore, photo-actuation by energy transfer of a molecular machine capable of producing work by entanglement of polymer chains has not yet been explored. For these reasons, we first studied the interaction of Pd-TPP with our motor in solution before its integration into a chemical gel.

III.2.2. Triplet excited-state energy transfer

Before characterizing the nature of the interaction between the photosensitizer and the motor, it is essential at first to test whether an interaction exists or not. In this context, one can monitor the rotational cycle of the molecular motor in the presence of the

photosensitizer. To do so, we choose to break the symmetry of the lower-part of the system must be broken so that the two stable states can be distinguished by ^{1}H NMR.
The simplest way to achieve such result is to use mono-protected motor **18** that can be easily synthesized from the bis-phenol motor **14** by adding *tert*-butyldimethylsilyl chloride (TBSCl) (**Scheme III.2**). The yield of this reaction was quite low because TBSCl was the limiting reagent in order to avoid the formation of bis-protected motor.

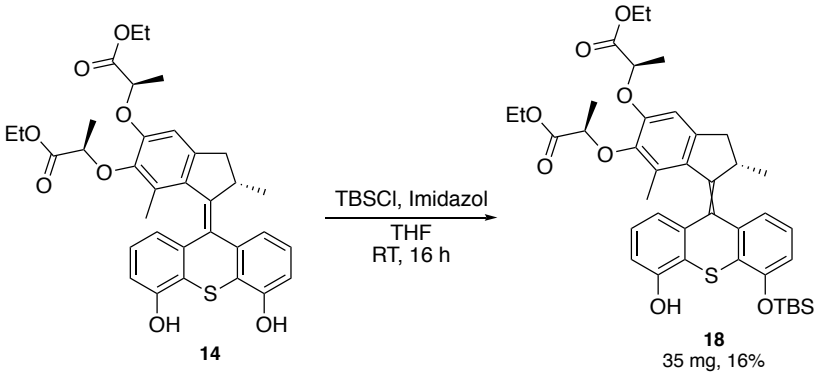

Scheme III.2 Synthesis of asymmetric motor **18**.

Each unstable intermediate could potentially be isolated by reducing the temperature so as to prevent the thermal helix inversion reaction, thus allowing the characterization of the unstable forms while irradiating. Unfortunately, molecule **18** could not be cooled below -78°C, due to its reduced solubility in CD_3OD at these temperature. In addition, at these temperatures, the thermal helix inversion energy barrier can still be easily overcome, as expected for 2nd generation rotary motors that can reach high frequency at room temperature (≤ 3 MHz).[4,122,123] At this point, it should be noted that this theoretical maximum rotational speed is only reached in the case of intense irradiation so that the system remains out of equilibrium. In the case of illumination at lower power, a temporal follow-up of the evolution of the stable form ratio remains possible.[124]
Thus, we separated the **E** and **Z** isomers of motor **18** by HPLC and irradiated one of them in the presence of Pd-TPP (ratio 1:1 at 11.8 mM in $CDCl_3$) with visible light (400-800 nm, 13.8 mW.cm^{-2}) (**Scheme III.3**).

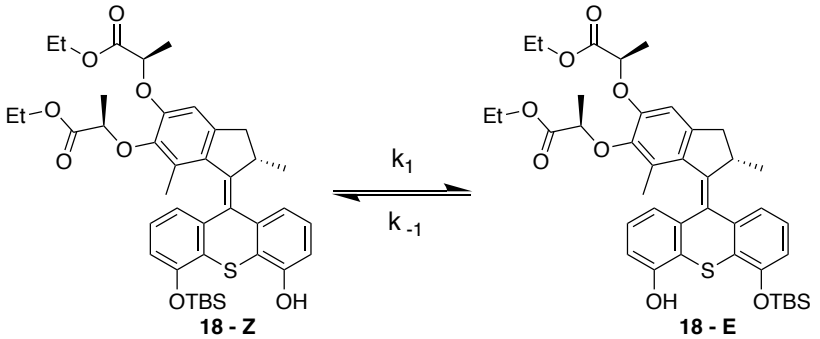

Scheme III.3 Molecular structure of **Z** and **E** isomers of asymmetric motor **18**, k_1 and k_{-1} being their respective kinetic constant of formation.

The evolution was then monitored by ^{1}H NMR, using the integration of the phenolic proton signal as reference and plotting the isomers ratio evolution vs. time (**Figure III.3**). Despite its apparent complexity, involving both reversible photoreactions and unidirectional relaxations, this system can be accurately described using a standard *cis-trans* isomerization model.
The rate of formation of isomer **E** can be written as:

$$\frac{\mathrm{d}[\boldsymbol{E}]}{\mathrm{dt}} = k_1[\boldsymbol{Z}] - k_{-1}[\boldsymbol{E}] \qquad (\text{III.1})$$

At (t = 0), we have:

$$[\boldsymbol{E}] = [\boldsymbol{E}]_0 \text{ and } [\boldsymbol{Z}] = [\boldsymbol{Z}]_0$$

And therefore:

$$[\boldsymbol{Z}] = [\boldsymbol{Z}]_0 - [\boldsymbol{E}]$$

Equation (III.1) can then be written as:

$$\frac{d[\boldsymbol{E}]}{dt} = k_1([\boldsymbol{Z}]_0 - [\boldsymbol{E}]) - k_{-1}[\boldsymbol{E}] \qquad (\text{III.2})$$

At the equilibrium, we have:

$$\frac{d[\boldsymbol{E}]}{dt} = 0 \text{ and } [\boldsymbol{E}] = [\boldsymbol{E}]_{\mathrm{eq}}$$

Applying this to the equation (III.2), we obtain:

$$k_1[\boldsymbol{Z}] = (k_1 + k_{-1})[\boldsymbol{E}]_{\mathrm{eq}} \qquad (\text{III.3})$$

We can then write:

$$\frac{d[\boldsymbol{E}]}{dt} = (k_1 + k_{-1})\big([\boldsymbol{E}]_{\mathrm{eq}} - [\boldsymbol{E}]\big) \qquad (\text{III.4})$$

After a standard resolution of (III.4), we have:

$$-\ln\big([\boldsymbol{E}]_{\mathrm{eq}} - [\boldsymbol{E}]\big) = (k_1 + k_{-1}).t - \ln\big([\boldsymbol{E}]_{\mathrm{eq}} - [\boldsymbol{E}]_0\big) \qquad (\text{III.5})$$

Therefore, by plotting (III.5) as $-ln([\boldsymbol{E}]_{eq} - [\boldsymbol{E}])$ as a function of time (**Figure III.*3*B**), we managed to determine the apparent isomerization rate from the slope:

$k_{iso\ (Vis)}$ = (2.44 ± 0.12)x10^{-4} s^{-1} *where* $k_{iso} = k_1 + k_{-1}$ (13.9 mW.cm^{-2})

This value is of the same order of magnitude as that measured under UV irradiation:

$k_{iso\ (UV)}$ = (6.49 ± 0.26)x10^{-4} s^{-1} (at 365 nm and 7.5 mW.cm^{-2})

These two isomerisation rates may seem relatively low for a system that is able to reach rotational speeds up to the MHz. However, there is a very large difference in light intensity between this experiment and those reported in the literature where powerful pulsed lasers

were used, whereas we relied on simple LEDs.[4] At such low power, only a fraction of irradiated motors isomerise at any given time. The photoisomerisation becomes then the rate limiting step, resulting in an reduced overall constant rate.[124]

To confirm the function of triplet sensitizer for Pd-TPP, a control experiment in the absence of Pd-TPP was also carried out and showed no isomerization over the same period of time (**Figure III.3B**). These experiments demonstrate that interaction between Pd-TPP and the motor are necessary for the isomerization process to occur using visible light.

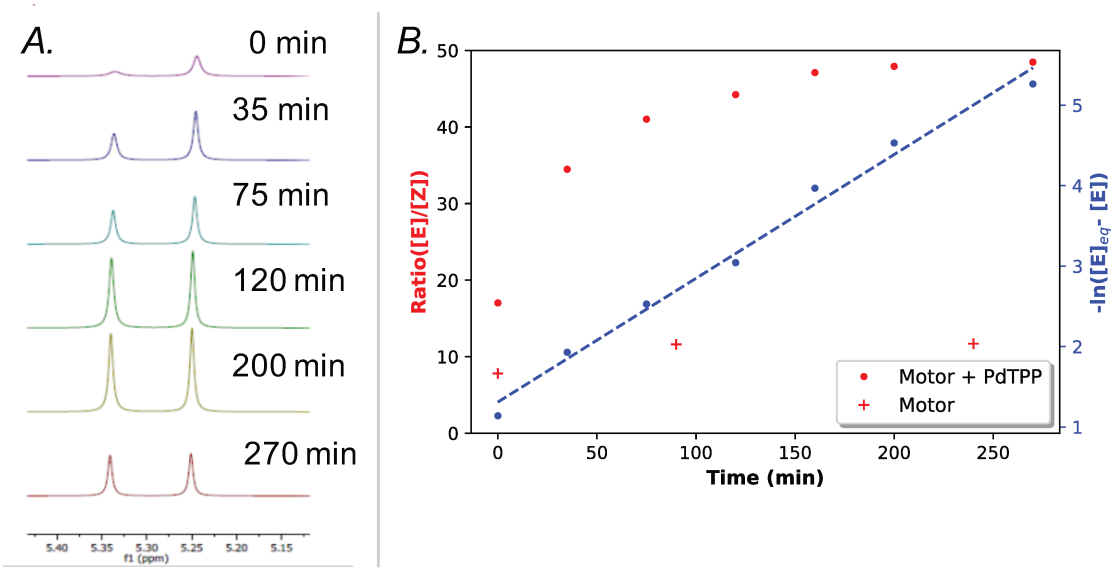

Figure III.3 A. Evolution of the NMR signal of the phenolic proton of motor **18** in the presence of Pd-TPP (both at 11.8 mM in $CDCl_3$) under visible light irradiation (530 nm). **B. Isomer ratio evolution** as a function of time in the presence or in the absence of Pd-TPP and its corresponding **kinetic plot** – Isomerization rate: $k_{iso} = (2.44 \pm 0.12)10^{-4}\ s^{-1}$

During these experiments, we noticed that the presence of oxygen led to a decrease in the rate of isomerization, forcing us to work under an inert atmosphere. Although anecdotic, this observation may indicate that the triplet excited-state of the photosensitizer is involved in an energy transfer process to the motor. Thus, to confirm this hypothesis, a phosphorescence quenching experiment involving tetra-protected motor **13** was performed. Pd-TPP is a chromophore characterized by a fluorescent peak at 610 nm and a strong phosphorescence peak at 700 nm with a measured lifetime of $\tau_0 = 61.95 \pm 0.001$ µs in $CHCl_3$ (**Figure III.4A-B**).

On the one hand, increasing the concentration of tetra-protected motor **13** in solution had no effect on the fluorescent emission at 610 nm, suggesting that the porphyrin singlet excited state is thus not involved in the energy transfer mechanism. On the other hand, a rapid decay of the porphyrin triplet excited-state lifetime and emission intensity was observed (**Figure III.*4*B**). This excited-state quenching can be characterised using the Stern-Volmer relationship that describes these variations in simple terms:

$$\frac{I_f^0}{I_f} = 1 + k_q \tau_0 [Q] \qquad (\text{III. } 6)$$

Here, I_f^0 corresponds to the initial phosphorescence intensity, I_f to the emission intensity in the presence of a quenching agent, [Q] to the quencher concentration and k_q to the quenching rate coefficient.

By fitting I_f^0/I_f as a function of [Q], we determined an extinction coefficient from the slope (**Figure III.*4*C**):

$k_q = (2.87 \pm 0.06)10^7\ M^{-1}.s^{-1}$

This measured value is two orders of magnitude lower than the one reported by Feringa *et al.*,[9] *i.e.* 1.8 x $10^9\ M^{-1}.s^{-1}$, which is close to the diffusion-limited rate. Nevertheless, all our experiments suggest that the interaction between the Pd-TPP and the motor is clearly a triplet excited-state energy transfer.

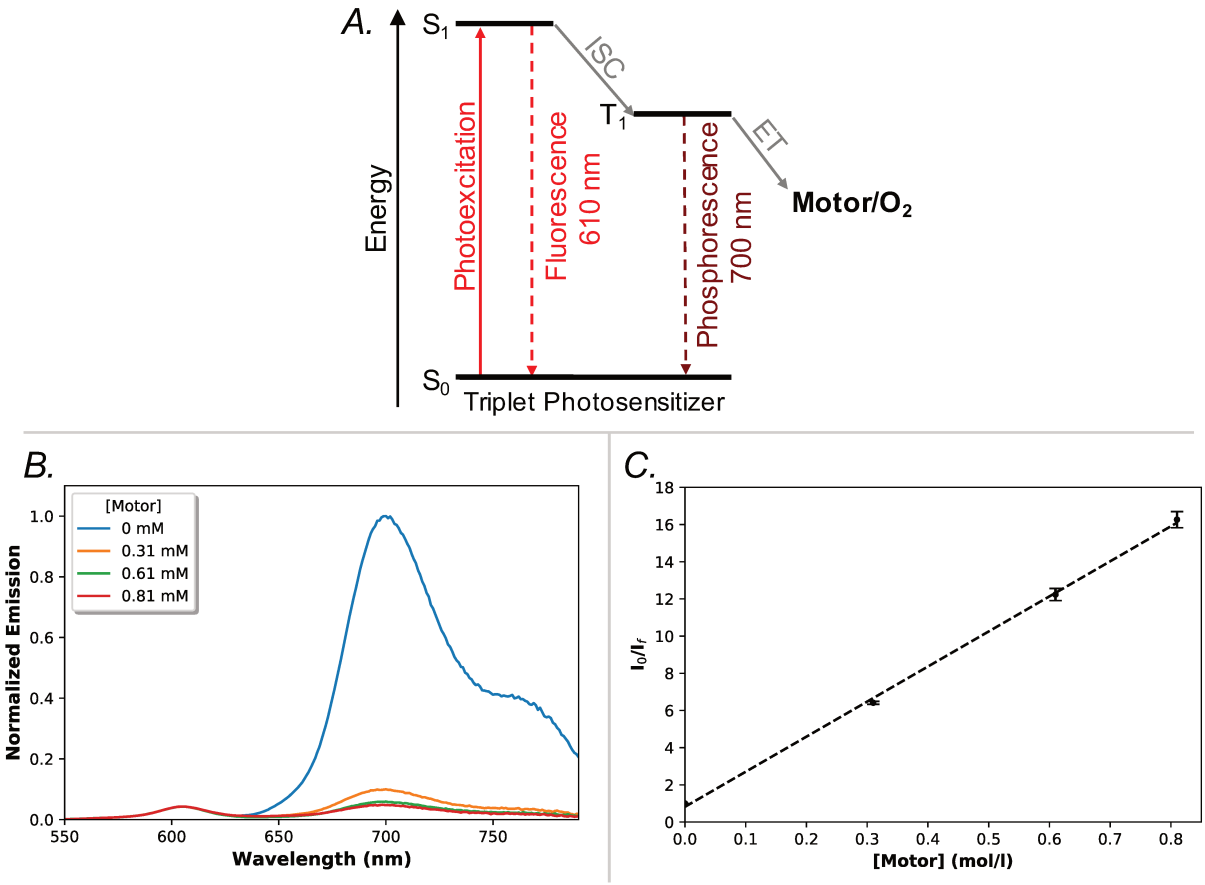

Figure III.4 A. Energy diagram of Pd-TPP. After photoexcitation, the system can return to the ground state either by fluorescence at 610 nm, by phosphorescence at 700 nm or by quenching interaction with another molecule (Motor, O_2, ...). **B.** Normalized phosphorescence emission spectra of Pd-TPP (0.5 mM in $CHCl_3$) with increasing concentrations of motor **13** (λ_{exc} = 532 nm). **C.** Stern-Volmer plot of Pd-TPP (0.5 mM in $CHCl_3$) with increasing concentrations of motor **13**.

To explain the lower efficiency of the triplet energy-transfer process and to explore the possibility to design a more efficient system, we turned our attention to quantum mechanics

calculations, specifically DFT and TD-DFT. The calculations were carried out by a member of our team, Dr. Andreas Vargas Jentzsch. First the molecular geometries of both the molecular motor reported by Feringa[9] and a truncated version of motor **13** (bearing methoxy groups instead of the *tert*-butyldimethylsilyl) were optimized, both on the ground and the triplet excited states using the B3LYP functional[125] and the def2-TZVP basis set[126] and chlorobenzene as implicit solvent. We decided to focus on the triplet-state geometries because considering the lifetime of the triplet states it is likely that the system has enough time to relax to its triplet state geometry and thus it would be the best approximation. Using these geometries, the excited state electronic transitions were calculated by TD-DFT (cam-B3LYP/def2-TZVP). The lowest triplet excited-state energy level was estimated to be at 241 kJ.mol^{-1} (496 nm) for motor **13** and at 193 kJ.mol^{-1} (619 nm) for Feringa's motor. Both these values are higher than the triplet state energy of the Pd-TTP sensitizer, which was estimated at 178 kJ.mol^{-1} (672 nm).[121] As the triplet state energy level of motor **13** is significantly higher, the increased difference in energy can explain the lower efficiency.

For consistency and because, strictly speaking, an energy transfer should not be possible from a lower to a higher energy level, we decided to also calculate the theoretical values of the triplet state energies of the Pd-TTP despite TD-DFT calculations being prone to errors on heavy metals.[127] The lowest triplet excited-state energy level of the porphyrin was estimated at an absurdly low 54 kJ.mol^{-1} (2196 nm). However, when considering only the transitions having a non-zero oscillating strength, three transitions stand out: 157 kJ.mol^{-1} (762 nm), 181 kJ.mol^{-1} (660 nm), and 227 kJ.mol^{-1} (526 nm). The two first ones are remarkably close to the experimentally observed bands of phosphorescence and could be interpreted as a validation of the theoretical result. The third value is not observed experimentally but could, in theory, be populated by irradiation with visible light. If the energy transfer occurs from this state, it would explain the high efficiency of the Feringa system, and the fact that we definitely observe a triplet-state energy transfer, albeit with a lower efficiency, in the results presented here.

III.2.3. Visible light-fuelled gel contraction

With the interaction between Pd-TPP and tetra-functionalized molecular motor **13** in solution now characterized, its influence on a contractile gel can finally be addressed. The design of the system is inspired by what has already been reported by our team.[6,7] A motor unit was functionalised by four triethylene glycol chains with terminal azide, which were made from triethylene glycol (TEG) (**Scheme III.4**). To functionalise the stator, a tosylation reaction was carried out to obtain the product **19**. After adding sodium azide compound **20** was formed and was tosylated once more into chain **21**. This molecule was then coupled with the phenols of motor **14** via nucleophilic substitution reaction to yield the bis-azide motor **22**.

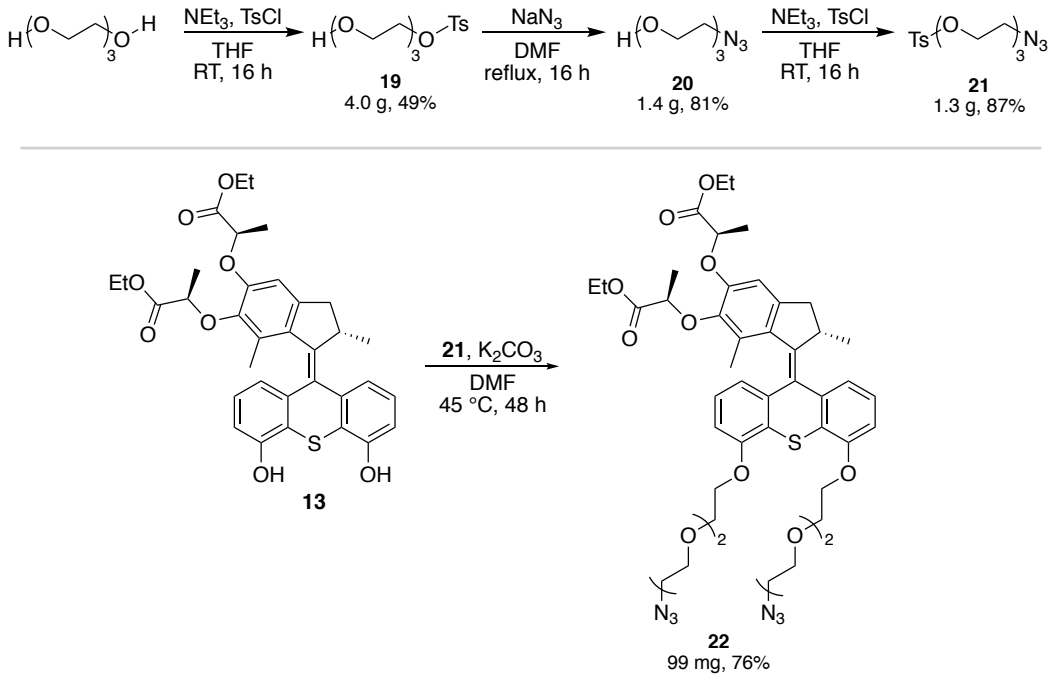

Scheme III.4 Synthesis of tosyl-azide TEG linker **21** and of bis-azide motor **22**.

The functionalization of the rotor required the presence of an amine group on the TEG chain (**Scheme III.5**). To do so, bis-tosyl **23** was obtained by adding an excess of tosyl chloride and then substituted twice with sodium azide to form bis-azide **24**. Addition of one equivalent of triphenylphosphine allowed to reduce one of the azides, giving access to azide-amine TEG **25**. Finally, after deprotection of motor **22** into bis-carboxylic acid **26** by adding sodium hydroxide, amidation reaction in presence of EDC and HOBt yielded tetra-azide motor **27**. The latter was then integrated as reticulating points and linked together with 5600-polyethylene glycol polymer chains bearing terminal alkyne moieties through Huisgen azide-alkyne cycloaddition.

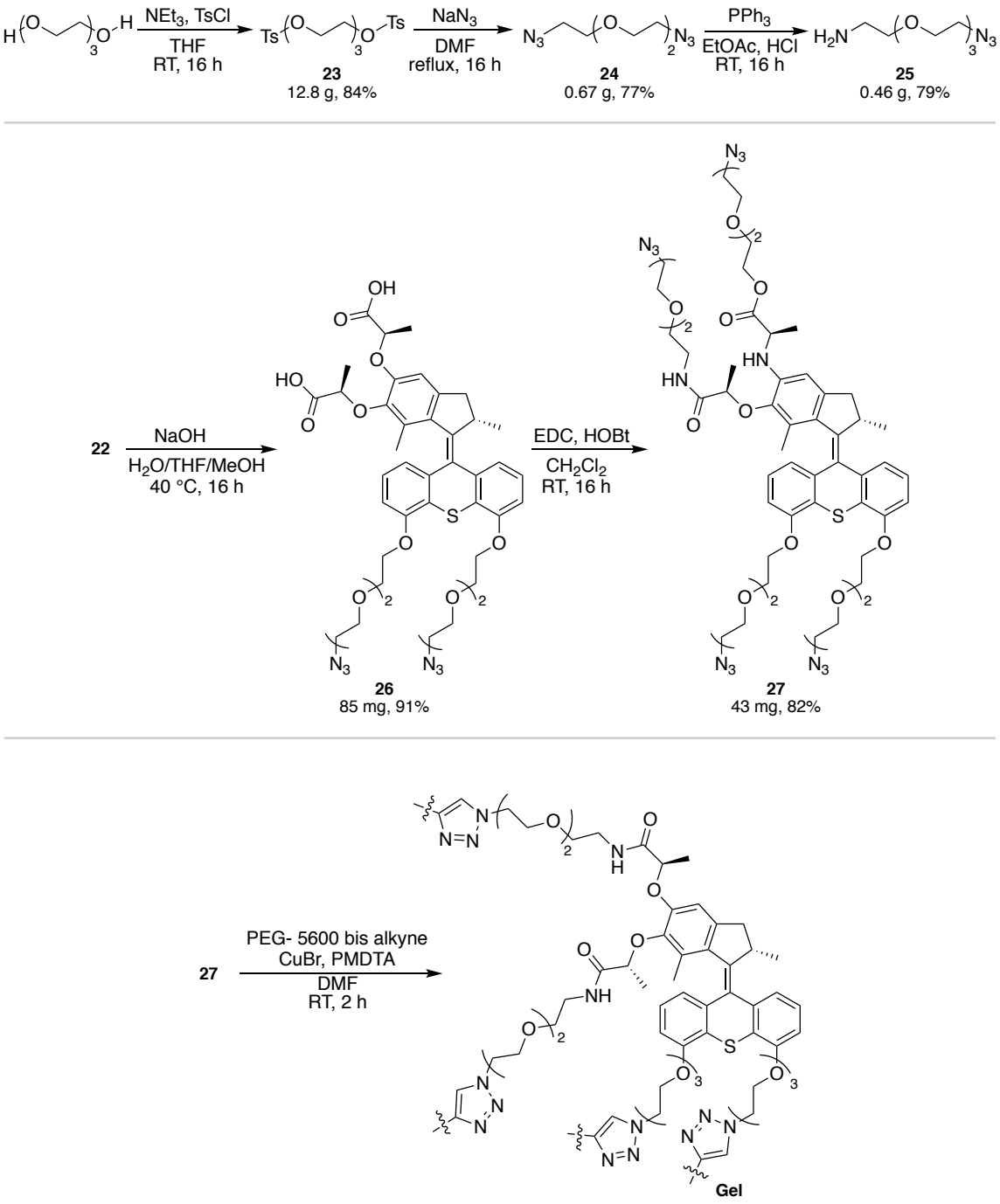

Scheme III.5 Synthesis of amine-azide TEG **25** and of tetra-azide motor **27** and formation of a gel by Huisgen-azide-alkyne click reaction.

The standard preparation process consists in swelling the contractile material in a Pd-TPP solution for at least one day, allowing the porphyrin to penetrate into the gel network. 1,2,4-trichlorobenzene was chosen as solvent since it is characterized by a good porphyrin solubility ($[Pd\text{-}TPP]_{max}$ = 0.2 g/L), low toxicity and high boiling point, thereby limiting its evaporation over time. Argon is bubbled for 30 min in order to limit the presence of oxygen. The film is then inserted inside a circular quartz cell with a 1 mm spacer. A LED is used to irradiate the set-up at 530 nm, by the mean of an optical fiber, and the contraction is recorded with a USB

camera, by taking a snapshot every 10 minutes (**Figure III.5**). Images are then processed to calculate the volume of the system from the area of the photographed surface. It is thus possible to establish contraction curves as a function of time.

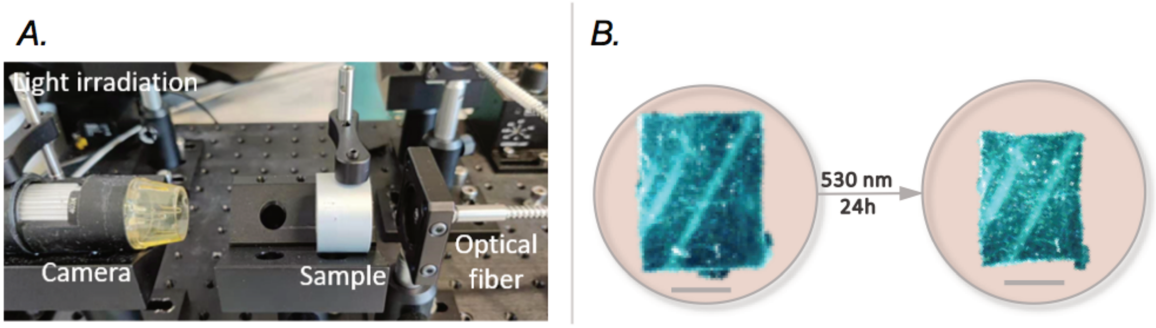

Figure III.5 A. Photograph of the irradiation set-up. **B.** Snapshots of gel before and after 24 hours irradiation at 530 nm. The gel is colourless but the pictures were taken while irradiating. Scale bar, 5 mm.

The gel contraction profiles were recorded at different Pd-TPP concentrations (**Figure III.6A**). Reduction in the overall contraction time as well as in the contraction onset time were observed as the photosensitizer concentration increases. Similarly, the maximum rate of contraction increased with higher porphyrin content. Finally, a relaxation of the material was also noticeable after a certain irradiation time. Although only observable in this graph for a Pd-TPP concentration of 0.2 g/L, this phenomenon occurred systematically over the whole concentration range but at lower rates. We therefore measured the influence of the photosensitizer according to the contraction onset time and the half-contraction time (**Figure III.6B**). The contraction onset time corresponds to the lag time needed for the polymer chains to twist sufficiently before creating a tension in the network. The time of half-contraction corresponds to the time at which 50% of the maximum contraction is achieved. Interestingly, these two parameters are similarly correlated to the porphyrin concentration. The more concentration of Pd-TPP is, the higher the chance of interaction with a motor is, so the faster the contraction and the shorter the delay are.

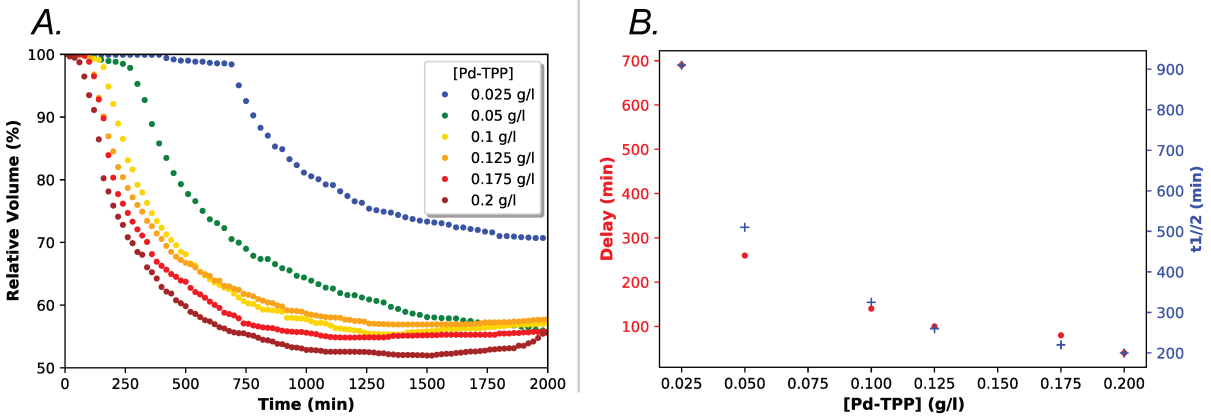

Figure III.6 A. Gel contraction profiles at different Pd-TPP concentrations (in 1,2,4-trichlorobenzene, λ_{exc} = 530 nm, P = 32 mW.cm^{-2}). **B.** Evolution of the **contraction onset time** and the **half-contraction time** $t_{1/2}$ as a function of porphyrin concentration.

The evolution is not linear and shows limits at both low and high porphyrin concentration. Obviously: without photosensitizer, there is no contraction. However, for high Pd-TPP concentration a threshold effect occurs when the vicinity of the motor unit becomes overcrowded, therefore additional Pd-TPP will no longer reduce the contraction time. Overall, for an irradiation of P_{530} = 28.2 mW.cm^{-2} a maximum shrinkage of 48% was obtained in about 16 h for a 0.2 g/L concentration of photosensitizer.

At the end of the contraction, gel relaxation was observed. This phenomenon has already been reported by our group[6] and it could be caused by the oxidation of the central double bond of the motors whose reactivity is enhanced by the increased tension. A free rotary axe is then formed, allowing the unwinding of the polymer chains and leading the gel to eventually swell back. Furthermore, as mentioned earlier, under UV light irradiation, solubilisation of the material could also be observed, indicating degradation of the network through excitation of organic molecules and/or formation of radical species. Thus, in 1,2,4-trichlorobenzene, no contraction could be measured under UV due to the rapid solubilisation of the gel, whereas at 530 nm such process did not occur even after 5 days of constant irradiation.

In addition, we still observe some difference in the measured contraction rate of gels with similar structures between visible (P_{530} = 28.2 mW.cm^{-2}, 48%, 16h, 1,2,4-trichlorobenzene) and UV light irradiation (P_{UV} = 70 mW.cm^{-2}, 45%, 120 min, toluene). At first glance, we thought that it comes from the difference in light intensity. However, studying the influence of the irradiation power on the contraction rate showed that the latter reaches a plateau at P_{lim} = 60 mW.cm^{-2}, suggesting that a kinetic limiting process is taking place (**Figure III.7**). At first sight, one might think that the thermal helix inversion is the rate limiting step. Indeed, the group of Feringa has shown that the presence of bulky groups can slow down the rate of rotation by increasing the energy required for this thermal relaxation.[10] Such a phenomenon most certainly also occurs in our system with the presence of long polymer chains integrated in a network. This would mean that all the motors are in their unstable form and therefore out of equilibrium. Similar kinetics should be observed under UV light irradiation. Thus, we deduced that the limitation is not related to the intrinsic functioning of the motor but rather to the rate of the intermolecular energy transfer. Although effective in solution, it is conceivable that this transfer is more difficult to achieve within a polymer network, since it requires close proximity between the photosensitizer and the crowded alkene. Therefore, at high light intensity, despite the excitation of most porphyrins, the time required to approach a motor remains the same, which would explain the presence of this plateau.

Regarding the difference in the contraction maxima, we noticed that the nature of the solvent and the gelation process have an important influence on the topology of the polymer, resulting in the presence of heterogeneities which may reduce the ability of the gel to contract. These factors and their corresponding impact are currently under study.

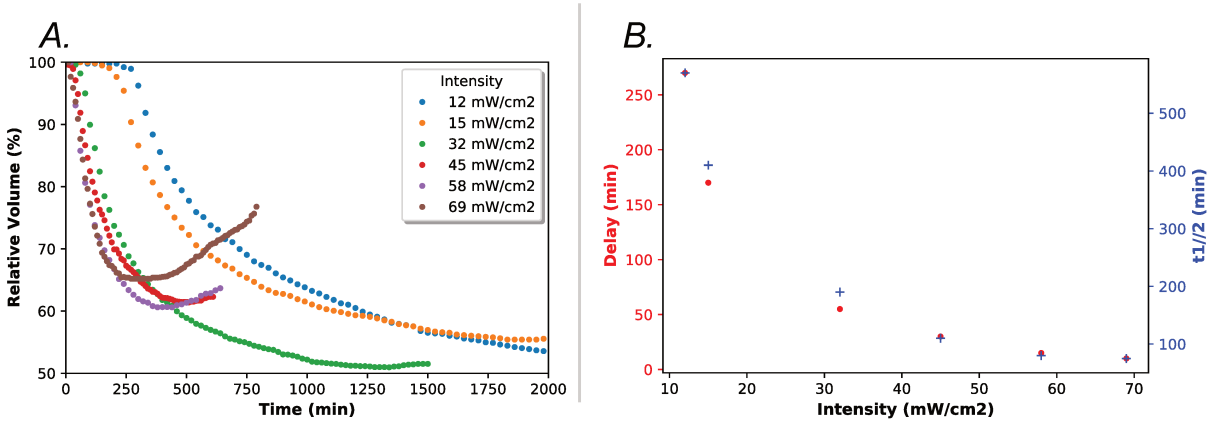

Figure III.7 A. Gel contraction profiles for different irradiation intensities (in 1,2,4-trichlorobenzene, [PdTPP] = 0.2 g.L^{-1}, λ_{exc} = 530 nm). **B.** Evolution of the **contraction onset time** and the **half-contraction time $t_{1/2}$** as a function of visible light intensity.

III.3. Conclusion

The addition of a porphyrin-based photosensitizer allows the unidirectional molecular motors to rotate when fuelled with visible light at 530 nm via a triplet state energy transfer mechanism. Its integration into a chemical gel containing molecular motors as reticulation points, allows the contraction of the material under visible light irradiation. The shrinking rate strongly depends on the porphyrin concentration and the light intensity, which are directly related to the energy transfer rate. Thus, the best contraction takes place with Pd-TPP saturation, over a period of about an hour and at a rate similar to what has been measured with UV irradiation, without showing any signs of degradation usually caused by light at these wavelengths.

The next challenge consists in improving the efficiency of the energy transfer to eventually accelerate the contraction process. The approach currently being investigated is to covalently integrate the photosensitizer into the gel in order to impose proximity between the porphyrin and the motor. Another strategy involves modifying the photosensitizer structure to better match the energy levels of the motor.

Chapter IV. Light-Fuelled Propulsion of JNPs

IV.1. Introduction

Nanorobotics is a rapidly growing field that follows perfectly the bottom-up approach proposed by R. P. Feynman. It mainly consists in assembling nanoscopic units into a larger structure to perform novel functions. Nano-robots or "nanobots" are particularly well suited for the development of precision medicine.[128–130] They offer an alternative to invasive surgery by treating a given problem from the inside,[131] enable targeted drug delivery[132] and can perform diagnostics[133] as well as imaging.[134] They have even found some use in water treatment and purification.[135]

However, due to their size, these systems operate in environments governed by low Reynolds numbers, meaning that they are strongly subject to Brownian motion as well as to the viscosity effect of the surrounding medium, causing their inertia to be negligible. Therefore, one of the most important challenges in the development of this type of nanosystems is the control of their locomotion. To this end, various strategies have been developed. The first one consists in applying an external force, such as electric,[136] optical[137] or rotating magnetic fields,[138,139] as well as ultra-sound[132,140] to move the nanobot directly. Externally fuelled devices are obviously very practical as they generally do not produce waste and are applicable to biological systems. However, the nature of the interactions employed intrinsically limits the minimum scale of the nanobot. Indeed, in the case of external rotating magnetic fields, sub-micrometric structures have a rapidly increasing erratic motion and require increasing frequencies, with a dependence inversely equal to the cube of their size.[141]

In contrast, the second approach is based on the self-propulsion of the nanobots by an on-board machine allowing each unit to move autonomously and independently, even at small scale. In this context, systems based on the formation of microbubbles at their surface have been developed. By consuming fuel present in solution, the structure is propelled forward by a stop-and-go movement and can reach speeds up to a few millimetres per second (**Figure IV.*1*A**).[142]

Nature offers us a magnificent alternative with the movement of micro-organisms such as flagella or cilia generated by chemical motors which sets their appendages in motion.[143] The use of a helical structure allows corkscrew-like travel and has led to the design of a large number of artificial propellers.[11] The majority of these devices works thanks to the rotation of one or more helices fixed on a common core. Janus nanoparticles (JNPs) are particularly well suited to serve as a building platform. They are colloidal objects that are characterised by their anisotropy in shape as well as in surface chemistry. Since they were first conceptualised in 1991 by P. G. de Gennes,[144] they have attracted a great interest and their development has been rapid.[145] Acting as a strong surfactant[146] or as a building block for the elaboration of supramolecular structures,[147] they are now found in numerous applications, ranging from

drug delivery[148] to theranostics[149] and textile materials.[150] Their potential in the preparation of nanobots is such that today the vast majority of systems are based on them, like the bubble propellers described above (**Figure IV.1A**).

In autonomous devices, movement is often achieved through chemical reactions. In biological organisms, motion is mainly powered by the hydrolysis of ATP or by ion-pumps, but in artificial JNPs bubble systems redox processes are used and most of them require the presence of hydrogen peroxide.[151] Furthermore, even when water alone is consumed,[152] the generation of waste either in the form of bubbles or by-products remains an issue, especially for medical applications.

In contrast, light represents an interesting alternative, depending on the wavelength, it can easily penetrate biological tissues without harming them while remaining spatiotemporally selective. However few examples involving autonomous light-fuelled nanobots have been reported so far. One remarkable example has been developed by Fischer *et al.* and consists in the peristaltic motion of a liquid-crystal elastomer structure (**Figure IV.1B**).[153] The presence of azobenzene in the network allows, under visible light irradiation (532 nm) and at relatively low quantities (*i.e.* 1%mol), the transition from a nematic phase to a disorganised isotropic state, through its *trans-cis* isomerisation, thus generating a local expansion of the material. Conversely, when placed in the dark, this photoswitch spontaneously returns to its original configuration, allowing the material to recover its initial properties. Digital micromirror device allows the system to be irradiated with great precision and to control the position and displacement of the expanding zones, resulting in a worm-like motion.

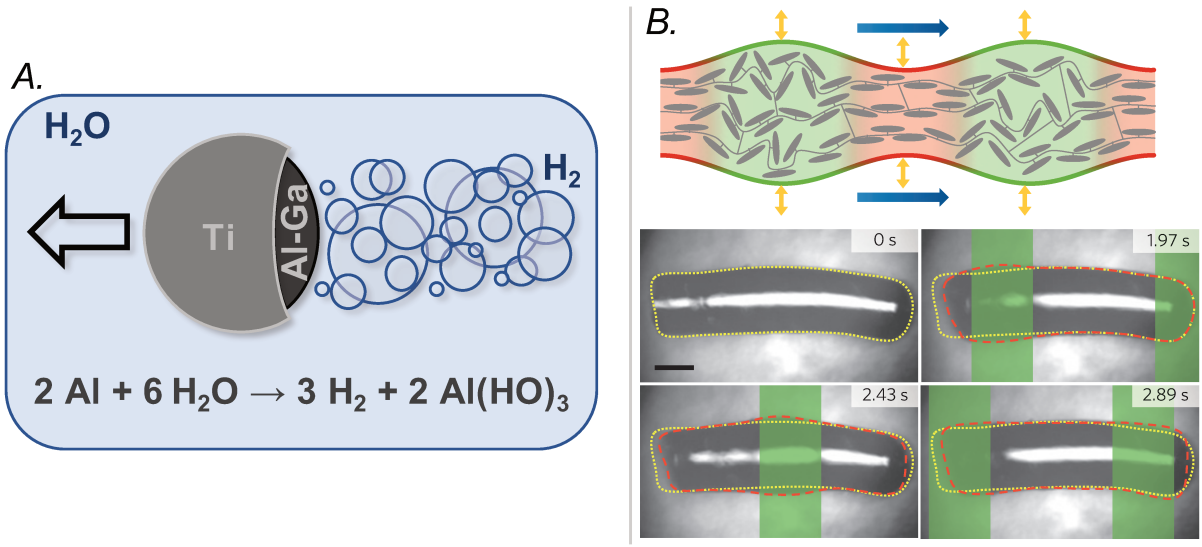

Figure IV.1 A. Scheme depicting a propulsion of the water-fuelled Ti/Al-Ga based asymmetric micro-motor by formation of dihydrogen resulting from the oxidation of aluminium and reduction of water. Adapted from ref 152. **B.** Scheme illustrating the selective disorder induced by isomerisation of azobenzene-based LCE under light irradiation (532 nm). The corresponding snapshots depict how the relaxation of the material can be translated to a worm-like movement. Scale bar, 200 µm. Adapted from ref 153.

Initially envisaged by Feringa,[10] the only example that has been reported to date incorporating a light-responsive motor is limited to propelling structures at the molecular scale.[154] In this work, J. M. Tour *et al.* developed a molecular motor that moves in solution while two fluorophores, placed on the stator, allow to monitor its motion by single molecule fluorescence correlation spectroscopy (**Figure IV.2**). A comparative study showed significant increase (up to 26%) in the diffusion rate of systems involving fast molecular motors (MHz) as long as they were placed under UV irradiation. In the case of fast non-directional motors, smaller increase of about 10% was observed. Conversely, inert structures (without rotor) or those bearing slow molecular motors (mHz) showed no significant change in their diffusion rate. Interestingly, the viscosity of the solvent does not seem to have a significant impact on the ability of the system to move. Overall, although the mechanism of motion has yet to be elucidated, these results clearly demonstrate the ability of a molecular motor to propel itself in solution.

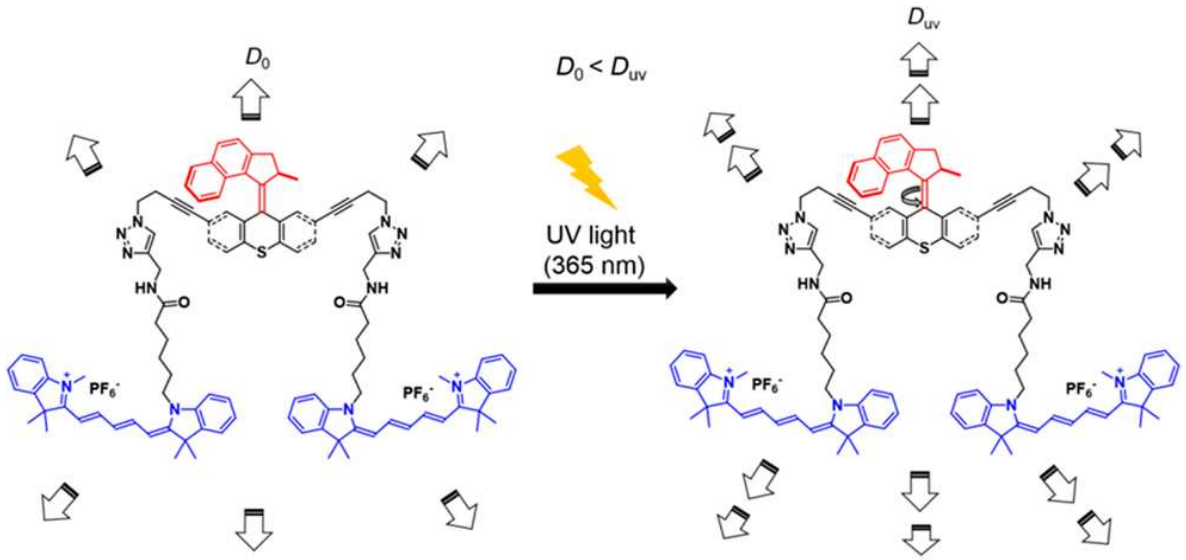

Figure IV.2 Molecular structure of the light-fuelled nanomachine. Upon irradiation an increase of 26% in the diffusion rate is observed. Adapted from ref 154.

Thus, inspired by these results and by the potential of the overcrowded alkene-based molecular motors to move nano-objects on a surface,[103] we investigated the use of these units functionalized by helixes to induce the propulsion of Janus nanoparticles under light irradiation. The work presented here results from the collaboration between organic chemists, polymer chemists and physicists. Pr. Christophe Serra and Dr. Madeline Vauthier (ICS, Strasbourg) have been in charge of elaborating the Janus particles. Our team focused on the synthesis of molecular motors and the study of their attachment to the nano-objects. Finally, Pr. Eric Buhler (LMSC, Paris) studied their characterisation by dynamic light scattering to determine whether a ballistic motion is indeed produced.

IV.2. Results and discussion

IV.2.1. System design

We initially attempted to synthesize clickable particles according to literature procedure,[155] which consisted in the preparation of linear polystyrene as a seed for the emulsion polymerisation of Janus particles functionalised with propargyl acrylate. However, the protocol used required the presence of 2,2'-azobis(2,4-dimethylvaleronitrile) (V-65B, Wako), a free radical initiator not readily available in Europe. All the attempt to replace it failed and we initiated a collaboration with the group of Serra of the ICS. Indeed, this team has recently developed a one-step method to prepare Janus nanoparticles from polystyrene sulphonate (PSS) and poly(lactic-co-glycolic acid) (PLGA) by elongational-flow micromixing (**Figure IV.3**).[156] More precisely, an aqueous solution containing Pluronic® F-127 as surfactant is mixed with an ethyl acetate solution in which the two polymers are solubilised. A double pump system allows the formation of an emulsion by means of a back and forth movement through microchannels. The number of cycles and the flow rate directly influences the size of the obtained particles. The resulting mixture is finally evaporated to remove traces of organic solvent. The colloids formed range in dimension from about 150 to 230 nm as determined by dynamic light scattering and are relatively monodisperse (*i.e.* PDI = 0.1-0.24). They are stable for about a month in an aqueous solution and are characterised by the presence of a hydrophilic and a hydrophobic side.

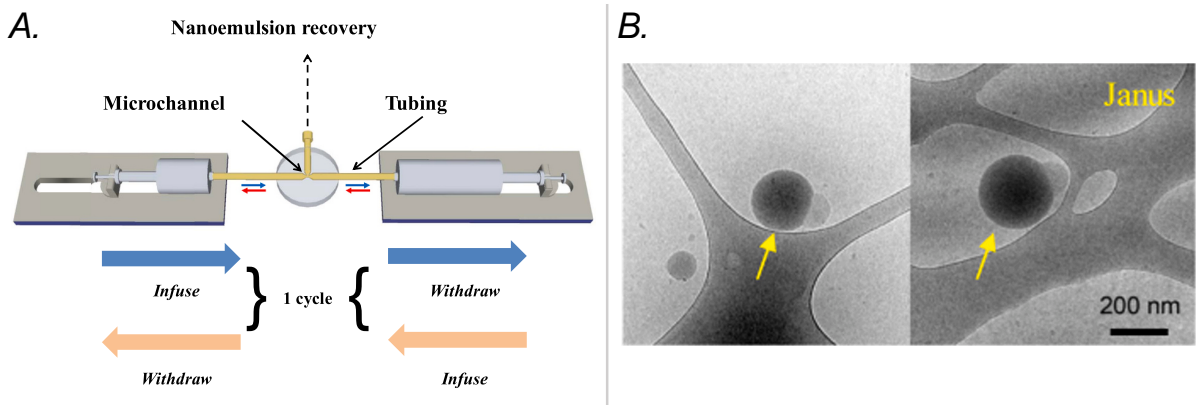

Figure IV.3 A. Scheme depicting the elongational-flow micromixer device. **B.** Cryo-TEM snapshots of the particles resulting from the micromixer (30 mL.min^{-1}, 150 cycles). Adapted from ref 156.

However, these Janus particles are also difficult to functionalise. They are indeed only stable in water and cannot withstand high temperatures, which considerably limits the range of possible coupling reactions with molecular motors, especially as the latter is hydrophobic. Our strategy to functionalized these JNPs consisted in taking advantage of the presence of negative charges on the PSS side to anchor molecular motors by electrostatic interactions. We thus designed molecular motor **29** which presents two permanent ammonium groups on the stator. Starting from the bis-phenol motor **14** and by simple addition of dibromoethane in

DMF at 60°C, bis-bromo intermediate **28** was obtained in relatively low yield due to a difficult purification by chromatographic column (**Scheme IV.1**). Subsequently, the addition of trimethylamine solubilised in ethanol allowed the formation of bis-ammonium motor **29** characterised by the presence of two permanent positive charges. As both reagents and solvents are volatile, isolation of the desired product occurred by simple evaporation under reduced pressure and proceeded in an almost quantitative yield. Such a motor is water soluble,[157] but it remains necessary to verify its ability to bind to the JNPs via the formation of ionic bonds with the sulphonate moieties. To this end, cation **29** was solubilised in deionised water and added to a solution of JNPs, before characterization.

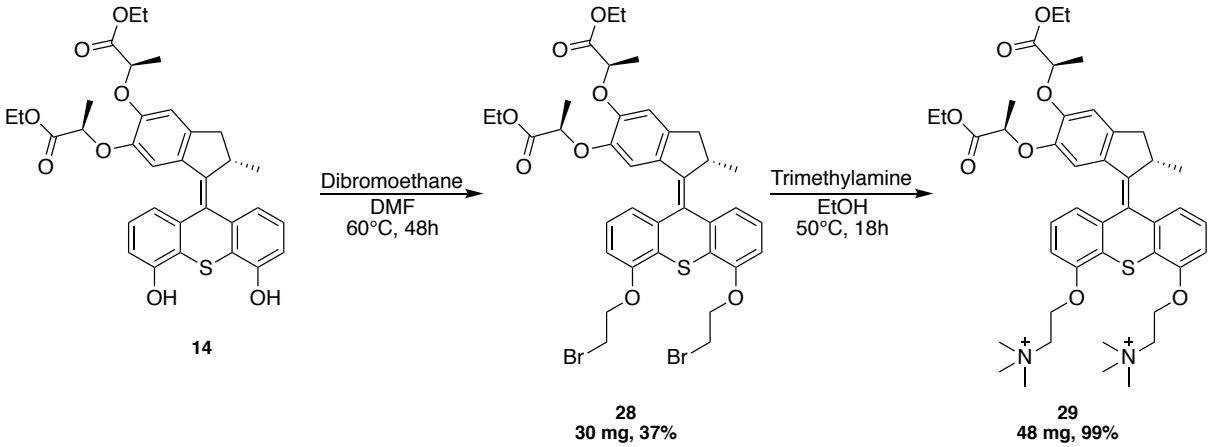

Scheme IV.1 Synthesis of the bis-ammonium Motor **29** by nucleophilic substitution on the bis-bromo Motor **28** intermediate.

IV.2.2. Janus particles functionalisation

A. Dynamic light scattering

Janus particles prepared by the team of Prof. Serra and Dr. Vauthier have a diameter of ~100 nm and are in general dispersed in water at a concentration of 2 g/L. Our first objective was to ensure that our molecular motor is able to bind them. Different procedures have been used for that. The first one consisted in measuring the size of the particles before and after the addition of molecular motor **29** by dynamic light scattering (DLS) (**Figure IV.4**). Unfortunately, due to the very small difference in size between the two systems, we did not observe any change beyond the measurement error. It is therefore impossible at this stage to draw any conclusions.

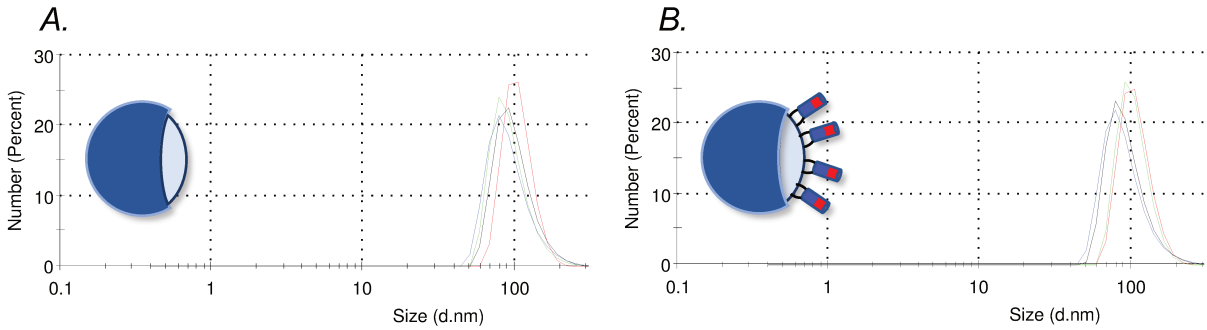

Figure IV.4. Dynamic Light Scattering measurement with a size distribution by number of a solution **A.** JNPs (0.2 g/l) and **B.** JNPs (0.2 g/l) + Motor **29** (0.2 g/l).

B. Zeta potential

As an alternative, we chose to take advantage of the presence of charges on the surface of the JNPs to monitor the evolution of the Zeta potential over the quantity of motor. The Zeta potential corresponds to the difference in electrical potential between the surface and the neutrality point and can be deduced from the electrophoretic mobility of the particles. Since PSS is anionic, we expected that the progressive addition of bulky cationic molecular motors will lead to a diminution of the mobility and an increase in the apparent charge. This was indeed observed experimentally (**Figure IV.5**). In practice, measurements were carried out on a range of samples containing always the same concentration of JNPs (*i.e.* 0.2 g/L), to which a motor solution (at 0.1 g/L) was added in variable quantities.

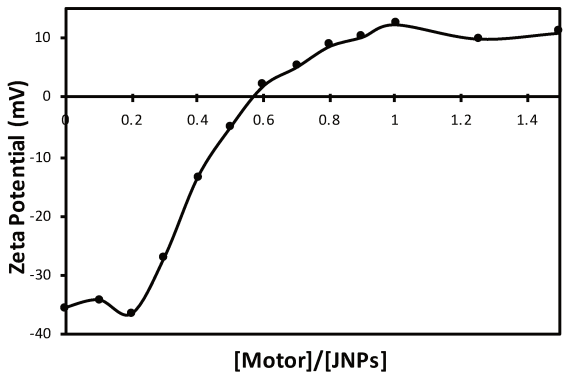

Figure IV.5. Evolution of the Zeta potential for different Janus particles - Motor ratio. The x-axis corresponds to the ratio of the mass concentration of the motor to that of the particles, as the molar mass of the nanoparticles has yet to be determined.

Initially, for pure JNPs, the measured potential is low, at around -35 mV, in agreement with the presence of negatively charged moieties. For concentration ratios below 0.2, we observed the presence of a plateau, which might be related to the filling of the surface layer by motors, which has little influence on the sliding plane and therefore on the value of the potential. Then, for concentration ratios between 0.2 and 1, a rapid increase in potential is observed, most likely corresponding to the progressive filling of the ionic double layer, which has the

greatest influence on electromobility. Finally, for concentration ratios above 1, a second plateau is distinguished, which attests to the saturation of the second layer. Interestingly, we also observed an inversion of the apparent charge of the nanoparticles. This phenomenon is not fully understood, although it is obviously linked to the accumulation of motors around the Janus particles but it implies that there are more positive than negative charges. Electrostatic forces are not sufficient to produce such a result, so another type of interaction must take place. Since the motor remains a predominantly aromatic system, it is conceivable that hydrophobic interactions between the rotor and the PLGA are responsible for this excess. As these interactions are weaker, they would be less effective in binding the motor and the evolution of the potential would be slowed down, which is illustrated here by a change of slope when the system becomes positively charged. In any case, these results certainly point to the existence of interactions between motors and JNPs.

C. Fluorescence

At the same time, we also noticed that JNPs in the presence of molecular motors were strongly luminescent under UV, whereas a solution of particles alone remained dark. In order to confirm the presence of interactions between motors and JNPs, we carried out a fluorescence study in the absence or presence of JNPs, using the Raman scattering peak as reference for normalisation. At first, we measured the emission spectra of the motor alone in solution over a concentration range from 0.01 g/L to 0.1 g/L (**Figure IV.6A**). The evolution is linear as expected for a chromophore isolated in solution at relatively low concentration (**Figure IV.6B**).

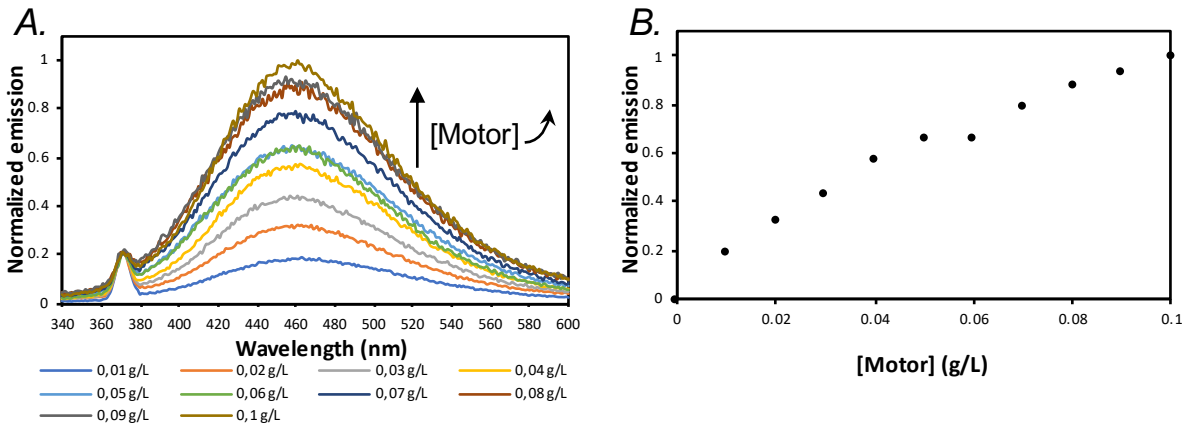

Figure IV.6 A. Fluorescence spectra of the molecular motor in water for different concentrations (λ_{exc} = 330 nm), the peak at 370 nm corresponds to the Raman scattering peak of water. **B.** Evolution of the motor emission as a function of concentration.

However, in the presence of Janus particles at 0.2 g/L, the fluorescence spectrum of the motor over the same concentration range evolved quite differently (**Figure IV.7**). Indeed, for the same setting parameters an increase by a factor 10 in the emission is observed with, this time, the appearance of a plateau starting at concentration ratio of 0.4. This difference in the emission intensity indicates a change in the de-excitation kinetics of the molecular motor. This

type of phenomenon commonly occurs when a fluorophore is immobilised on a surface, as modification of the electronic environment can induce a reduction of the non-radiative processes leading to an increase in fluorescence.[158]

On the other hand, the presence of a plateau for concentration above 0.4 suggests the existence of a fluorescence quenching process. This is certainly linked to the increase in motor concentration on the surface of the particles as the ratio increases. Indeed, as soon as an excited chromophore is at the vicinity of at least another one in the ground state, an energy transfer can take place, limiting the radiative processes. Overall, this fluorescence study strongly indicates that the motor is indeed attached to the surface of the nanoparticles.

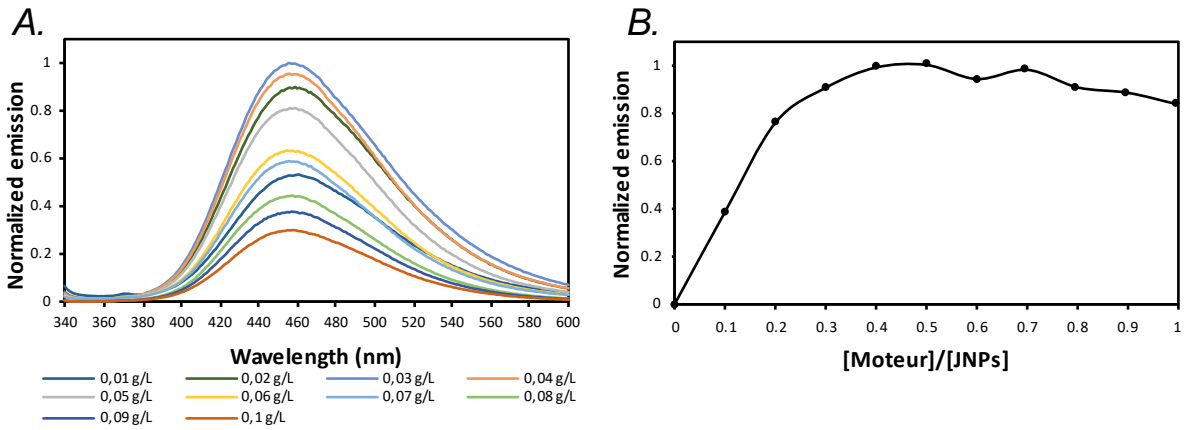

Figure IV.7 A. Fluorescence spectra of the molecular motor at different concentrations in water in the presence of JNPs (0.2 g/L) (λ_{exc} = 330 nm) **B.** Evolution of the motor + JNPs emission as a function of concentration ratio.

D. Cryogenic-transmission electron microscopy

Transmission electron microscopy (TEM) can also provide insights on whether there is an interaction or not between JNPs and molecular motors. In the case of this PSS/PLGA-based JNPs, Prof. Serra and Dr. Vauthier noted that only cryo-TEM could clearly distinguish their anisotropy. Thus, in the absence of a motor, objects consisting of two distinct parts could be observed (**Figure IV.8A**), the contrast being linked to the difference in electron density of the constituent polymers.

As shown on **Figure IV.8B**, the addition of molecular motors resulted in the formation of homogeneous nanoparticles for a [Motor]/[JNPs] ratio of 1. With such a quantity of motor, Zeta potential measurements as well as fluorescence experiments indicated that the surface of the particles is completely saturated to the point where the apparent charge even become positive. The presence of motors may result in homogenisation of the surface electron density, resulting in the appearance of symmetrical nano-objects.

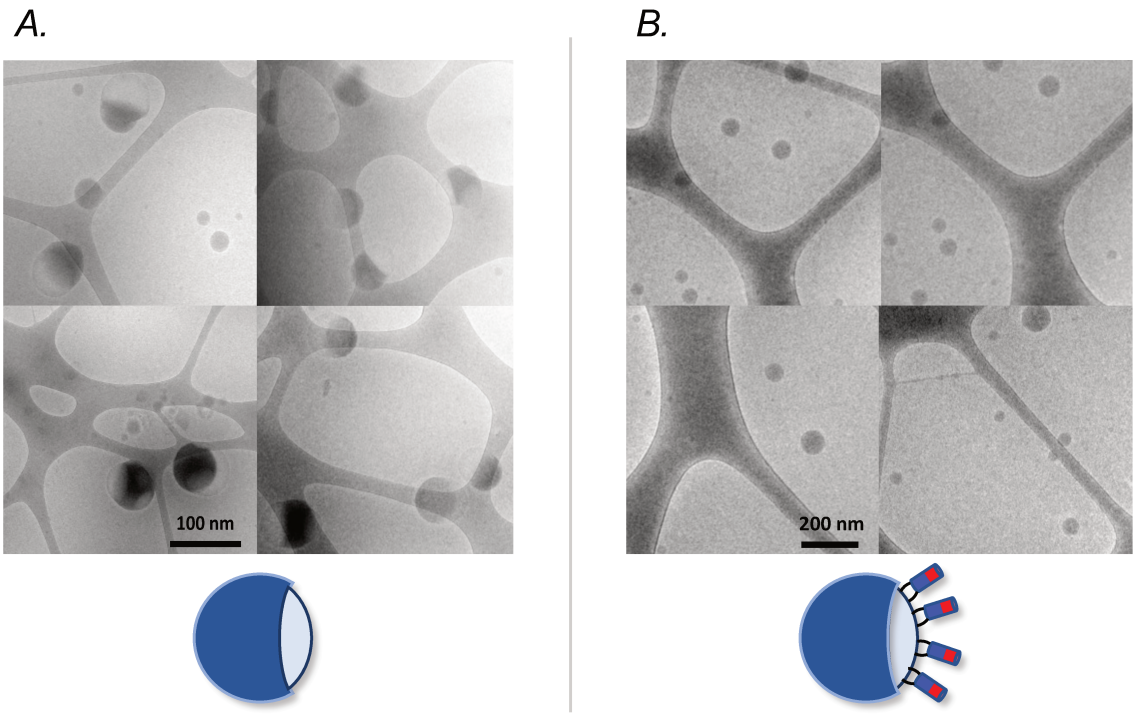

Figure IV.8. Cryo-TEM pictures of Janus nanoparticles at 0.2 g/L without **a.** and with **b.** motors for a ratio [Motor]/[JNPs] ratio of 1 .

Overall, electron microscopy, zeta potential measurement and fluorescence experiments together suggest the presence of molecular motors on the surface of Janus nanoparticles. Although powerful, these techniques do not allow us to attest their propulsion under UV irradiation. Such measurements require to use advanced scattering-based characterisation methods, which were performed by Prof. Eric Buhler (LMSC, Paris).

IV.2.3. JNPs propulsion

Rayleigh scattering characterizes the elastic emission of light, *i.e.* without energy loss, by particles much smaller than the incident wavelength. This very common phenomenon is central for experimental techniques aiming at characterising nano-objects. In this context, static light scattering consists in the measurement of the scattered intensity (I) of dispersed particles in solution as a function of the measurement angle (θ), which can also be represented in the form of a scattering wave vector (q).

$$q = \frac{4\pi sin\theta}{\lambda} \qquad (\text{IV.1})$$

Here, λ corresponds to the wavelength of incident light. This is a powerful technique since it allows the determination of physical properties such as the apparent average radius of gyration (R_G), corresponding to the root of the mean square of the distance between centre of mass and monomers, or the average molar mass (M_W) of the particles by extrapolation of I at $q^2 = 0$, if we have access to the dn/dc values.[159] In our case, this measurement was

performed on three different samples consisting of JNPs alone, JNPs in the presence of motors and finally JNPs with motors while irradiating in-situ with a UV LED (**Figure IV.9A**). The curves obtained are relatively similar and all three follow the shape of a decreasing exponential, characteristic of a Guinier regime. (**Figure IV.9B**).

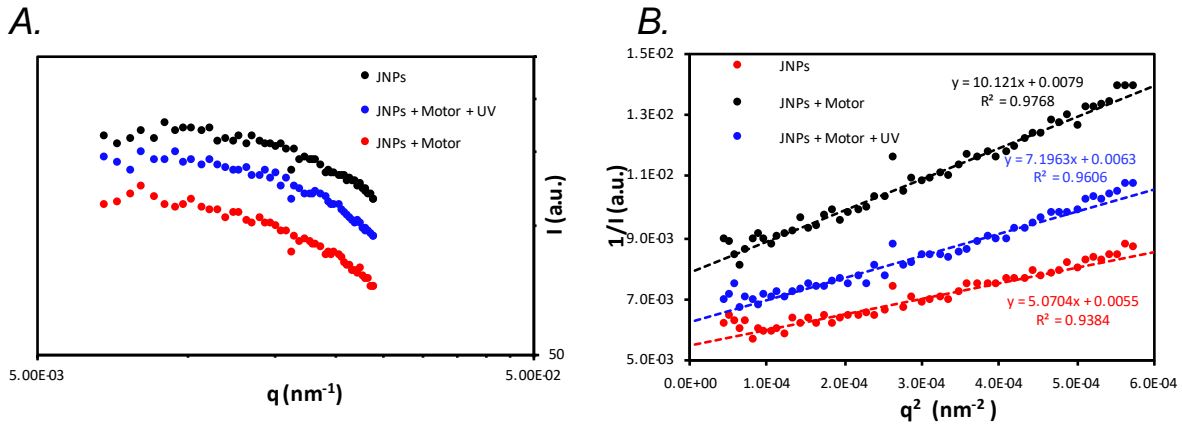

Figure IV.9. A. Static light scattering (SLS) measurement of JNPs (0.2 g/L) with or without motor (0.1 g/L) either in the presence or absence of UV irradiation. **B.** Guinier plot of the SLS measurements and corresponding linear regression.

Guinier plot of the SLS data enable determination of apparent R_G according to Guinier model:

$$\frac{1}{I(q)} = \frac{1}{I(q^2 = 0)}\left(1 + \frac{q^2 R_G^2}{3}\right) \qquad (\text{IV.2})$$

Linear regression of the experimental date afforded the following values, by neglecting the Virial effect (*i.e.* interactions between each object):

$R_G^{(\text{JNPs})}$ = 52.5 nm

$R_G^{(\text{JNPs + Mot})}$ = 62 nm

$R_G^{(\text{JNPs + Mot + UV})}$ = 58.4 nm

A small increase of the radius of gyration was observed after addition of molecular motors **29** and a relative decrease was spotted when the system is placed under UV irradiation. This increase in size is consistent with the addition of the motor to the surface of the particles.
Subsequently, homodyne dynamic scattering experiments were carried out. This technique gives access to the polydispersity (PDI) of the sample and showed a single diffusive (*i.e.* Brownian) process with or without UV along with a characteristic time inversely proportioned to q^2 allowing the determination of the apparent hydrodynamic diameter (D_H) of the particles. The latter is related to the apparent hydrodynamic radius (R_H), which corresponds to the size of a spherical particle diffusing at the same speed, via the Stockes-Einstein relation if the temperature and solvent viscosity are known. R_H can therefore also provide information on the geometry of the objects using the ratio:

$$\rho = \frac{D_H}{2R_G} \qquad (\text{IV.3})$$

The following values were measured at a fixed concentration and by neglecting the Virial effect:

PDI = 0.11	$D_H^{(JNPs)}$ = 138 nm	ρ = 1.31
PDI = 0.19	$D_H^{(JNPs + Motor)}$ = 132 nm	ρ = 1.06
PDI = 0.19	$D_H^{(JNPs + Motor + UV)}$ = 132 nm	ρ = 1.13

We can immediately notice that the polydispersity of pure JNPs is quite good, with a value of 0.11. This value decreases slightly with the addition of motors, which could possibly be linked to an inhomogeneous distribution of the cations among the particles. Concerning the hydrodynamic diameter, we can observe that the addition of motors decreases the apparent size, which goes from 138 nm to 132 nm. This phenomenon is not completely understood, but may be caused by an electrostatic screening effect of the particles by the motors.
Moreover, the ρ ratio indicates that these nano-objects are initially endowed with a geometry close to the hard sphere ($\rho_{(hard\ sphere)}$ = 1.29), but it subsequently decreased with the addition of motors. As the latter are not uniformly distributed on the surface, this lower ρ ratio might be explained by the fact that the particles may experience a small deformation of their apparent structure.
Finally, we observe that the hydrodynamic diameter remains identical in the presence or the absence of UV irradiation. Such a result is quite normal in the case of a homodyne dynamic light scattering experiment, since this technique only allows access to the scattering constant by capturing the scattered light, unlike the so-called heterodyne technique. It consists in adding to the scattered beam a second reference signal derived from the partial deflection of the incident laser (**Figure IV.10**),[160] thus allowing the average drift speed of the particles in solution to be known. To date, ballistic component (*e.g.* a forced diffusion) in the intensity autocorrelation function could be observed allowing determination of complex (in the sense of complex numbers) dynamical structure factor. These preliminary results are thus encouraging and seem to attest the ability of the motors to propel a structure. However, further analysis and calculations are still required before it can be fully validated.

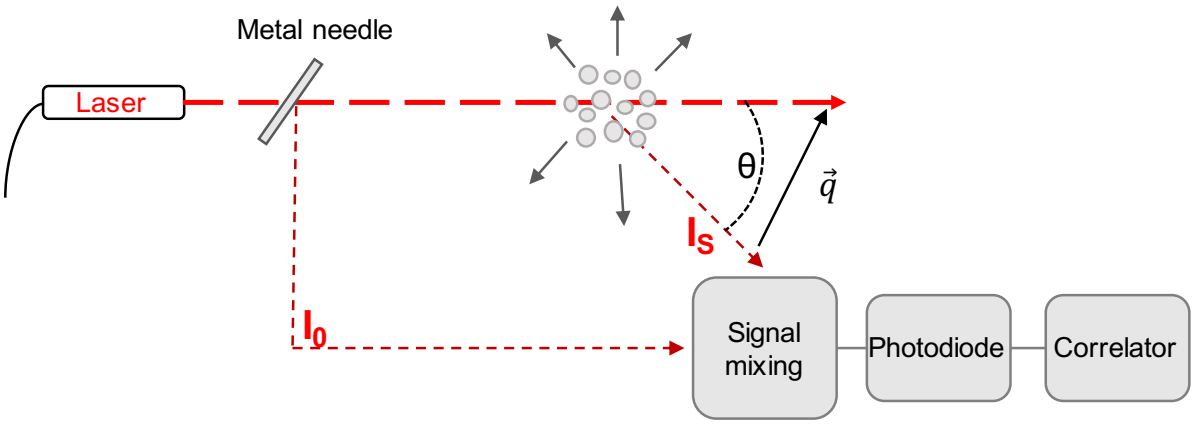

Figure IV.10. Scheme depicting a heterodyne dynamic light scattering set-up where I_0 is the reference beam, I_S the scattered beam, **θ** the scattered angle and **q** the scattering wave vector.

IV.3. Conclusion

Overall, we believe that the work reported in this manuscript makes a definite advance in the field of self-propelled systems, thanks to the fruitful collaboration of chemists, physical chemists and physicists. Indeed, using Janus particles based on PLGA and PSS, we succeeded in functionalizing them with Feringa type molecular motors thanks to electrostatic interactions, as determined by Zeta potential measurements and fluorescence experiments. Finally, dynamic and static light scattering analyses have allowed us to accurately characterise these nano-objects, the latest results of which suggest (but have yet to be confirmed) that they can be propelled.

Nevertheless, in the short term, more analyses are still required to confirm our conclusions. In the medium term, we envision to investigate the interaction between these charged objects by determining the Virial coefficient and to add propellers to the system.

With a size ratio of 1 to 100, motors are very small compared to the dimensions of the particles to be moved. Therefore, in order to amplify the effects of each rotation, we should consider functionalizing the rotor. Indeed, it has been reported that the presence of bulky moieties allows more solvent to be stirred at the cost of an increase in the energy barrier of the thermal relaxation stage.[10] A screw-shaped propeller is a widely used structure for the generation of propulsion, both in micro-organisms[11] and in aeronautics.[161] Such a device follows an asymmetric time-sequence allowing optimal displacement at low Reynolds numbers.[162] We think that a polyproline (n = 15 - 50) is particularly suited as it self-organises into a helix with a pitch of only three units[163] and can be easily obtained via solid-phase peptide synthesis (SPPS). SPPS is a very powerful synthetic technic as it significantly facilitates the purification steps while offering great control over chain length and sequence.[164,165] In addition to being rigid, polyproline is also functionalisable,[166] as each proline can carry secondary groups, which allow modulation of the properties of the structure, such as its hydrophilicity. In the long term, we think that it will be desirable to study the effects of chain length and the nature of its substituents on its propulsion capacity.

To date, polyproline has been successfully synthesised but its attachment to the molecular motor is still under study, we plan to attach it to the motor via a Huisgen click reaction between two azide-functionalised proline units and alkynes groups placed on the rotor, as illustrated on **Figure IV.11**.

Finally we also plan to study the influence of different parameters, such as the length and structure of the helices or the quantity of motor at the surface of the particles, on the propulsion speed of the system.

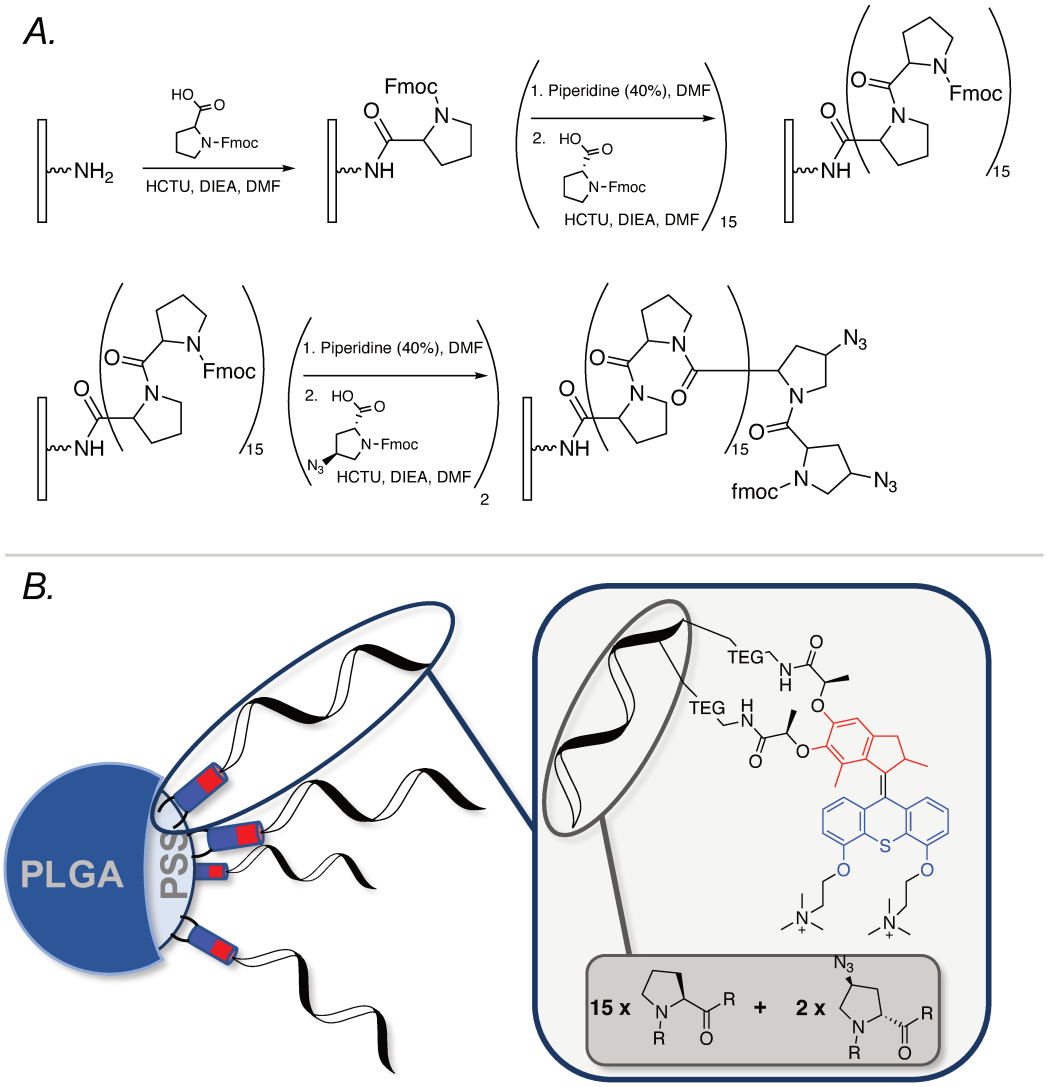

Figure IV.11 A. SPPS of a polyproline helix bearing 15 prolines and 2 azido-proline. **B.** Scheme depicting the design of the propellers and its corresponding molecular structure bearing a 15-unit polyproline.

General conclusion and outlook

My thesis focused on the integration of photo-activated unidirectional molecular motors into active systems in order to push the limits of what has already been achieved and to lay the foundations for future research. The work carried out was thus articulated around three main axes.

The first one consisted in a scale-up of the synthesis of a tetra-functionalized and orthogonally protected molecular motor. Indeed, although this task may seem simple at first sight, no less than 40 g were synthesised, in collaboration with my colleague Alexis Perrot, after more than 12 synthetic steps. This work has allowed us to better understand the limits of the processes used while optimising them as much as possible, which will save time for future syntheses.

The second axis concerned the use of visible light for the contraction of a polymer network containing molecular motors as cross-linking nodes thanks to the presence of a photosensitizer. Thus, I first demonstrated that the tetra-functionalized motor alone was indeed able to rotate at 530 nm by simple addition of Palladium(II) tetraphenylporphyrin in solution. I was then able to demonstrate that an energy transfer involving the triplet states of the motor takes place between the photosensitizer and the motor, but with a kinetic lower than what had been reported in the literature. Subsequent DFT calculations provided information on the origin of this difference, which arises from the fact that the calculated triplet energy level of the motor were slightly higher than those of the porphyrin. Nevertheless, I carried out the first gel irradiation experiments with visible light and studied the impact of the different parameters of the system, namely the porphyrin concentration and the light intensity. Overall, this approach allows to reach contraction rates close to the ones measured under UV irradiation, thus becoming the first example of material contraction incorporating unidirectional molecular motors powered by energy transfer ever reported. Following these exciting results, further research can be carried out to improve the efficiency of this energy transfer either by modifying the structure of the photosensitizer or by covalently integrating it into the polymer network. In the longer run, we can imagine coupling new modulating units such as spiropyran or spirooxazine, which were previously incompatible with UV irradiation, to provide a mechanosensitive reversibility to the contraction.

Finally, the third axis consisted in taking advantage of the rotation of molecular motors under UV irradiation to set Janus nanoparticles in motion. This work results from a productive collaboration between teams of polymer chemists (Prof. Serra, CMP, Strasbourg), organic chemists (SAMS, Strasbourg)and physicists (Prof. Buhler, LMSC, Paris). Using “homemade” Janus particles having negative charges on one side due to the presence of PSS, we managed to attach positively charged molecular motors thanks to electrostatic interactions. The nature of the non-covalent interactions between the motor and the JNPs was characterized using Zeta potential measurements, fluorescence experiments and electron microscopy. We then carried out further light scattering experiments to determine whether a propulsion effect was observed or not. To date, preliminary results from the so-called heterodyne SLS technique have revealed a ballistic component in the motion of the Janus particles. Although encouraging, these results remain to be confirmed through additional measurements. In the long term, we expect to determine the number of motors per particle in order to deduce a

propulsion force. Finally, we also plan to try to functionalise the rotor of the motors with propellers in order to eventually amplify their impact on the propulsion and therefore the speed of the JNPs. Overall, this work, if the results are confirmed, would be considered as the first example of nanoparticles propulsion by the combined action of light-fuelled molecular motors fixed on their surface. It would serve as a proof-of-concept and would eventually pave the way for the development of a new type of nanobots which would be powered solely by light irradiation, making their use in biological environments much more feasible.

Résumé de la thèse

Introduction

La double liaison est au cœur du mécanisme des moteurs moléculaires rotatoires. Un alcène combine à la fois des interactions σ et π et se caractérise par une vitesse de rotation extrêmement lente. En effet, s'éloigner de la configuration plane initiale nécessite la rupture de la liaison π. Par conséquent, la barrière d'énergie cinétique correspondante est trop élevée pour être franchie à température ambiante, ce qui permet la séparation des stéréoisomères E et Z. L'isomérisation *trans* --> *cis* a généralement lieu sous irradiation UV et l'inversion *cis* --> *trans* se produit généralement dans le domaine visible. Un encombrement stérique élevé au voisinage de la double liaison entraîne une déformation de la liaison en imposant un angle de torsion entre les différents groupes qui adoptent une hélicité gauche (*M*) ou droite (*P*). L'ajout de groupements chiraux à proximité de cette zone influence la stabilité relative des hélices et en favorise une par rapport à l'autre. Profitant de la différence de niveaux d'énergie, le premier moteur moléculaire consistait en deux tétrahydrophénanthrenes identiques reliés entre eux par une double liaison et fonctionnalisés en position *ortho* par deux groupes méthyles de même configuration absolue (*R*) (**Figure R.1A**).[1] Le système adopte initialement une organisation (*P,P*)-*trans*, qui est thermodynamiquement la plus stable (**Figure R.1B**). Sous irradiation UV à 280 nm, une photoisomérisation réversible forme l'intermédiaire (*M,M*)-*cis*. En raison de l'encombrement stérique induit par les groupements méthyles équatoriaux, une inversion thermique de l'hélice (ITH) se produit spontanément pour revenir à la configuration plus stable (*P,P*)-*cis*. Une photoisomérisation ultérieure à 280 nm entraîne un autre photoéquilibre en faveur d'un second intermédiaire instable, le (*M,M*)-*trans*. Une fois encore, afin de libérer la contrainte stérique et de ramener les méthyles à leur position axiale respective, une autre inversion thermique a lieu. Bien que thermodynamiquement favorisée, cette dernière nécessite le franchissement d'une barrière énergétique nettement plus élevée, d'où la nécessité de chauffer le milieu à 60°C. Le (*P,P*)-*trans* est ainsi régénéré après une rotation de 360° en quatre étapes. Globalement, la lumière alimente le système en le poussant hors d'équilibre, tandis que les groupes chiraux imposent l'unidirectionnalité qui permet de revenir à l'état le plus stable. Le moteur est donc autonome et fonctionne en continu tant qu'il est irradié.

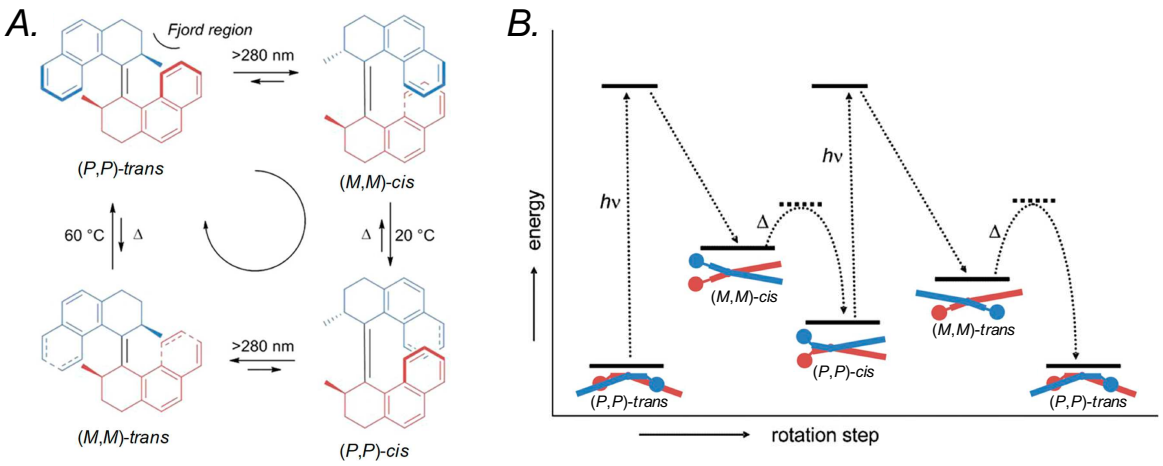

Figure R.1 A. Structure moléculaire et mécanisme du premier moteur unidirectionnel piloté par la lumière. **B**. Profil énergétique de chaque intermédiaire et vue de dessus correspondante. Adapté de réf. 3 et 2.

Un moteur moléculaire se caractérise par la mise en place d'un mouvement continu en produisant un travail tant qu'il est alimenté en énergie. Cependant, isolé en solution, le travail d'une machine est difficile à exploiter de manière utile. Pour cela, il est nécessaire de l'organiser au sein d'un système capable d'utiliser, de coordonner et même d'amplifier le travail produit pour réaliser des fonctions inédites. Notre groupe a développé un système capable d'effectuer des mouvements macroscopiques tout en stockant le travail produit par le moteur (**Figure R.2**).[6] Pour ce faire, un dérivé tétrafonctionnalisé de moteur de deuxième génération, caractérisé par deux points de fixation placés à la fois sur le rotor et le stator, a été synthétisé. Cette unité a ensuite été intégrée dans un réseau polymère covalent en tant que point de réticulation, conduisant à la formation d'un gel chimique de taille centimétrique. Lorsqu'il est placé sous irradiation UV, la rotation unidirectionnelle des moteurs déséquilibre le système, entraînant l'enroulement des chaînes de polymère les unes autour des autres. Cet enroulement entraîne une diminution de la longueur apparente de la chaîne, ce qui provoque une contraction macroscopique du matériau. À chaque cycle, le travail est stocké sous forme de tension mécanique par la torsion des polymères.

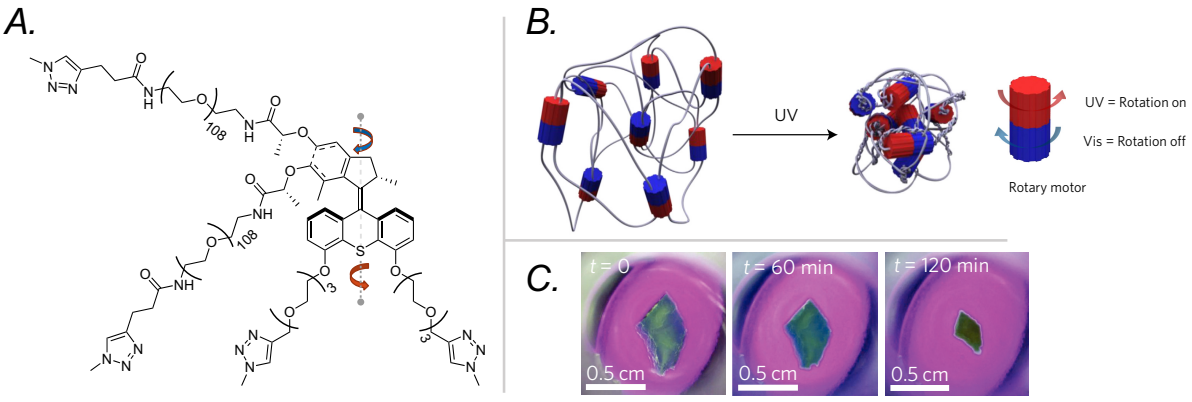

Figure R.2 A. Structure moléculaire du moteur tétrafonctionnalisé au sein du gel chimique. **B**. Représentation schématique de la contraction d'un gel sous irradiation UV. **C**. Instantanés de la contraction dans le temps. Adapté de la réf. 6.

Mes travaux au cours de cette thèse ont porté sur l'exploitation de ce moteur tétra-fonctionnalisé à travers deux thématiques différentes. Le premier consistait à développer des gels contractiles fonctionnant à des longueurs d'onde plus élevées, afin de limiter la dégradation inhérente à l'utilisation des UV. Le second volet de mes recherches visait à propulser des nanoobjets par la lumière. Pour cela, en collaboration avec deux autres groupes, nous avons conçu un système constitué de moteurs moléculaires ancrés sur des nanoparticules de Janus et étudié leur mouvement principalement par des expériences de diffusion de la lumière.

Synthèse à l'échelle de plusieurs grammes

Le moteur piloté par la lumière, qui a été utilisé pendant ma thèse, est adapté de cette deuxième génération. Une réactivité rapide est en effet essentielle pour le développement de matériaux intelligents. Deux acides carboxyliques et deux phénols, placés respectivement sur le rotor et le stator, ont été incorporés. Ces groupes sont initialement protégés de façon orthogonale, permettant ainsi une fonctionnalisation asymétrique de cette molécule. La synthèse est convergente, résultant d'un couplage Barton-Kellogg comme étape principale entre les parties supérieure et inférieure (**Figure R.3**).

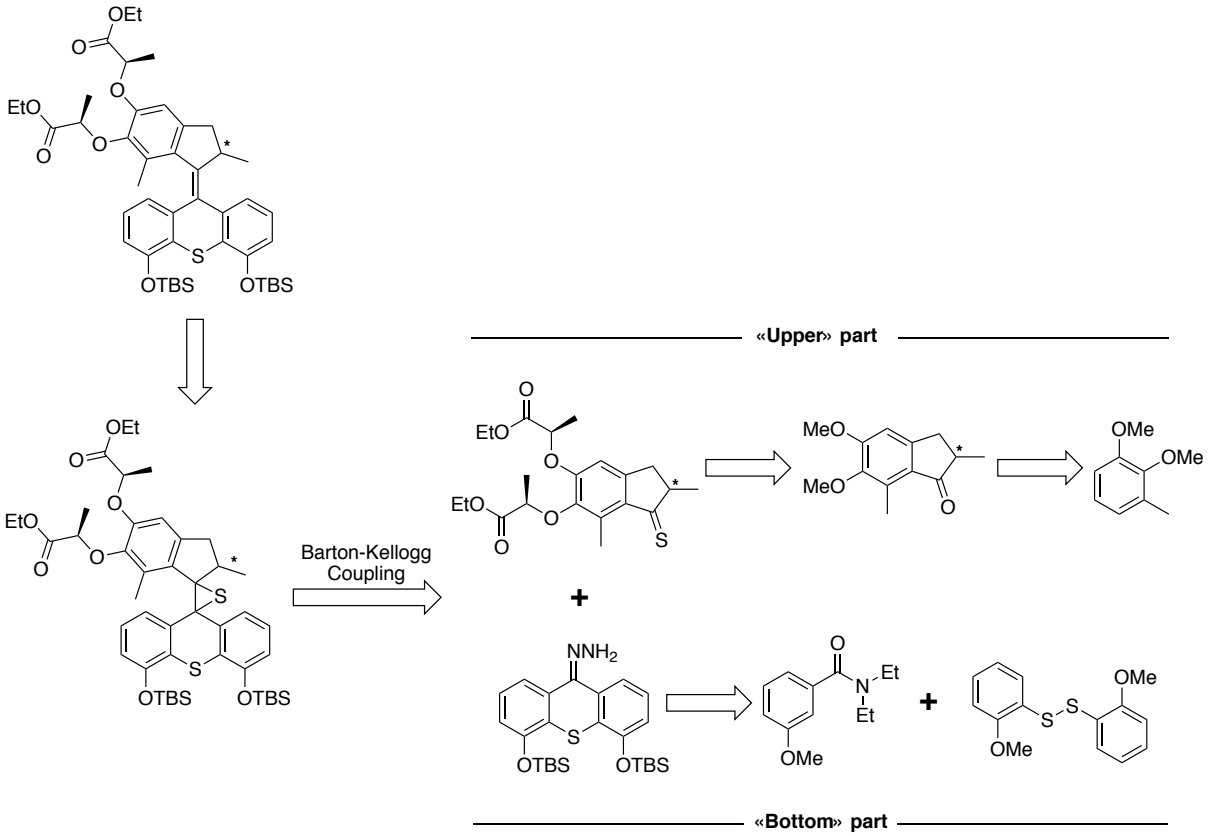

Figure R.3 Rétro-synthèse du moteur moléculaire à protection orthogonale.

Globalement, la mise à l'échelle synthétique de ce moteur moléculaire a permis d'obtenir plus de 40 g d'épisulfure prêt à l'emploi, soit 20 fois plus que ce qui avait été rapporté précédemment. Le moteur ainsi obtenu constitue l'élément clé pour le développement de nouveaux systèmes et matériaux photosensibles visés au cours de mon doctorat.

Contraction alimentée par la lumière visible

La lumière est un outil particulièrement puissant car elle est non invasive et pourtant facilement contrôlable dans le temps, l'espace et l'intensité. Dans le cas des moteurs à double liaison, une irradiation UV est généralement nécessaire pour générer un mouvement. À ces longueurs d'onde, la lumière est suffisamment énergétique pour provoquer un certain nombre d'effets indésirables. Les dommages peuvent se produire soit au niveau de la machine moléculaire, soit dans son environnement, par la formation de radicaux libres et leur photo-oxydation ultérieure.[107,108] Dans le cas des gels contractiles développés par notre équipe,[6,7] cela se traduit par une dégradation du réseau de polymères. En revanche, la lumière visible est inoffensive, disponible sur une large gamme de longueurs d'onde et sélective. Elle pénètre plus facilement les matériaux et est compatible avec les milieux biologiques. Cependant, elle reste moins énergétique, ce qui implique que des stratégies doivent être développées pour permettre la rotation des unités motrices à des longueurs d'onde plus élevées.[111]

À cette fin, l'ajout d'un photosensibilisateur a été étudié. Un photosensibilisateur est un chromophore caractérisé par sa capacité à transférer son état excité à un substrat proche par un processus intermoléculaire ou intramoléculaire avant de retourner à son état fondamental sans être altéré. Il implique souvent un état triplement excité en raison de leur durée de vie prolongée, ce qui augmente la probabilité d'interaction avec des substrats proches. Elle offre ainsi une gamme d'absorption plus large en faisant correspondre le niveau d'énergie de l'état excité sélectionné du substrat avec un chromophore approprié, et réduit considérablement la quantité de travail de synthèse, puisqu'il suffit d'ajouter un agent photosensibilisant en solution pour observer ses effets. Inspiré par le travail de pionnier de l'équipe de Feringa,[9,120] L'addition d'un photosensibilisateur à base de porphyrine et le transfert d'énergie intermoléculaire à triple état correspondant aux moteurs moléculaires ont été étudiés d'abord en solution, puis intégrés dans un gel contractile.

Pour tester si une interaction existe ou non, on peut suivre le cycle de rotation du moteur moléculaire en présence du photosensibilisateur. Pour cela, nous choisissons de briser la symétrie de la partie inférieure du système doit être brisée afin que les deux états stables puissent être distingués par RMN ^{1}H. Les isomères **E** et **Z** du moteur **18** ont été séparés par HPLC et l'un d'entre eux a été irradié en présence de Pd-TPP (ratio 1:1 à 11.8 mM dans $CDCl_3$) avec de la lumière visible (400-800 nm, 13.8 mW.cm^{-2}) (**Scheme R.1**).

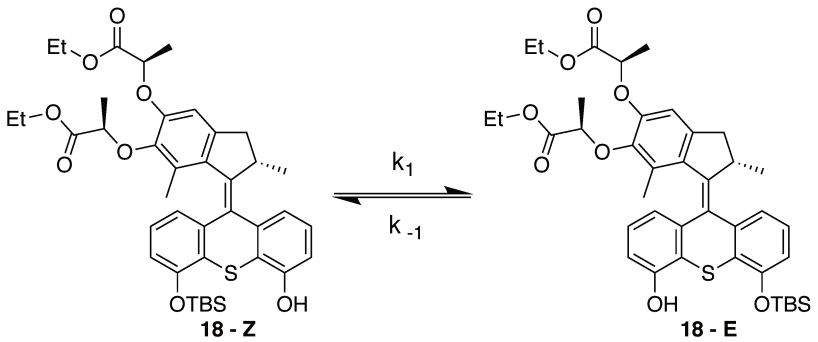

Scheme R.1 Structure moléculaire des isomères **Z** et **E** du moteur asymétrique **18**, k_1 et k_{-1} étant leurs constantes cinétiques de formation respectives.

L'évolution a ensuite été suivie par RMN ^{1}H, en utilisant l'intégration du signal du proton phénolique comme référence et en traçant l'évolution du rapport des isomères en fonction du temps (**Figure R.4A**). Malgré son apparente complexité, impliquant à la fois des photoréactions réversibles et des relaxations unidirectionnelles, ce système peut être décrit avec précision en utilisant un modèle standard d'isomérisation *cis-trans*. Le taux de formation de l'isomère E peut être écrit comme suit :

$$\frac{\mathrm{d}[\boldsymbol{E}]}{\mathrm{dt}} = k_1[\boldsymbol{Z}] - k_{-1}[\boldsymbol{E}] \qquad (\mathrm{R.1})$$

Après une résolution standard, en traçant $-ln([\boldsymbol{E}]_{eq} - [\boldsymbol{E}])$ en fonction du temps (**Figure R.4B**), nous avons réussi à déterminer le taux d'isomérisation apparent à partir de la pente :

$k_{iso\ (Vis)} = (2.44 \pm 0.12)\text{x}10^{-4}\ s^{-1}$ *où* $k_{iso} = k_1 + k_{-1}$ (13.9 mW.cm^{-2})

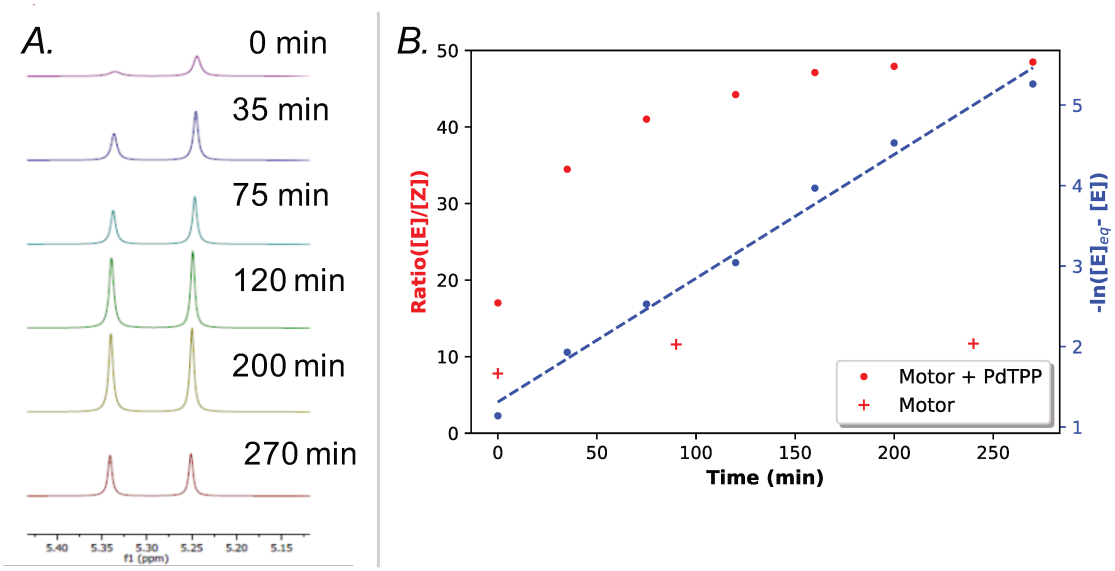

Figure R.4 A. Évolution du signal RMN du proton phénolique du moteur **18** en présence de Pd-TPP (tous deux à 11,8 mM dans $CDCl_3$) sous irradiation de lumière visible (530 nm). **B.** Evolution du **rapport d'isomérie** en fonction du temps en présence ou en l'absence de Pd-TPP et son **tracé cinétique** correspondant - Taux d'isomérisation : $k_{iso} = (2.44 \pm 0.12)10^{-4}\ s^{-1}$

L'interaction entre le Pd-TPP et un moteur moléculaire en solution étant maintenant caractérisée, son influence sur un gel contractile peut enfin être abordée. Une unité motrice

a été fonctionnalisée par quatre chaînes de triéthylène glycol avec azide terminal, qui ont été fabriquées à partir de triéthylène glycol. Le processus de préparation standard consiste à gonfler le matériau contractile dans une solution de Pd-TPP de 1,2,4-trichlorobenzène ($[Pd\text{-}TPP]_{max}$ = 0.2 g/L).

Les profils de contraction du gel ont été enregistrés à différentes concentrations de Pd-TPP (**Figure R.5A**). Une réduction du temps de contraction global ainsi que du temps de début de contraction a été observée lorsque la concentration du photosensibilisateur augmente. De même, la vitesse maximale de contraction augmentait avec la teneur en porphyrine. Nous avons donc mesuré l'influence du photosensibilisateur sur le temps de début de contraction et le temps de demi-contraction (**Figure R.5B**). Le temps de début de contraction correspond au délai nécessaire pour que les chaînes de polymère se tordent suffisamment avant de créer une tension dans le réseau. Le temps de demi-contraction correspond au moment où 50% de la contraction maximale est atteinte. Il est intéressant de noter que ces deux paramètres sont corrélés de manière similaire à la concentration en porphyrine. Plus la concentration de Pd-TPP est importante, plus les chances d'interaction avec un moteur sont élevées, donc plus la contraction est rapide et plus le délai est court.

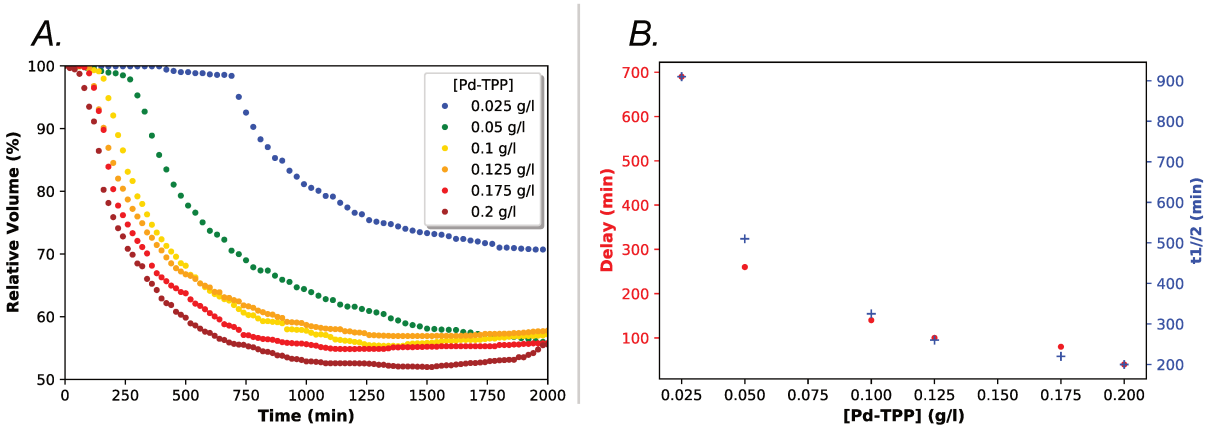

Figure R.5 A. Profils de contraction du gel à différents [Pd-TPP] (dans le 1,2,4-trichlorobenzène, λ_{exc} = 530 nm, P = 32 mW.cm^{-2}). **B.** Évolution du temps de début de contraction et du temps de demi-contraction $t_{1/2}$ en fonction de [Pd-TPP].

Globalement, pour une irradiation de P_{530} = 28.2 mW.cm^{-2}, une contraction maximale de 48% a été obtenue en environ 16 h pour une concentration de 0.2 g/L de photosensibilisateur. A la fin de la contraction, une relaxation du gel a été observée. Ce phénomène pourrait être causé par l'oxydation de la double liaison centrale des moteurs dont la réactivité est renforcée par l'augmentation de la tension. Un axe rotatif libre est alors formé, permettant le déroulement des chaînes de polymères et conduisant le gel à regonfler éventuellement. Par ailleurs, sous irradiation UV, une solubilisation du matériau a également pu être observée, indiquant une dégradation du réseau par excitation des molécules organiques et/ou formation d'espèces radicalaires. Ainsi, dans le 1,2,4-trichlorobenzène, aucune contraction n'a pu être mesurée sous UV en raison de la solubilisation rapide du gel, alors qu'à 530 nm, un tel processus ne s'est pas produit même après 5 jours d'irradiation constante. Le prochain défi consiste à améliorer l'efficacité du transfert d'énergie pour accélérer le processus de contraction.

Fonctionnalisation de particules de Janus

Le seul exemple de nano-nageurs incorporant un moteur sensible à la lumière est limité à l'échelle moléculaire (**Figure R.6**).[154] Dans ce travail, une étude comparative a montré une augmentation significative (jusqu'à 26%) du taux de diffusion des systèmes impliquant des moteurs moléculaires rapides (MHz) tant qu'ils sont placés sous irradiation UV. Dans le cas de moteurs rapides non-directionnels, une augmentation plus faible d'environ 10% a été observée. A l'inverse, les structures inertes (sans rotor) ou celles portant des moteurs moléculaires lents (mHz) n'ont montré aucun changement significatif de leur taux de diffusion. Il est intéressant de noter que la viscosité du solvant ne semble pas avoir un impact significatif sur la capacité du système à se déplacer. Globalement, bien que le mécanisme du mouvement reste à élucider, ces résultats démontrent clairement la capacité d'un moteur moléculaire à se propulser en solution.

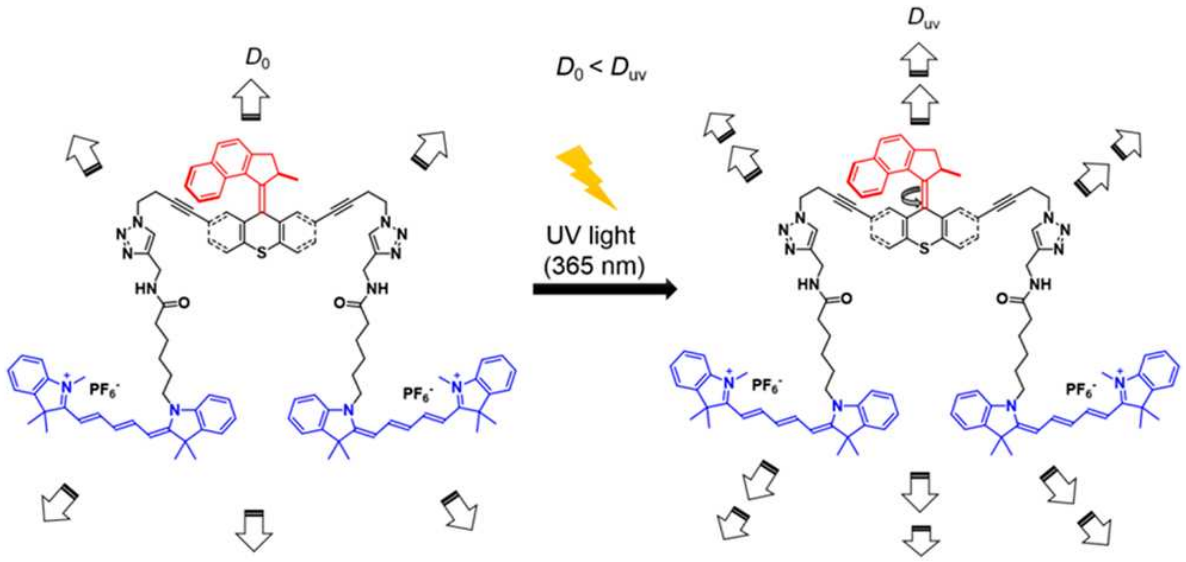

Figure R.6 Structure moléculaire de la nanomachine alimentée par la lumière. Lors de l'irradiation, une augmentation de 26% du taux de diffusion est observée. Adapté de la réf. 154.

Ainsi, inspiré par ces résultats et par le potentiel des moteurs moléculaires à base d'alcènes surpeuplés pour déplacer des nano-objets sur une surface,[103] nous avons étudié l'utilisation de ces unités fonctionnalisées par des hélices pour induire la propulsion de nanoparticules de Janus sous irradiation lumineuse. Nous avons initié une collaboration avec le groupe de Serra de l'ICS qui a récemment développé une méthode en une étape pour préparer des nanoparticules de Janus à partir de polystyrène sulfonate (PSS) et de poly(acide lactique-co-glycolique) (PLGA) par micromélange à flux allongé (**Figure R.7**).[156] Plus précisément, une solution aqueuse contenant du Pluronic® F-127 comme tensioactif est mélangée à une solution d'acétate d'éthyle dans laquelle les deux polymères sont solubilisés. Un système de double pompe permet la formation d'une émulsion grâce à un mouvement de va-et-vient à travers des microcanaux. Le mélange résultant est évaporé pour éliminer les traces de solvant organique. Les colloïdes formés ont une dimension d'environ 150 à 230 nm, déterminée par diffusion dynamique de la lumière, et sont relativement monodisperses (*cad* PDI = 0.1-0.24).

Ils sont stables pendant environ un mois dans une solution aqueuse et sont caractérisés par la présence d'un côté hydrophile et d'un côté hydrophobe.

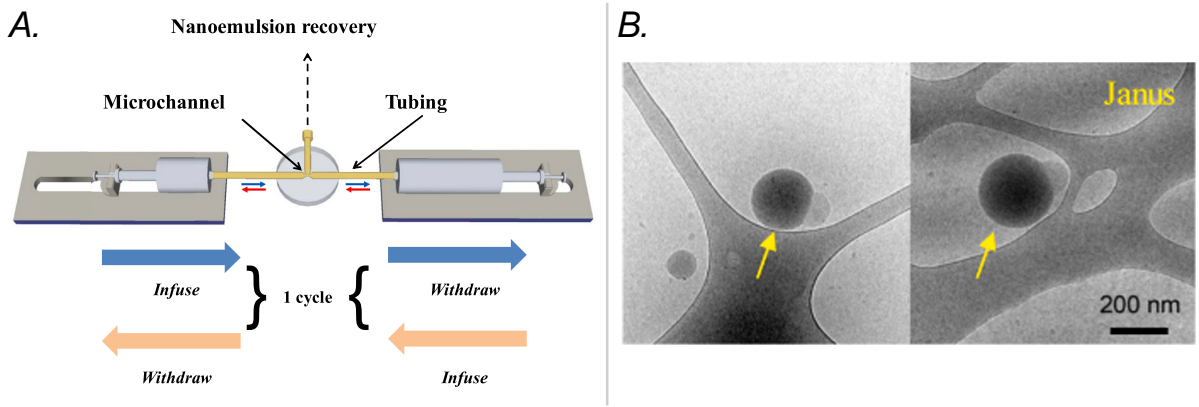

Figure R.7 A. Schéma décrivant le dispositif de micromélangeur à flux allongé. **B.** Clichés Cryo-TEM des particules résultant du micromélangeur (30 mL.min^{-1}, 150 cycles). Adapté de la réf 156.

Cependant, ces particules de Janus étaient difficiles à fonctionnaliser. Elles ne sont en effet stables que dans l'eau et ne supportent pas les hautes températures, ce qui limite considérablement l'éventail des réactions de couplage possibles avec les moteurs moléculaires, d'autant plus que ces derniers sont hydrophobes. Notre stratégie pour fonctionnaliser ces JNP a consisté à profiter de la présence de charges négatives du côté du PSS pour ancrer les moteurs moléculaires par des interactions électrostatiques. Nous avons ainsi conçu un moteur moléculaire qui présente deux groupes ammonium permanents sur le stator.

La présence de charges à la surface des JNP nous a permis de suivre l'évolution du potentiel Zeta sur la quantité de moteur. Le potentiel Zeta correspond à la différence de potentiel électrique entre la surface et le point de neutralité et peut être déduit de la mobilité électrophorétique des particules. Le PSS étant anionique, nous nous attendions à ce que l'addition progressive de moteurs moléculaires cationiques volumineux entraîne une diminution de la mobilité et une augmentation de la charge apparente. Ceci a été effectivement observé expérimentalement (**Figure R.8**). En pratique, les mesures ont été effectuées sur une gamme d'échantillons contenant toujours la même concentration de JNPs (soit 0.2 g/L), à laquelle une solution de moteur (à 0.1 g/L) a été ajoutée en quantités variables.

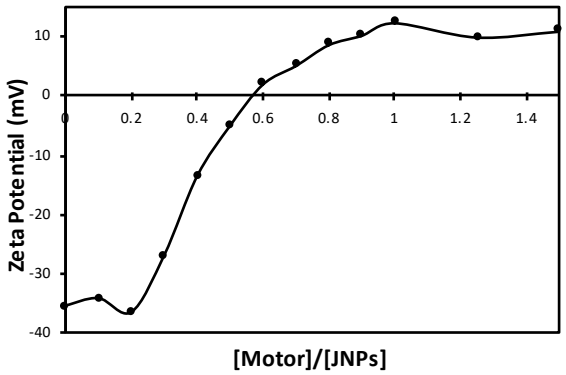

Figure R.8. Évolution du potentiel Zeta pour différentes particules de Janus - Rapport moteur. L'axe des abscisses correspond au rapport entre la concentration massique du moteur et celle des particules, la masse molaire des nanoparticules restant à déterminer.

Initialement, pour les JNP pures, le potentiel mesuré est faible, aux alentours de -35 mV, en accord avec la présence de moitiés chargées négativement. Pour des rapports de concentration inférieurs à 0.2, nous avons observé la présence d'un plateau, qui pourrait être lié au remplissage de la couche superficielle par les moteurs, ce qui a peu d'influence sur le plan de glissement et donc sur la valeur du potentiel. Ensuite, pour des rapports de concentration compris entre 0.2 et 1, on observe une augmentation rapide du potentiel, correspondant très probablement au remplissage progressif de la double couche ionique, qui a la plus grande influence sur l'électromobilité. Enfin, pour des rapports de concentration supérieurs à 1, on distingue un second plateau, qui atteste de la saturation de la seconde couche.

Pour confirmer davantage la présence d'interactions entre les moteurs et les JNP, nous avons réalisé une étude de fluorescence en l'absence ou en présence de JNP, en utilisant le pic de diffusion Raman comme référence pour la normalisation. Dans un premier temps, nous avons mesuré les spectres d'émission du moteur seul en solution sur une gamme de concentration allant de 0.01 g/L à 0.1 g/L. L'évolution est linéaire comme attendu pour un moteur en solution. L'évolution est linéaire comme attendu pour un chromophore isolé en solution à une concentration relativement faible. Cependant, en présence de particules de Janus à 0.2 g/L, le spectre de fluorescence du moteur sur la même gamme de concentration a évolué de façon très différente (**Figure R.9**). En effet, pour les mêmes paramètres de réglage, une augmentation d'un facteur 10 de l'émission est observée avec, cette fois, l'apparition d'un plateau à partir d'un rapport de concentration de 0.4 g/L. Ce type de phénomène se produit couramment lorsqu'un fluorophore est immobilisé sur une surface. En revanche, la présence d'un plateau pour une concentration supérieure à 0.4 suggère l'existence d'un processus de quenching de la fluorescence, qui est certainement lié à l'augmentation de la concentration du moteur à la surface des particules. Un transfert d'énergie peut se produire, limitant les processus radiatifs.

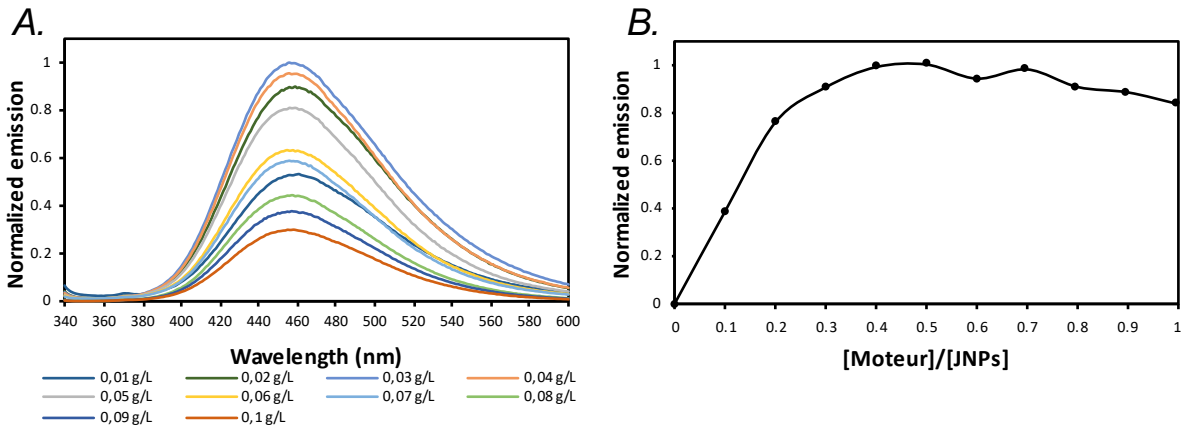

Figure R.9 A. Spectres de fluorescence du moteur moléculaire à différentes concentrations dans l'eau en présence de JNPs (0.2 g/L) (λ_{exc} = 330 nm) **B.** Évolution de l'émission du moteur + JNPs en fonction du rapport de concentration.

Globalement, la mesure du potentiel zêta et les expériences de fluorescence suggèrent ensemble la présence de moteurs moléculaires à la surface des nanoparticules de Janus. Pour attester de leur propulsion sous irradiation UV, il est nécessaire d'utiliser des méthodes de caractérisation avancées basées sur la diffusion, telles que la diffusion statique de la lumière qui consiste à mesurer l'intensité diffusée (I) des particules dispersées en solution en fonction de l'angle de mesure (θ), qui peut également être représenté sous la forme d'un vecteur d'onde de diffusion (q).

$$q = \frac{4\pi sin\theta}{\lambda} \qquad (\text{R. 2})$$

Ici, λ correspond à la longueur d'onde de la lumière incidente. Il s'agit d'une technique puissante puisqu'elle permet de déterminer des propriétés physiques telles que le rayon de giration moyen apparent (RG), correspondant à la racine du carré moyen de la distance entre le centre de masse et les monomères, ou la masse molaire moyenne (MW) des particules par extrapolation de I à $q^2 = 0$, si l'on a accès aux valeurs dn/dc.[159] Dans notre cas, cette mesure a été effectuée sur trois échantillons différents constitués de JNP seules, de JNP en présence de moteurs et enfin de JNP avec moteurs tout en irradiant in-situ avec une LED UV. (**Figure R.*10*A**). Les courbes obtenues sont relativement similaires et toutes trois suivent la forme d'une exponentielle décroissante, caractéristique d'un régime de Guinier (**Figure R.*10*B**).

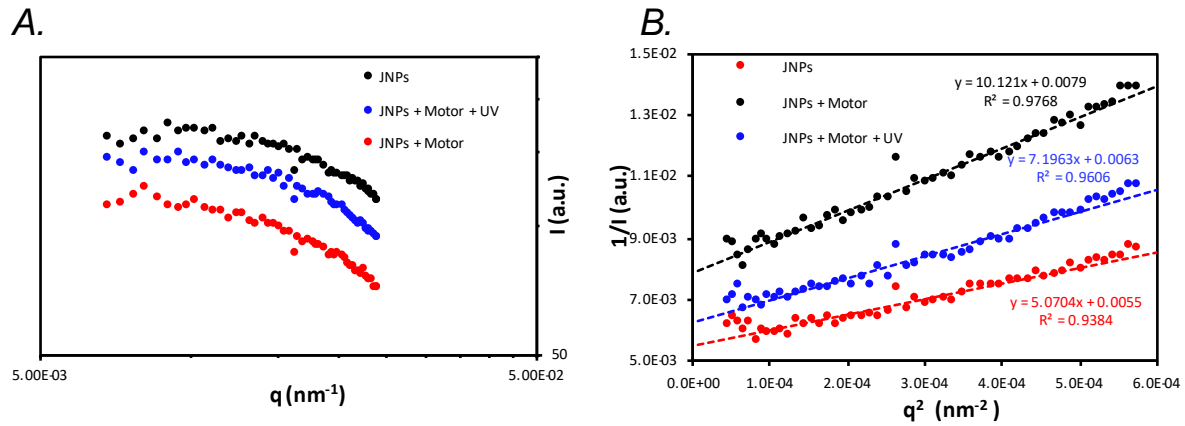

Figure R.10. A. Mesure de la diffusion statique de la lumière (SLS) des JNP (0.2 g/L) avec ou sans moteur (0.1 g/L) en présence ou en l'absence d'irradiation UV. **B.** Tracé de Guinier des mesures SLS et régression linéaire correspondante.

Le tracé de Guinier des données SLS permet de déterminer le RG apparent selon le modèle de Guinier :

$$\frac{1}{I(q)} = \frac{1}{I(q^2 = 0)}\left(1 + \frac{q^2 R_G^2}{3}\right) \qquad (\text{R.3})$$

La régression linéaire des données expérimentales a donné les valeurs suivantes, en négligeant l'effet Virial (c'est-à-dire les interactions entre chaque objet) :

$R_G^{(\text{JNPs})}$ = 52.5 nm

$R_G^{(\text{JNPs + Mot})}$ = 62 nm

$R_G^{(\text{JNPs + Mot + UV})}$ = 58.4 nm

Une petite augmentation du rayon de giration a été observée après l'ajout des moteurs moléculaires et une diminution relative a été repérée lorsque le système est placé sous irradiation UV. Cette augmentation est cohérente avec l'ajout du moteur à la surface des particules.

Par la suite, des expériences de diffusion dynamique homodyne ont été réalisées. Cette technique donne accès à la polydispersité (PDI) de l'échantillon et a montré un processus diffusif unique (*cad* Brownien) avec ou sans UV ainsi qu'un temps caractéristique inversement proportionnel à q^2 permettant la détermination du diamètre hydrodynamique apparent (DH) des particules. Ce dernier est relié au rayon hydrodynamique apparent (RH), qui correspond à la taille d'une particule sphérique diffusant à la même vitesse, via la relation de Stockes-Einstein si la température et la viscosité du solvant sont connues. Le RH peut donc également fournir des informations sur la géométrie des objets utilisant le rapport :

$$\rho = \frac{D_H}{2R_G} \qquad (\text{R.4})$$

Les valeurs suivantes ont été mesurées à une concentration fixe et en négligeant l'effet Virial :

PDI = 0.11 $D_H^{(\text{JNPs})}$ = 138 nm ρ = 1.31

PDI = 0.19 $D_H^{(\text{JNPs + Motor})}$ = 132 nm ρ = 1.06

PDI = 0.19 $D_H^{(JNPs + Motor + UV)}$ = 132 nm ρ = 1.13

Nous pouvons immédiatement remarquer que la polydispersité des JNP pures est assez bonne, avec une valeur de 0.11. Cette valeur diminue légèrement avec l'ajout de moteurs, ce qui pourrait éventuellement être lié à une distribution inhomogène des cations parmi les particules. Concernant le diamètre hydrodynamique, nous pouvons observer que l'ajout de moteurs diminue la taille apparente, qui passe de 138 nm à 132 nm. Ce phénomène n'est pas complètement compris, mais pourrait être causé par un effet d'écran électrostatique des particules par les moteurs.

Par ailleurs, le rapport ρ indique que ces nano-objets sont initialement dotés d'une géométrie proche de la sphère dure ($\rho_{(sphère\ dure)}$ = 1.29), mais qu'elle diminue ensuite avec l'ajout de moteurs. Ces derniers n'étant pas uniformément répartis sur la surface, ce rapport ρ plus faible pourrait s'expliquer par le fait que les particules peuvent subir une petite déformation de leur structure apparente.

Enfin, nous observons que le diamètre hydrodynamique reste identique en présence ou en l'absence d'irradiation UV. Un tel résultat est tout à fait normal dans le cas d'une expérience de diffusion dynamique de la lumière homodyne, puisque cette technique ne permet d'accéder à la constante de diffusion qu'en capturant la lumière diffusée, contrairement à la technique dite hétérodyne. Celle-ci consiste à ajouter au faisceau diffusé un second signal de référence dérivé de la déviation partielle du laser incident (**Figure R.11**),[160] permettant ainsi de connaître la vitesse moyenne de dérive des particules en solution. A ce jour, une composante balistique (par exemple une diffusion forcée) dans la fonction d'autocorrélation de l'intensité a pu être observée permettant la détermination d'un facteur de structure dynamique complexe (au sens des nombres complexes). Ces résultats préliminaires sont donc encourageants et semblent attester de la capacité des moteurs à propulser une structure. Cependant, des analyses et des calculs supplémentaires sont encore nécessaires avant de pouvoir les valider pleinement.

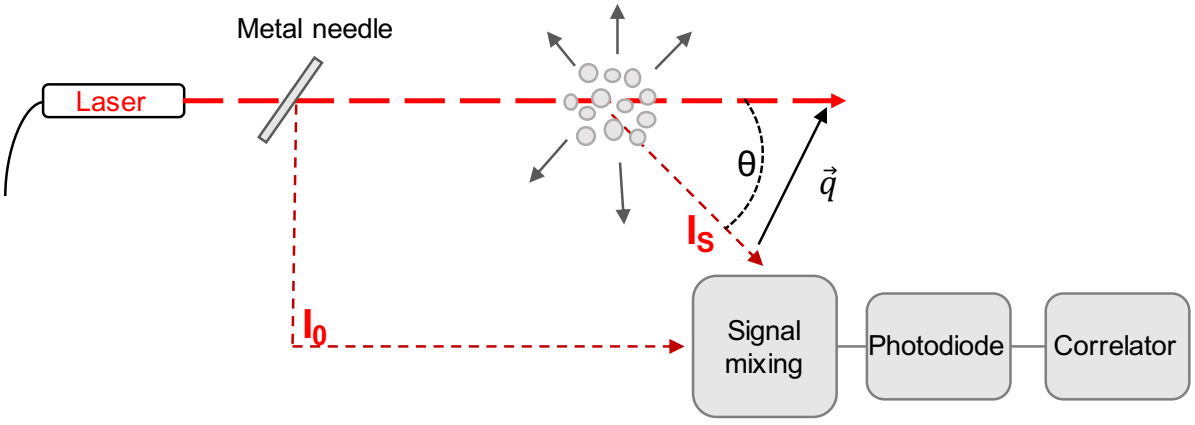

Figure R.11. Schéma décrivant une configuration de diffusion dynamique de la lumière hétérodyne où I_0 est le faisceau de référence, I_S le faisceau diffusé, θ l'angle de diffusion et q le vecteur d'onde de diffusion.

Globalement, nous pensons que le travail rapporté dans ce manuscrit constitue une avancée certaine dans le domaine des systèmes autopropulsés, grâce à la collaboration fructueuse de chimistes, physico-chimistes et physiciens. En effet, en utilisant des particules Janus à base de PLGA et de PSS, nous avons réussi à les fonctionnaliser avec des moteurs moléculaires de type Feringa grâce à des interactions électrostatiques, déterminées par des mesures de potentiel Zeta et des expériences de fluorescence. Enfin, des analyses de diffusion de lumière dynamique et statique nous ont permis de caractériser précisément ces nano-objets, dont les derniers résultats suggèrent (mais restent à confirmer) qu'ils peuvent être propulsés.

Experimental Section

General methods

All general reagents and solvents were purchased at the highest commercial quality and used as received (Sigma Aldrich, Acros and TCI). Bis-alkyne-PEG5600 (Mp = 5600 Da) was purchased from Iris Biotech. All reactions were carried out under an Argon atmosphere with dry solvents unless otherwise noted. Dry solvents were obtained using a double column SolvTech purification system. Water was deionized by using a milli-gradient system (Millipore, Molsheim, France). Yields refer to purified spectroscopically (^{1}H NMR) homogeneous materials. Thin Layer Chromatographies were performed with TLC silica on aluminium foils (Silica Gel/UV254, Aldrich). In most cases, irradiation using a Bioblock VL-4C UV-Lamp (6 W, 254 nm and/or 365 nm) as well as *p*-anisaldehyde, phosphomolybdic acid and Cerium ammonium molybdate stainings were used for visualization. Ultra-performance liquid chromatography coupled to mass spectrometry (UPLC-MS) was recorded on a Waters Acquity UPLC-SQD machine equipped with a PDA detector (190-500 nm, 80 Hz), using a reverse phase column (Waters, BEH C18 1.7 µm, 2.1 × 50 mm), MassLynx 4.1 – XP software for analysis, and a water/acetonitrile/0.1% formic acid mixture gradient as eluent. Preparative HPLC was performed on a Waters Autopurify system equipped with a UV detector (λ = 300 nm), a 3100 mass spectrometer, a reverse phase column (Waters, Sun Fire Prep C_{18} 5.0 µm, 19 × 150 mm) running with a water/methanol/0.1% formic acid gradient as eluent, and the MassLynx 4.1 – XP software for analysis. HRMS mass spectra were recorded on a Micro-Q-TOF apparatus from Bruker.

NMR spectra were recorded on a Bruker Avance 400 MHz spectrometer with working frequencies of 400 and 101 MHz for ^{1}H and ^{13}C nuclei, respectively. ^{1}H and ^{13}C NMR spectra were internally referenced to the residual proton solvent signal ($CDCl_3$: 7.26 ppm, CD_3OD: 3.31 ppm and $(CD_3)_2CO$: 2.05 ppm for ^{1}H spectrum, and $CDCl_3$: 77.16 ppm, $(CD_3)_2CO$:206.26 and 29.84 ppm and CD_3CN: 118.26 and 1.32 ppm for ^{13}C spectrum) and all chemical shifts are given in ppm. Coupling constants J are listed in Hz. The following notation is used for the ^{1}H NMR spectral splitting patterns: singlet (s), doublet (d), triplet (t), pentuplet (p), septuplet (sept), multiplet (m), large (l). UV-Vis spectra were recorded on a Perkin-Elmer Lambda-25 spectrophotometer with quartz glass cuvettes S3 of 1 cm optical path. All spectroscopy samples were measured at room temperature unless otherwise noted.

DLS and Zeta Potential measurements were performed on a ZetaSizer Nano ZS (Malvern Instruments, Worcestershire, U.K.) using a standard Zeta Potential cuvette and always at 25°C. Fluorescence emission spectra were recorded on a FluoroMax-4 spectrofluorometer from Horiba Jobin-Yvon.

Emission spectra and lifetime measurements were recorded on a Fluorolog FL3-22.

The measurements performed at Laboratoire Matière et Systèmes Complexes (Paris) used a 3D LS spectrometer (LS Instruments, Fribourg, Switzerland) equipped with a 25 mW HeNe

laser (JDS uniphase) operating at l = 632.8 nm, a two channel multiple tau correlator (1088 channels in autocorrelation), a variable-angle detection system, and a temperature controlled index matching vat (LS Instruments). The scattering spectrum was measured using two single mode fibre detections and two high sensitivity APD detectors (PerkinElmer, model SPCM-AQR-13-FC). Fluctuations in the scattered intensity with time I(q,t) (also called count rate), measured at a given scattering angle, theta, or equivalently at a given scattering wave vector, q = (4*π*n/λ)*sin(θ/2), are directly reflecting the so-called Brownian motion of the scattering particles (refractive index n = 1.33 at 20°C for water). In dynamic light scattering (DLS), the fluctuation pattern is translated into the normalized time autocorrelation function of the scattered intensity. For a diffusive process with a characteristic time inversely proportioned to q^2, $g(2)(q,t) = B \exp(-2Dq^2t)$, with D the mutual diffusion coefficient. The Stokes–Einstein relation permits to determine the hydrodynamic radius (Rh) of the scattered objects; Rh = kT/6π*θD, if the temperature T and solvent viscosity eta are known (here eta = 1 cP at 20°C for water). The size distribution was determined using the classical cumulant method and the CONTIN algorithm based on the inverse Laplace transform of the correlation function.

To analyse the morphology and shape of the composite nano-particles, cryo-transmission electron microscopy (cryo-TEM) experiments were performed. A 5 µL drop of the JNPs suspension was deposited onto a lacey-holey carbon film (Ted Pella) freshly glow discharged (Elmo, Cordouan Technologies). The grid was rapidly frozen in liquid ethane cooled by liquid nitrogen in a home-made environment- controlled machine. The grids were mounted onto a Gatan 626 cryoholder and observed in a Tecnai G2 (FEI-Eindhoven) operating at 200 kV and the images were taken with an Eagle 2k2k ssCCD camera (FEI- Eindhoven) under low dose conditions. The contrast was, in that case, directly related to the atomic number of the diffusing atoms.

Synthetic procedures

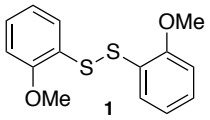

1

Compound (**1**) – 1,2-bis(2-methoxyphenyl)disulfane

To a stirred, biphasic solution of 2-methoxythiophenol (1 eq., 70.0 g, 61 mL, 500 mmol) in water (150 mL) was added dropwise a solution of iodine (1.01 eq., 129 g, 505 mmol) in methanol (500 mL) until the brown iodine colour persisted. The mixture was stirred at rt overnight. The solution was filtered, the solid was collected and dried to afford compound **1** (70.0 g, 250 mmol, 99%) as a white powder.

R_f = 0.4 (Et_2O:cyclohexane = 1:6)**.**

^{1}H NMR ($CDCl_3$, 400 MHz, 298°C) δ = 7.53 (dd, *J* = 7.6, 1.2 Hz, 2H), 7.19 (dd, *J* = 7.6, 7.6 Hz, 2H), 6.93-6.89 (m, 2H), 6.85 (d, *J* = 8.4 Hz, 2H), 3.90 (s, 6H).

^{13}C NMR ($CDCl_3$, 100 MHz, 298°C) δ = 156.5, 127.7, 127.5, 124.5, 121.3, 110.4, 55.8.
MS (ESI): m/z calculated for $C_{14}H_{16}O_2S_2$ $[M+H]^+$: 279.05, Found: 279.15.

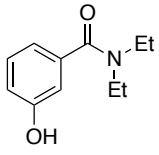

2

Compound (**2**) – *N*,*N*-diethyl-3-hydroxybenzamide

To 3-hydroxybenzoic acid (1 eq., 43.6 g, 315.7 mmol) were added thionyl chloride (8 eq., 312 g, 190 mL, 2.59 mol) in excess and DMF (1 mL) at room temperature under an argon atmosphere. The mixture was then refluxed at 70°C for 1 h and then cool down to room temperature. The excess thionyl chloride was removed under vacuum and further azeotropped with toluene. Then dry dichloromethane (175 mL) was added and the solution was treated slowly with diethylamine (3.6 eq., 83 g, 118 mL, 1.14 mol) at 0°C. The mixture was further stirred at 0 °C for 1 h. After the evaporation of the solvent, the mixture was dispersed in water (250 mL) and the pH was adjusted to 2-3 with hydrochloric acid and then extracted with ethyl acetate (150 mL × 4). The combined organic layers were dried over sodium sulphate and evaporated to give the compound **2** (59.4 g, 307 mmol, 97 %) as brown crystals.
^{1}H NMR ($CDCl_3$, 400 MHz, 298°C) δ = 8.65 (s, 1H), 7.15 (t, *J* = 8.5 Hz, 1H), 6.84-6.80 (m, 1H), 6.78- 6.74 (m, 2H), 3.55 (br s, 2H), 3.23 (br s, 2H), 1.20 (br s, 3H), 1.10 (br s, 3H).
^{13}C NMR ($CDCl_3$, 100 MHz, 298°C) δ = 172.7, 157.3, 137.2, 129.1, 117.0, 116.8, 114.5, 43.9, 39.5, 14.2, 12.7.
MS (ESI): m/z calculated for $C_{14}H_{15}O_2S_2$ $[M+H]^+$: 279.05, Found: 279.15.

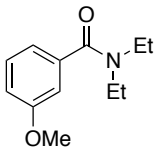

3

Compound (**3**) – *N*,*N*-diethyl-3-methoxybenzamide

To a solution of compound **2** (1 eq., 77.5 g, 400 mmol) in acetone (650 mL) was added potassium carbonate (3 eq., 168 g, 1.21 mol) and methyl iodide (2.9 eq., 171 g, 75 mL, 1.19 mol) dropwise and the mixture was then stirred overnight at room temperature. After evaporation of the solvent, the crude residue was partitioned between water (100 mL) and ethyl acetate (2 x 200 mL). The organic phases were combined and dried over sodium sulphate. Evaporation of the solvent under reduced pressure afforded compound **3** (83.3 g, 401 mmol, 100 %) as a brown liquid.
R$_f$ = 0.3 (Et_2O:cyclohexane = 1:2).

^{1}H NMR ($CDCl_3$, 400 MHz, 25°C) δ = 7.30 (ls, 1H), 6.94-6.90 (m, 3H), 3.88 (ls, 3H), 3.84 (ls, 2H), 3.55 (ls, 2H), 1.24 (ls, 3H), 1.12 (ls, 3H).
^{13}C NMR ($CDCl_3$, 100 MHz, 25°C) δ = 170.8, 159.4, 138.4, 129.3, 118.2, 114.8, 111.5, 55.1, 43.1, 39.0, 14.1, 12.7.
MS (ESI): m/z calculated for $C_{12}H_{18}NO_2$ $[M+H]^+$: 209.13, Found: 209.19.

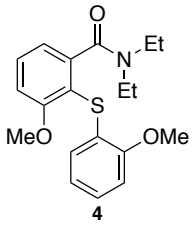

4

Compound (**4**) – *N*,*N*-diethyl-3-methoxy-2-((2-methoxyphenyl)thio) benzamide

In a three-neck round-bottom flask adapted with an Argon entry, an addition funnel and a thermocouple, TMEDA (1 eq., 14.0 g, 18.2 mL, 120 mmol) was dissolved in THF (150 mL). The mixture was cooled down to -78°C using an acetone/dry ice bath. Once the temperature reached -80°C/-78°C, *s*-BuLi (2 eq., 1.4 M in THF, 172 mL, 241 mmol) was added dropwise to the mixture through an addition funnel over 1 hour. During this time, a solution of compound **3** (1 eq., 25.0 g, 120 mmol) was dissolved in THF (100 mL) under an argon atmosphere and was cooled down to -78°C as well. After 1 hour, the solution containing compound **3** was cannulated in an addition funnel and added dropwise and the mixture was stirred at -78°C for 1 hour. A solution of compound **1** (1.8 eq., 60.4 g, 217 mmol) in THF (350 mL) under an argon atmosphere was then added through the addition funnel over 1 hour. At the end of the addition, the mixture was stirred overnight while going back to room temperature. The mixture was diluted with Et_2O (150 mL) and washed with 1 M NaOH solution (2 x 300 mL). The organic layer was dried over sodium sulphate and then was concentrated under reduced pressure. The crude residue was then purified by column chromatography (silica gel, EtOAc:toluene = 1:6) to provide the desired compound **4** as a white solid (20.4 g, 59 mmol, 49 % yield).
R_f = 0.2 (toluene:EtOAc = 2:1).
^{1}H NMR ($CDCl_3$, 400 MHz, 298°C) δ = 7.43 (t, *J* = 8.0 Hz, 1H), 7.06-7.02 (m, 1H), 6.95-6.93 (m, 2H), 6.78 (d, *J* = 7.6 Hz, 1H), 6.75-6.67 (m, 2H) 3.87 (s, 3H), 3.74 (s, 3H), 3.73-3.64 (m, 1H), 3.39-3.30 (m, 1H), 3.15-3.06 (m, 1H), 3.04-2.95 (m, 1H), 1.18 (t, *J* = 6.8 Hz, 3H), 0.98 (t, *J* = 7.2 Hz, 3H).
^{13}C NMR ($CDCl_3$, 100 MHz, 25°C) δ = 168.6, 160.5, 155.6, 145.2, 131.1, 127.0, 125.8, 125.4, 120.9, 118.7, 116.1, 111.2, 110.2, 56.1, 55.7, 42.6, 38.5, 13.8, 12.4.
HRMS: m/z calculated for $C_{19}H_{23}LiNO_3S$ $[M+Li]^+$: 352.155, Found: 352.155.

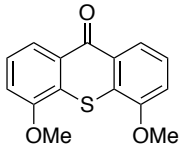

5

Compound (**5**) – 4,5-dimethoxy-9H-thioxanthen-9-one

To a solution of diisopropylamine (5.01 eq., 37.9 g, 53 mL, 375 mmol) in THF (530 mL) was added under an argon atmosphere *n*-butyllithium (5.02 eq., 1.6 M, 235 mL, 376 mmol) at -78°C. After 30 min the dry ice bath was removed. To the newly prepared LDA solution was added a solution of compound **4** (1 eq., 28.8 g, 74.8 mmol) in THF (350 mL) dropwise at 0°C over 1 hour. The mixture was then stirred at room temperature overnight. After that time a saturated NH_4Cl solution (10 mL) was added. The mixture was extracted with ethyl acetate (20 mL x 3). The combined organic phase was dried over sodium sulphate and concentrated under reduced pressure affording the desired compound **5** (19.2 g, 70.6 mmol, 94 %) as a yellow solid.

***R*$_f$** = 0.47 (toluene).

^{1}H NMR ($CDCl_3$, 400 MHz, 25°C) δ = 8.25 (dd, *J* = 8.0, 0.8 Hz, 2H), 7.45 (dd, *J* = 8.0, 8.0 Hz, 2H), 7.16-7.13 (dd, *J* = 8.0, 0.8 Hz, 2H), 4.06 (s, 6H).

^{13}C NMR ($CDCl_3$, 100 MHz, 25°C) δ = 180.2, 154.9, 130.0, 127.7, 126.0, 121.5, 112.1, 56.4.

HRMS: m/z calculated for $C_{15}H_{12}LiO_3S$ $[M+Li]^+$: 279.066, Found 279.066.

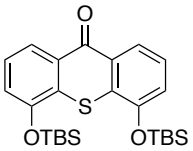

6

Compound (**6**) – 4,5-bis((*tert*-butyldimethylsilyl)oxy)-9*H*-thioxanthen-9-one

Deprotection

To a solution of the compound **5** (1 eq., 35.2 g, 129 mmol) in dry dichloromethane (750 mL) was slowly added boron tribromide (3.9 eq., 126 g, 47.6 mL, 503 mmol) at 0°C. The mixture was then stirred at room temperature overnight. The reaction mixture was cooled down to 0°C before slowly adding MeOH (250 mL). The solvent was then evaporated under reduced pressure. To remove all BBr_3residues, this procedure was repeated at least three times. The resulting product was then used directly in the next step without further purification.

Protection

To a solution of the crude bis-phenol in dry THF (1300 mL) were added imidazole (3 eq., 26.4, 387 mmol)and *tert*-butyldimethylsilyl chloride (3 eq., 58.4 g, 67.1 mL, 387 mmol) at room temperature under an argon atmosphere. The mixture reaction was stirred overnight. The mixture reaction was then filtered, concentrated under reduced pressure and purified by flash

column chromatography (silica gel, toluene) affording compound **6** (43.4g, 91.9 mmol, 71 %) as a yellow solid.

R_f = 0.7 (toluene:EtOAc = 6:1).

^{1}H NMR ($CDCl_3$, 400 MHz, 25°C) δ = 8.24 (dd, *J* = 8.1, 1.5 Hz, 2H), 7.36 (dd, *J* = 8.1, 8.1 Hz, 2H), 7.11 (dd, *J* = 8.1, 1.5 Hz, 2H), 1.10 (s, 18H), 0.37 (s, 12H).

^{13}C NMR ($CDCl_3$, 100 MHz, 25°C) δ = 180.7, 151.3, 130.7, 130.1, 125.9, 122.0, 119.5, 25.8, 18.8, -4.2.

HRMS: m/z calculated for $C_{25}H_{36}LiO_3SSi_2$ $[M+Li]^+$: 479.208, Found: 479.207.

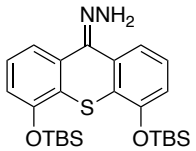

7

Compound (**7**) – (4,5-bis((*tert*-butyldimethylsilyl)oxy)-9*H*-thioxanthen-9-ylidene)hydrazine

Thioketone formation

To a solution of compound **6** (1 eq., 22.2 g, 43.8 mmol) in THF (300 mL) under an argon atmosphere was added phosphorous pentasulfide (3.15 eq., 30.7 g, 138 mmol). The mixture reaction was stirred at 60-65°C for 1 hour. After cooling down to room temperature, the mixture was filtered and the residue was washed with dichloromethane (200 mL) or until the eluent became colourless. The solvent was then evaporated under reduced pressure to afford a brown solid which was used as such in the next step.

Hydrazone formation

The crude residue was dissolved in ethanol (600 mL) under an argon atmosphere. Hydrazinmonohydrate (5.34 eq., 23.4 g, 22.8 mL, 234 mmol) was added dropwise at 0°C. The mixture was stirred at room temperature overnight. The reaction mixture was then evaporated under reduced pressure at room temperature. The resulting orange solid was purified by flash column chromatography (alumina gel, toluene:EtOAc = 2:1) affording compound **7** (13.0 g, 26.6 mmol, 61 %) as an orange solid.

^{1}H NMR ($CDCl_3$, 400 MHz, 25°C) δ = 7.66 (dd, *J* = 8.0, 1.3 Hz, 1H), 7.43 (dd, *J* = 8.0, 1.3 Hz, 1H), 7.25 (dd, *J* = 8.0 , 8.0 Hz, 1H), 7.15 (dd, *J* = 8.0, 8.0 Hz, 1H), 6.82 (dd, *J* = 8.0, 1.0 Hz, 1H), 6.78 (dd, *J* = 8.0, 1.2 Hz, 1H), 1.09 (s, 9H), 1.06 (s, 9H), 0.33 (s, 6H), 0.25 (s, 6H).

^{13}C NMR ($CDCl_3$, 100 MHz, 25°C) δ = 152.3, 150.7, 142.1, 135.0, 127.5, 126.8, 126.5, 125.1, 124.1, 120.4, 118.8, 117.5, 116.6, 25.8, 25.6, 18.4, -4.2.

MS (ESI): m/z calculated for $C_{25}H_{39}N_2O_2SSi_2$ $[M+H]^+$: 487.23, Found: 487.31.

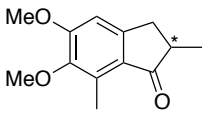

8

Compound (**8**) – 5,6-dimethoxy-2,7-dimethyl-1*H*-inden-1-one

To mechanically stirred polyphosphoric acid (370 mL) heated at 70°C, were added methacrylic acid (1.89 eq., 128 g, 127 mL, 1.49 mol) and 1,2-dimethoxy-3-methylbenzene (1 eq., 120 g, 117 mL, 788 mmol). After stirring the mixture at 70°C overnight, the solution was cooled down to 0°C, then slowly heated to room temperature and stirred overnight. The next day, the reaction mixture was poured onto ice (400 mL) and stirred overnight. The mixture was intensively extracted with ethyl acetate (5 x 200 mL). The combined organic layers were washed with aqueous $NaHCO_3$ (2 x 200 mL), water (200 mL) and brine (200 mL) then dried over sodium sulphate. The solution was concentrated under reduced pressure to a damp solid which was then recrystallized from n-heptane(100 mL) affording compound **8** (102 g, 463 mmol, 59%) as a brown crystals.

^{1}H NMR ($CDCl_3$, 400 MHz, 25°C) δ = 6.75 (s, 1H), 3.91 (s, 3H), 3.77 (s, 3H), 3.27-3.22 (m, 1H), 2.67-2.53 (m, 2H), 2.50 (s, 3H), 1.27 (d, J = 7.1 Hz, 3H).

^{13}C NMR ($CDCl_3$, 100 MHz, 25°C) δ = 208.8, 158.0, 151.9, 146.9, 132.6, 127.4, 105.9, 60.1, 55.9, 42.2, 34.5, 16.7, 10.8.

HRMS: m/z calculated for $C_{13}H_{17}LiO_3$ $[M+Li]^+$: 227.125, Found: 227.125.

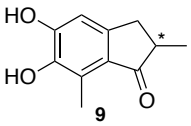

9

Compound (**9**) – 5,6-dihydroxy-2,7-dimethyl-1*H*-inden-1-one

To a solution of compound **8** (1 eq., 35.0 g, 158 mmol) in dichloromethane (250 mL) at 0°C under an argon atmosphere was slowly added boron tribromide (2.06 eq., 82 g, 30.9 mL, 327 mmol). The mixture was stirred while allowed to reach room temperature. After 24h, the reaction was quenched by adding methanol dropwise at -75°C. The solvent was then evaporated under reduced pressure to afford compound **9** (29.9 g, 155.7 mmol, 98%) as a deep blue solid that was used without further purification.

***R*$_f$** = 0.5 (cyclohexane:EtOAc = 1:1).

^{1}H NMR (CD_3OD, 400 MHz, 25°C) δ = 6.67 (s, 1H), 3.20-3.15 (m, 1H), 2.63-2.52 (m, 2H), 2.48 (s, 3H), 1.21 (d, J = 7.1 Hz, 3H).

^{13}C NMR (CD_3OD, 100 MHz, 25°C) δ = 212.3, 153.4, 150.1, 144.3, 126.9, 125.5, 109.7, 43.8, 34.7, 17.5, 10.9.

HRMS: m/z calculated for $C_{11}H_{12}LiO_3$ $[M+Li]^+$: 199.094, Found: 199.094.

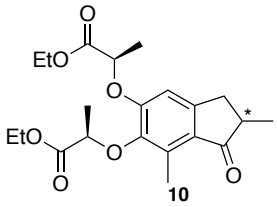

Compound (**10**) – bis-protected Indenone

To a solution of compound **9** (1 eq., 25.0 g, 130 mmol)), lactic ethyl ester (2.74 eq., 42.0 g, 40.8 mL, 355 mmol)) and triphenylphosphine (2.7 eq., 93.3 g, 355 mmol) in dry THF (750 mL) was added diisopropyl azodicarboxylate (2.8 eq., 77.1 g, 75.6 mL, 358 mmol) dropwise at 0°C under an argon atmosphere. The mixture was then stirred at room temperature for 16 hours. The solvent was removed under reduced pressure, the crude product was dissolved into ethyl acetate (200 mL), the precipitate was removed by filtration. After a second evaporation the crude product was dissolved again in a 1:4 mixture of ethyl acetate:cyclohexane (250 mL). The precipitate formed was removed one more time by filtration. After concentration under reduced pressure, the residue was then purified by flash column chromatography (silica gel, cyclohexane --> cyclohexane:EtOAc = 5:1) affording a diastereomeric mixture of compound **10** (20.42 g, 52.03 mmol, 40%) as a slight yellow oil.

^{1}H NMR ($(CD_3)_2CO$, 400 MHz, 25°C) δ = 6.85 (s, 1H), 5.14 (q, *J* = 7.0 Hz, 1H), 4.96 (q, *J* = 7.0 Hz, 1H), 4.20-4.10 (m, 4H), 3.25-3.17 (m, 1H), 2.65-2.59 (m, 1H), 2.56 (s, 3H), 2.53-2.50 (m, 1H), 1.67 (d, *J* = 7.0 Hz, 3H), 1.55 (d, *J* = 7.0 Hz, 3H), 1.23 (t, *J* = 7.0 Hz, 3H), 1.20 (t, *J* = 7.0 Hz, 3H), 1.15 (d, *J* = 7.3 Hz, 3H).

^{13}C NMR ($(CD_3)_2CO$, 100 MHz, 25°C) δ = 208.7, 172.9, 171.9, 154.7, 152.0, 146.4, 133.2, 128.1, 108.2, 77.8, 73.1, 62.1, 61.3, 43.6, 35.0, 22.3, 19.2, 18.7, 16.7, 14.9, 11.6.

HRMS: m/z calculated for $C_{21}H_{28}LiO_7$ $[M+Li]^+$: 399.199, Found: 399.199.

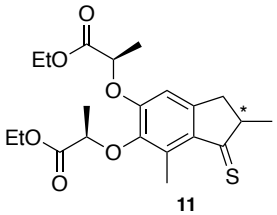

Compound (**11**) – Thioketone

A solution of compound **10** (1 eq., 16.0 g, 40.8 mmol) and phosphorous pentasulfide (3.13 eq., 28.4 g, 127 mmol) in toluene (150 mL) was heated at 80°C for 1 hour under an argon atmosphere. After cooling down to room temperature, the reaction mixture was filtered and washed with ethyl acetate (200 mL) until the eluent was colourless. Flash column chromatography (silica gel, EtOAc:cyclohexane = 1:13) afforded compound **11** (8.0 g, 19.6 mmol, 48 %) as a purple oil. As the product is not stable, it was prepared just before use in the next step.

^{1}H NMR ($CDCl_3$, 400 MHz, 25°C) δ = 6.61 (s, 1H), 4.88 (q, *J* = 6.8 Hz, 1H), 4.82 (q, *J* = 6.8 Hz, 1H), 4.26-4.18 (m, 4H), 3.33-3.26 (m, 1H), 3.00-2.96 (m, 1H), 2.77 (s, 3H), 2.71-2.66 (m, 1H), 1.69 (d, *J* = 6.8 Hz, 3H), 1.62 (d, *J* = 6.8 Hz, 3H), 1.39 (d, *J* = 7.2 Hz, 3H), 1.25 (t, *J* = 6.8 Hz, 6H).
^{13}C NMR ($CDCl_3$, 100 MHz, 25°C) δ = 248.7, 172.1, 171.0, 154.6, 152.8, 145.2, 138.1, 135.1, 106.1, 77.2, 72.6, 60.9, 55.5, 43.4, 38.9, 21.6, 21.5, 18.6, 18.2, 14.0, 13.8.
MS (ESI): m/z calculated for $C_{21}H_{29}O_6S$ $[M+H]^+$: 409.17, Found: 409.28.

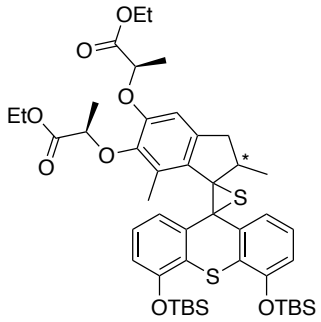

12

Compound (**12**) – (*R*) & (*S*) bis-ester bis-TBS Episulfide

In a dry Schlenk flask covered with aluminium foil to protect it from light, sodium sulphate (10 eq., 24.8 g, 174 mmol) and compound **7** (1.21 eq., 10.2 g, 21 mmol) were solubilised in dry THF (50 mL) under an argon atmosphere. The solution was cooled down to 0°C and Manganese dioxide (10 eq., 15.2 g, 174 mmol) was then added. The reaction mixture was stirred for 40 min while allowed to reach room temperature. A solution of compound **11** (1 eq., 7.1 g, 17.4 mmol) in dry THF (50 mL) was prepared under an argon atmosphere. The solution containing compound **7** was then added slowly through a cannula to the solution of thioketone **11** at room temperature. The flask containing compound **7** was washed with dry THF (2 x 10 mL) and the solution added over thioketone **11**. The mixture was stirred overnight. After concentration under reduced pressure, the crude residue was purified using column chromatography (silica gel, toluene:EtOAc = 100:0 --> 50:1) to afford compound **12** (9.53 g, 11.0 mmol, 63%) as a yellowish oil.
R,R,R-isomer ***12***
R_f = 0.7 (toluene:EtOAc = 6:1).
^{1}H NMR ($CDCl_3$, 400 MHz, 25°C) δ = 7.39 (dd, *J* = 8.0, 0.8 Hz, 1H), 7.24 (dd, *J* = 7.6, 1.2 Hz, 1H), 7.10 (dd, *J* = 8.0, 8.0 Hz, 1H), 7.01 (dd, *J* = 8.0, 8.0 Hz, 1H), 6.73 (dd, *J* = 8.0, 1.2 Hz, 1H), 6.60 (dd, *J* = 8.0, 1.2 Hz, 1H), 6.35 (s, 1H), 4.61 (q, *J* = 6.8 Hz, 1H), 4.22-4.15 (m, 5H), 3.22-3.17 (m, 1H), 2.16 (s, 3H), 2.07 (d, *J* = 14.8 Hz, 1H), 1.52 (d, *J* = 6.8 Hz, 3H), 1.42 (d, *J* = 6.8 Hz, 3H), 1.35-1.32 (m, 1H), 1.31 (t, *J* = 6.8 Hz, 3H), 1.23 (t, *J* = 7.2 Hz, 3H), 1.05 (s, 9H), 0.98 (s, 9H), 0.92 (d, *J* = 6.8 Hz, 3H), 0.26 (s, 3H), 0.24 (s, 3H), 0.09 (s, 3H), -0.07 (s, 3H).
^{13}C NMR ($CDCl_3$, 100 MHz, 25°C) δ = 172.5, 171.9, 151.6, 151.5, 149.7, 144.7, 140.3, 139.9, 136.1, 131.6, 128.9, 127.9, 127.8, 126.2, 125.5, 123.5, 121.7, 117.5, 116.9, 108.9, 77.5, 77.2,

73.2, 71.6, 61.9, 60.9, 60.6, 41.1, 37.7, 25.9, 25.8, 21.1, 18.9, 18.4, 18.3, 18.2, 14.2, 14.1, 12.4, -3.9, -4.2, -4.3, -4.7.

MS (ESI): m/z calculated for $C_{46}H_{65}O_8S_2Si_2$ $[M+H]^+$: 865.37, Found: 865.46.

R,R,S-isomer ***12***

R_f = 0.65 (toluene:EtOAc = 6:1).

^{1}H NMR ($CDCl_3$, 400 MHz, 25°C) δ = 7.38 (dd, *J* = 8.0, 1.2 Hz, 1H), 7.24 (dd, *J* = 8.0, 1.2 Hz, 1H), 7.09 (dd, *J* = 8.0, 8.0 Hz, 1H), 7.00 (dd, *J* = 8.0, 8.0 Hz, 1H), 6.73 (dd, *J* = 8.0, 1.2 Hz, 1H), 6.59 (dd, *J* = 8.0, 1.2 Hz, 1H), 6.26 (s, 1H), 4.59 (q, *J* = 6.8 Hz, 2H), 4.22-4.12 (m, 4H), 3.23-3.18 (m, 1H), 2.13 (s, 3H), 2.04 (d, *J* = 14.8 Hz, 1H), 1.52 (d, *J* = 6.8 Hz, 3H), 1.35-1.32 (m, 1H), 1.28 (d, *J* = 6.8 Hz, 3H), 1.24 (t, *J* = 6.8 Hz, 3H), 1.18 (t, *J* = 7.2 Hz, 3H), 1.06 (s, 9H), 0.95 (s, 9H), 0.92 (d, *J* = 7.2 Hz, 3H), 0.26 (s, 3H), 0.24 (s, 3H), 0.07 (s, 3H), -0.09 (s, 3H).

^{13}C NMR ($CDCl_3$, 100 MHz, 25°C) δ = 172.7, 171.9, 151.5, 151.4, 149.1, 143.8, 140.0, 139.7, 136.1, 131.5, 128.8, 127.9, 126.2, 125.5, 123.6, 121.7, 117.5, 116.9, 107.8, 77.2, 76.5, 72.5, 71.4, 61.7, 61.1, 60.6, 40.9, 37.6, 25.9, 25.8, 21.1, 18.6, 18.4, 18.3, 18.2, 14.1, 14.0, 12.4, -4.0, -4.2, -4.3, -4.8.

HRMS: m/z calculated for $C_{46}H_{64}O_8LiS_2Si_2$ $[M+Li]^+$: 871.374, Found: 871.374.

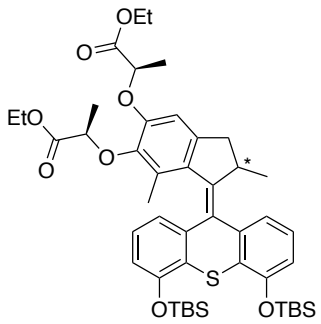

13

Compound (**13**) – (*R*) & (*S*) bis-ester bis-TBS Motor

Compound **12** (1 eq., 1.0 g, 1.16 mmol) was dissolved in toluene (40 mL) and then triphenylphosphine (15.03 eq., 4.56 g, 17.37 mmol) was added. The reaction mixture was stirred at reflux for 24 hours. After cooling down to room temperature, the crude was concentrated under reduced pressure and the residue purified by flash column chromatography (silica gel, toluene --> toluene:EtOAc = 80:1) affording compound **13** (866.7 mg, 1.04 mmol, 90%) as a yellow solid.

R,R,S-isomer ***13***

R_f = 0.63 (toluene:EtOAc = 6:1).

^{1}H NMR ($CDCl_3$, 400 MHz, 25°C) δ = 7.29 (d, *J* = 7.2 Hz, 1H), 7.13 (dd, *J* = 8.0 Hz, 1H), 6.86 (dd, *J* = 8.0 Hz, 1H), 6.69 (dd, *J* = 8.0, 1.2 Hz, 1H), 6.64 (dd, *J* = 7.6, 1.2 Hz, 1H), 6.63 (dd, *J* = 7.6, 1.2 Hz, 1H), 6.54 (s, 1H), 4.78- 4.72 (m, 2H), 4.27-4.09 (m, 5H), 3.38-3.31 (m, 1H), 2.32 (d, *J* = 15.2 Hz, 1H), 1.61 (d, *J* = 6.8 Hz, 3H), 1.44 (d, *J* = 6.8 Hz, 3H), 1.22 (t, *J* = 7.2 Hz, 3H), 1.21 (t, *J* = 7.2

Hz, 3H), 1.21 (s, 3H), 1.09 (s, 9H), 1.08 (s, 9H), 0.62 (d, *J* = 6.8 Hz, 3H), 0.29 (s, 3H), 0.27 (s, 6H), 0.25 (s, 3H).

^{13}C NMR ($CDCl_3$, 100 MHz, 25°C) δ = 172.4, 171.9, 152.7, 152.2, 149.6, 145.5, 144.4, 141.9, 141.8, 138.3, 133.4, 130.8, 128.1, 127.7, 127.1, 126.4, 126.1, 120.9, 120.2, 116.3, 115.5, 108.1, 76.9, 72.9, 61.2, 60.6, 39.4, 37.9, 25.9, 18.9, 18.5, 18.4, 14.4, 14.1, 14.0, -3.9, -4.0, -4.3, -4.4.

MS (ESI): m/z calculated for $C_{46}H_{65}O_8SSi_2$ $[M+H]^+$: 833.39 Found: 833.58.

R,R,R-isomer ***13***

R_f = 0.68 (toluene:EtOAc = 6:1).

^{1}H NMR ($CDCl_3$, 400 MHz, 25°C) δ = d 7.28 (d, *J* = 7.2 Hz, 1H), 7.12 (dd, *J* = 8.0, 8.0 Hz, 1H), 6.88 (dd, *J* = 8.0, 8.0 Hz, 1H), 6.68 (dd, *J* = 8.0, 0.8 Hz,1H), 6.65 (dd, *J* = 7.6, 1.2 Hz, 2H), 6.56 (s, 1H), 4.77 (q, *J* = 6.8 Hz, 1H), 4.44 (q, *J* = 6.8 Hz, 1H), 4.28-4.16 (m, 4H), 4.11-4.08 (m, 1H), 3.35-3.29 (m, 1H), 2.32 (d, *J* = 14.8 Hz, 1H), 1.62 (d, *J* = 6.4 Hz, 3H), 1.51 (d, *J* = 6.8 Hz, 3H), 1.28 (t, *J* = 7.2 Hz, 3H), 1.27 (t, *J* = 7.2 Hz, 3H), 1.19 (s, 3H), 1.09 (s, 9H), 1.08 (s, 9H), 0.61 (d, *J* = 6.8 Hz, 3H), 0.29 (s, 3H), 0.28 (s, 3H), 0.27 (s, 3H), 0.25 (s, 3H).

^{13}C NMR ($CDCl_3$, 100 MHz, 25°C) δ = 172.4, 172.2, 152.7, 152.2, 150.2, 145.4, 144.9, 142.3, 141.8, 138.4, 133.5, 130.9, 128.2, 127.6, 127.2, 126.5, 126.1, 121.0, 120.3, 116.3, 115.5, 108.2, 77.4, 73.0, 61.2, 60.7, 39.5, 38.0, 25.9 (6C), 18.9, 18.7, 18.5, 18.4 (2C), 14.4, 14.2, 14.1, -3.9, -4.0, -4.3, -4.4

MS (ESI): m/z calculated for $C_{46}H_{65}O_8SSi_2$ $[M+H]^+$: 833.39 Found: 833.58

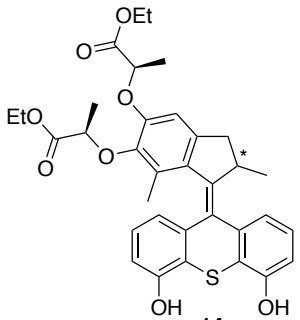

14

Compound (**14**) – (*R*) & (*S*) bis-ester bis-phenol Motor

A solution of compound **13** (1 eq., 225 mg, 0.27 mmol) was solubilized in THF (10 mL) under an argon atmosphere and cooled down to 0°C before adding tetrabutylammonium fluoride (2.06 eq., 0.56 mL, 0.56 mmol) dropwise and then stirred for 10 min. The reaction mixture was quenched by the addition of a saturated solution of NH_4Cl (10 mL). Dichloromethane (20 mL) was added and the resulting organic phase was washed with water (10 mL) and brine (10 mL), dried over sodium sulphate and evaporated under reduced pressure. The crude residue was purified by chromatography column (silica gel, CH_2Cl_2:MeOH = 100:1 --> 100:5) to afford compound **14** (161.7 mg, 0.27 mmol, 99%) as a yellowish solid.

R,R,S-isomer ***14***

R_f = 0.2 (CH_2Cl_2:MeOH = 20:1).

^{1}H NMR (CD_3OD, 400 MHz, 25°C) δ = 7.24 (d, *J* = 7.2 Hz, 1H), 7.15 (dd, *J* = 8.0, 8.0 Hz, 1H), 6.86 (dd, *J* = 8.0, 8.0 Hz, 1H), 6.72 (dd, *J* = 8.0, 1.2 Hz, 1H), 6.66 (dd, *J* = 8.0, 1.0 Hz, 1H), 6.64 (s, 1H), 6.64 (dd, *J* = 7.6, 0.8 Hz, 1H), 4.86 (q, *J* = 6.8 Hz, 1H), 4.78 (q, *J* = 6.8 Hz, 1H), 4.22-4.09 (m, 5H), 3.40-3.35 (m, 1H), 2.35 (d, *J* = 14.8 Hz, 1H), 1.57 (d, *J* = 6.8 Hz, 3H), 1.38 (d, *J* = 6.8 Hz, 3H), 1.23 (t, *J* = 6.8 Hz, 3H), 1.20 (t, *J* = 6.8 Hz, 3H), 1.20 (s, 3H), 0.62 (d, *J* = 6.4 Hz, 3H).
^{13}C NMR (CD_3OD, 100 MHz, 25°C) δ = 174.2, 173.5, 155.7, 155.2, 151.1, 146.5, 145.5, 143.8, 143.5, 140.2, 134.7, 131.9, 130.2, 127.9, 127.8, 124.0, 123.3, 120.5, 120.0, 113.2, 113.1, 109.4, 77.9, 74.1, 62.4, 62.0, 40.4, 39.3, 19.3, 18.9, 18.7, 15.0, 14.5, 14.4.
HRMS: m/z calculated for $C_{34}H_{36}LiO_8S$ $[M+Li]^+$: 611.229, Found: 611.228.
R,R,R-isomer ***14***
R_f = 0.2 (CH_2Cl_2:MeOH = 20:1).
^{1}H NMR (CD_3OD, 400 MHz, 25°C) δ = 7.30 (d, *J* = 7.2 Hz, 1H), 7.22 (dd, *J* = 8.0, 8.0 Hz, 1H), 6.98 (dd, *J* = 8.0, 8.0 Hz, 1H), 6.82 (dd, *J* = 8.0, 1.2 Hz, 1H), 6.75 (dd, *J* = 8.0, 1.0 Hz, 1H), 6.67 (s, 1H), 6.59 (dd, *J* = 7.6, 0.8 Hz, 1H), 4.86 (q, *J* = 6.8 Hz, 1H), 4.78 (q, *J* = 6.8 Hz, 1H), 4.22-4.09 (m, 5H), 3.40-3.35 (m, 1H), 2.35 (d, *J* = 14.8 Hz, 1H), 1.57 (d, *J* = 6.8 Hz, 3H), 1.38 (d, *J* = 6.8 Hz, 3H), 1.23 (t, *J* = 6.8 Hz, 3H), 1.20 (t, *J* = 6.8 Hz, 3H), 1.20 (s, 3H), 0.62 (d, *J* = 6.4 Hz, 3H).
^{13}C NMR (CD_3OD, 100 MHz, 25°C) δ = 174.2, 173.5, 155.7, 155.2, 151.1, 146.5, 145.5, 143.8, 143.5, 140.2, 134.7, 131.9, 130.2, 127.9, 127.8, 124.0, 123.3, 120.5, 120.0, 113.2, 113.1, 109.4, 77.9, 74.1, 62.4, 62.0, 40.4, 39.3, 19.3, 18.9, 18.7, 15.0, 14.5, 14.4.
HRMS: m/z calculated for $C_{34}H_{36}LiO_8S$ $[M+Li]^+$: 611.229, Found: 611.228.

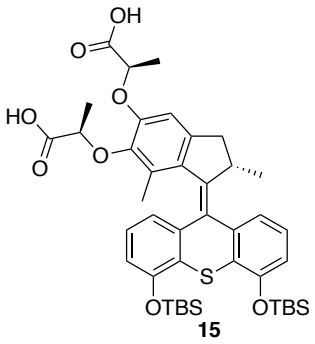

15

Compound (**15**) – (*S*) bis-acid bis-TBS Motor

Compound **13** (1 eq., 100 mg, 0.12 mmol) and trimethyltin hydroxide (4.903 eq., 107 mg, 0.59 mmol) were dispersed in dichloroethane (2 mL). The solution mixture was then placed in a microwave and heated to 100°C (300 W, fixed power) for 5 hours. The solvent was removed under reduced pressure and the residue was diluted with ethyl acetate (20 mL). The organic phase was washed with water (5 x 20 mL) to remove tin, dried over sodium sulphate and evaporated under reduced pressure providing compound **15** (92 mg, 0.12 mmol, 99%) as a slight grey solid.
R_f = 0.13 (CH_2Cl_2:MeOH = 10:1).

^{1}H NMR (CD_3OD, 400 MHz, 25°C) δ = 7.37 (d, *J* = 7.2 Hz, 1H), 7.22 (dd, *J* = 8.0, 8.0 Hz, 1H), 6.95 (dd, *J* = 8.0, 8.0 Hz, 1H), 6.78 (dd, *J* = 8.0, 0.8 Hz, 1H), 6.73 (dd, *J* = 8.0, 1.2 Hz, 1H), 6.65 (s, 1H), 6.63 (dd, *J* = 7.6, 1.2 Hz, 1H), 4.83 (q = 6.8 Hz, 1H), 4.68 (q, *J* = 6.8 Hz, 1H), 4.15-4.08 (m, 1H), 3.35-3.32 (m, 1H), 2.38 (d, *J* = 14.8 Hz, 1H), 1.56 (d, *J* = 6.4 Hz, 3H), 1.48 (d, *J* = 6.8 Hz, 3H), 1.19 (s, 3H), 1.12 (s, 18H), 0.63 (d, *J* = 6.4 Hz, 3H), 0.30 (s, 12H).
^{13}C NMR (CD_3OD, 100 MHz, 25°C) δ = 178.5, 154.1, 153.5, 152.5, 147.1, 146.1, 143.5, 143.4, 139.9, 133.7, 131.5, 129.3, 129.0, 128.2, 127.8, 127.6, 122.3, 121.7, 117.8, 117.1, 109.4, 79.4, 75.4, 40.4, 39.2, 26.6, 19.7, 19.4, 19.3, 19.2, 15.2, -3.5, -3.7, -3.8, -4.0.
MS (ESI): m/z calculated for $C_{42}H_{57}O_8SSi_2$ $[M+H]^+$: 777.33, Found: 776.32.

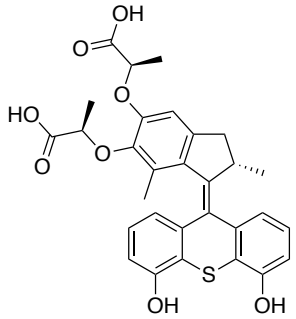

16

Compound (**16**) – (*S*) bis-acid bis-phenol Motor

To a solution of compound **15** (100 mg, 0.127 mmol) in THF (5 mL) was added tetrabutylammonium fluoride (1 M in THF, 0.45 mL, 0.45 mmol) at 0°C. The mixture was stirred at this temperature for 5 min. A saturated solution of NH_4Cl (7 mL) was then added and the mixture was extracted with a 3:1 mixture of dichloromethane:methanol (3 × 10 mL). The combined organic layer was dried over sodium sulphate and concentrated under reduced pressure. The crude residue was purified by flash column chromatography (silica gel, CH_2Cl_2:MeOH = 50:1 --> MeOH) affording compound **16** (35 mg, 64.5 µmol, 48 % yield) as a yellow solid.
***R*$_f$** = 0.7 (MeOH).
^{1}H NMR (CD_3OD, 400 MHz, 25°C) δ = 7.25 (d, *J* = 8.0 Hz, 1H), 7.16 (dd, *J* = 8.0, 8.0 Hz, 1H), 6.93 (dd, *J* = 8.0, 8.0 Hz, 1H), 6.81 (s, 1H), 6.74 (dd, *J* = 8.0, 1.0 Hz, 1H), 6.64 (d, *J* = 8.0 Hz, 1H), 6.51 (d, *J* = 8.0 Hz, 1H), 4.63 (q, *J* = 6.8 Hz, 1H), 4.57 (q, *J* = 6.8 Hz, 1H), 4.20-4.15 (m, 1H), 3.45-3.88 (m, 1H), 2.37 (d, *J* = 15.2 Hz, 1H), 1.51 (d, *J* = 6.8 Hz, 3H), 1.35 (d, *J* = 6.8 Hz, 3H), 1.26 (d, *J* = 6.8 Hz, 3H), 0.59 (d, *J* = 6.8 Hz, 3H).
^{13}C NMR (CD_3OD, 100 MHz, 25°C) δ = 176.6, 155.9, 155.2, 151.4, 146.5, 145.6, 144.0, 143.8, 140.2, 134.8, 132.2, 130.3, 128.0, 124.1, 123.3, 120.6, 120.4, 113.3, 113.2, 109.6, 109.4, 78.6, 74.2, 40.5, 39.3, 30.9, 19.3, 19.1, 18.8, 15.3.
MS (ESI): m/z calculated for $C_{30}H_{29}O_8S$ $[M+H]^+$: 549.16, Found: 549.31.

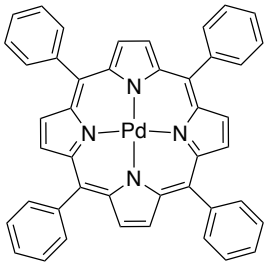

17

Compound (**17**) – Pd-Tetraphenylporphyrin

To a solution of tetraphenylporphyrin (1 eq., 50.0 mg, 81 µmol) in dichloromethane (20 mL) was added palladium acetate (45 eq., 823 mg, 3.66 mmol). The mixture was stirred at reflux overnight. After cooling down to room temperature, the solution was filtered and concentrated under reduced pressure. The crude residue was purified by column chromatography (silica gel, cyclohexane: CH_2Cl_2 = 1:1) affording compound **17** (40 mg, 56 µmol, 68%) as a red solid.

^{1}H NMR (400 MHz, $CDCl_3$, 25°C) δ = 8.74 (s, 8H), 8.16-8.10 (m, 8H), 7.76-7.68 (m, 12H).

^{13}C NMR (100 MHz, $CDCl_3$, 25°C) δ = 148.8, 141.8, 141.1, 131.2, 129.4, 123.0, 121.1, 35.2, 31.9.

NMR data corresponds to what is described in the literature.[167]

MS (ESI): m/z calculated for $C_{44}H_{28}N_4Pd$ $[M+H]^+$: 719.13, Found 718.62.

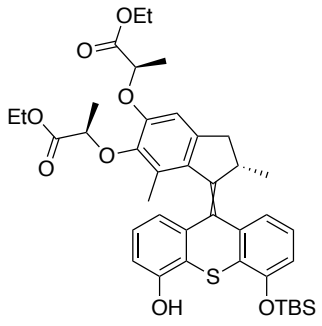

18

Compound (**18**) – (*S*) E/Z bis-ester mono-phenol mono-TBS asymmetric Motor

To a solution of compound **14** (182 mg, 0.301 mmol) in dry THF (20 mL) at 0°C under an argon atmosphere were added imidazole (28.69 mg, 0.42 mmol) and *tert*-butyldimethylsilyl chloride (63.5 mg, 73.5 µL, 0.42 mmol). The solution was allowed to each room temperature and was stirred for 6 hours. The reaction mixture was then filtered, washed with THF (20 mL) and concentrated under reduced pressure. The crude residue was purified by column chromatography (silica gel, cyclohexane:EtOAc = 4:1 --> 1:1) affording compound **18** (35 mg, 49.6 µmol, 16% yield) as a yellow solid. The compound was then further purified by preparative HPLC reverse phase columns (Waters, Xbridge Prep C_{18} 5.0 µm, 19 × 150 mm) running with a 0.05% NH3 water/methanol gradient as eluent, t_{R1} = 30.17 min, t_{R2} = 30.87 min.) in order to separate E and Z isomers.

N.B.:

The E and Z isomers could not be assigned as even ^{1}H NOESY NMR could not differentiate them, so they will be referred to as isomer 1 and 2.

Isomer 1

t_{R1} = 30.17 min.

^{1}H NMR ($CDCl_3$, 400 MHz, 25°C) δ = 7.29 (m, *J* = 7.2 Hz, 1H), 7.2 (dd, *J* = 8.0, 8.0 Hz, 1H), 6.94 (dd, *J* = 8.0, 8.0 Hz, 1H), 6.83 (dd, *J* = 8.0, 1.2 Hz, 1H), 6.7 (dd, *J* = 8.0, 1.0 Hz, 1H), 6.66 (dd, *J* = 7.6, 0.8 Hz, 1H), 6.58 (s, 1H), 5.25 (s, 1H), 4.78 (q, *J* = 6.4 Hz, 1H), 4.5 (q, *J* = 6.8 Hz, 1H), 4.29-4.12 (m, 4H), 4.08 (t, *J* = 6.6 Hz, 1H), 3.38-3.31 (dd, *J* = 16.0 Hz, 8.0 Hz, 1H), 2.37 (d, *J* = 16 Hz, 1H), 1.53 (d, *J* = 6.8 Hz, 3H), 1.52 (d, *J* = 6.8 Hz, 3H), 1.31-1.24 (m, 10H), 1.10 (s, 8H), 0.69 (d, *J* = 6.4 Hz, 3H), 0.26 (s, 3H), 0.24 (s, 3H).

MS (ESI): m/z calculated for $C_{40}H_{50}O_8SSi$ $[M+H]^+$: 719.30, Found 719.78.

Isomer 2

t_{R2} = 30.87 min.

^{1}H NMR ($CDCl_3$, 400 MHz, 25°C) δ = 7.34-7.30 (m, 1H), 7.16 (dd, *J* = 7.9, 7.9 Hz, 1H), 6.97 (dd, *J* = 8.0 Hz, 1H), 6.76 (dd, *J* = 8.0, 1.2 Hz, 1H), 6.71 (dd, *J* = 8.0, 1.2 Hz, 1H), 6.65 (dd, *J* = 7.6, 1.2 Hz, 1H), 6.58 (s, 1H), 5.33 (s, 1H), 4.78 (q, *J* = 6.7 Hz, 1H), 4.50 (dd, *J* = 9.4, 6.8 Hz, 1H), 4.29-4.15 (m, 4H), 4.07 (t, *J* = 6.6 Hz, 1H), 3.34 (dd, *J* = 14.9 Hz, 6.3 Hz, 1H), 2.35 (d, *J* = 15 Hz, 1H), 1.63 (d, *J* = 6.8 Hz, 3H), 1.52 (d, *J* = 6.8 Hz, 3H), 1.29-1.24 (m, 10H), 1.10 (s, 8H), 0.65 (d, *J* = 6.4 Hz, 3H), 0.29 (s, 3H), 0.27 (s, 3H).

MS (ESI): m/z calculated for $C_{40}H_{50}O_8SSi$ $[M+H]^+$: 719.30, Found 719.78.

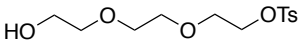

19

Compound (**19**) – tosyl TEG

Trimethylamine (1 eq., 1.57 g, 2.62 mL, 26.64 mmol) was added to a solution of triethylene glycol (1 eq., 4.0 g, 26.64 mmol) in THF (20 mL) under an argon atmosphere. The mixture was cooled down to 0°C, and then a solution of tosyl chloride (1 eq., 5.08 g, 26.64 mmol) in THF (20 mL) was added dropwise over 30 min. The reaction mixture was allowed to reach room temperature and was stirred overnight. The suspension was filtered and dried over sodium sulphate. The solvent was removed under reduced pressure. The crude residue was purified by column chromatography (silica gel, cyclohexane:EtOAc = 4:6 --> EtOAc), affording compound **19** (4.0 g, 13.1 mol, 49%) as a yellow oil.

R_f = 0.10 (cyclohexane:EtOAc = 4:6).

^{1}H NMR ($CDCl_3$, 400 MHz, 25°C) δ = 7.80 (d, *J* = 8.4 Hz, 2H), 7.34 (d, *J* = 8.4 Hz, 2H), 7.20 (t, *J* = 3.4 Hz, 2H), 3.90-3.6 (m, 10H), 2.45 (s, 3H), 1.60 (s, 1H).

^{13}C NMR ($CDCl_3$, 100 MHz, 25°C) δ = 145.4, 133.2, 130.1, 128.3, 72.7, 70.8, 70.1, 69.5, 68.9, 61.7, 21.9.

MS (ESI): m/z calculated for $C_{13}H_{20}O_6S$ $[M+H]^+$: 304.98, Found 305.02.

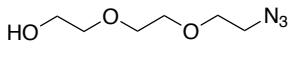

20

Compound (**20**) – azide TEG

In a dry round bottom flask, sodium azide (2.5 eq., 1.6 g, 24.6 mmol) was added to a solution of compound **19** (1 eq., 3.0 g, 9.86 mmol) in dry DMF (20 mL). The reaction mixture was heated to reflux overnight. The mixture was cooled down to room temperature, the solvent was removed under reduced pressure and the crude residue was purified by column chromatography (silica gel, cyclohexane:EtOAc = 4:6 --> 2:8), affording compound **20** (1.40 g, 7.99 mmol, 81%) as a yellow oil.

R_f = 0.17 (cyclohexane:EtOAc = 4:6).

^{1}H NMR ($CDCl_3$, 400 MHz, 25°C) δ = 3.76-3.71 (br s, 2H), 3.70-3.65 (m, 6H), 3.65-3.60 (m, 2H), 3.40 (t, J = 5.0 Hz, 2H).

^{13}C NMR ($CDCl_3$, 100 MHz, 25°C) δ = 72.4, 70.5, 70.3, 70.0, 61.7, 50.5.

MS (ESI): m/z calculated for $C_6H_{13}N_3O_3$ $[M+H]^+$: 175.10, Found 175.12.

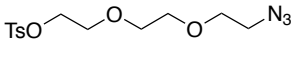

21

Compound (**21**) – tosyl, azide TEG

To a solution of compound **20** (1 eq., 0.75 g, 4.28 mmol) in dichloromethane (5 mL) was added triethylamine (2 eq., 1.2 mL, 8.64 mmol) and the solution cooled down to 0°C. Tosyl chloride (1.5 eq., 1.25 g, 6.55 mmol) was added and the mixture was then allowed to reach room temperature and was stirred overnight. The mixture reaction was diluted with dichloromethane (50 mL) and washed successively with a 3% HCl solution (30 mL) and brine (30 mL). The organic layer was dried over sodium sulphate and concentrated under reduced pressure. The crude residue was purified by column chromatography (silica gel, cyclohexane:EtOAc = 8:2 --> 7:3) affording compound **21** as a yellow oil (1.26 g, 3.82 mmol, 87% yield).

R_f = 0.4 (cyclohexane:EtOAc = 6:1).

^{1}H NMR ($CDCl_3$, 400 MHz, 25 °C) δ = 7.80 (d, J = 8.4 Hz, 2H), 7.34 (d, J = 8.4 Hz, 2H), 4.16 (t, J = 4.8 Hz, 2H), 3.70 (t, J = 4.8 Hz, 2H), 3.64 (t, J = 5.2 Hz, 2H), 3.60 (s, 4H), 3.36 (t, J = 5.2 Hz, 2H), 2.44 (s, 3H).

^{13}C NMR ($CDCl_3$, 100 MHz, 25°C) δ = 144.3, 140.2, 130.5, 130.4 , 128.4, 70.4, 70.2, 70.0, 69.1, 50.4, 50.0, 21.4.

MS (ESI): m/z calculated for $C_{13}H_{19}N_3O_5S$ $[M+H]^+$: 329.11, Found 329.12.

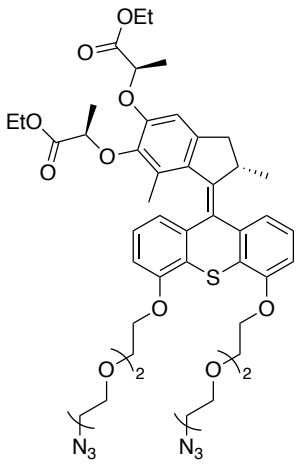

22

Compound (**22**) – (*S*) bis-ester bis-azide Motor

Compound **14** (1 eq., 85.0 mg, 0.14 mmol) and compound **21** (3.75 eq., 173.61 mg, 0.53 mmol) were dissolved in DMF (10 mL). The mixture was stirred overnight at 45°C. After cooling down to room temperature, the reaction mixture was diluted with water (10 mL) and extracted with dichloromethane (3 x 15 mL). The combined organic phases were dried over sodium sulphate and the solvent evaporated under reduced pressure. The crude residue was purified by flash column chromatography (silica gel, cyclohexane:EtOAc = 3:1 --> 1:1) affording compound **22** (99 mg, 0.11 mmol, 76%) as an orange oil.

R_f = 0.4 (cyclohexane:EtOAc = 1:1)

^{1}H NMR ($CDCl_3$, 400 MHz, 25°C) δ = 7.32 (d, *J* = 7.6 Hz, 1H), 7.21 (dd, *J* = 8.0, 8.0 Hz, 1H), 6.97 (dd, *J* =8.0, 8.0 Hz, 1H), 6.76 (d, *J* = 7.6 Hz, 1H), 6.68 (m, 2H), 6.57 (s, 1H), 4.76 (q, *J* = 6.7 Hz, 1H), 4.49 (q, *J* = 6.7 Hz, 1H) 4.34-4.06 (m, 10H), 4.00-3.93 (m, 4H), 3.87-3.82 (m, 4H), 3.76-3.66 (m, 8H), 3.38 (br t, *J* = 4.9 Hz, 3H), 3.37-3.32 (m, 1H), 2.33 (d, *J* = 14.8 Hz, 1H), 1.63 (d, *J* = 7.8 Hz, 3H), 1.50 (d, *J* = 7.8 Hz, 3H), 1.25-1.22 (m, 6H), 1.20 (s, 3H), 0.62 (d, *J* = 6.8 Hz, 3H).

^{13}C NMR ($CDCl_3$, 100 MHz, 25°C) δ = 172.6, 172.1, 155.9, 156.2, 147.73, 146.2, 143.8, 141.9, 140.9, 136.9, 133.4, 131.1, 127.7, 126.9, 126.5, 125.0, 123.7, 121.5, 120.3, 109.5, 109.1, 108.1, 73.0, 71.3, 70.9, 70.2, 69.8, 68.9, 61.3, 60.8, 50.8, 39.6, 38.2, 27.0, 19.1, 18.7, 18.5, 14.6, 14.2.

MS (ESI): m/z calculated for $C_{46}H_{58}N_6O_{12}S$ $[M+H]^+$: 918.38, Found 918.43.

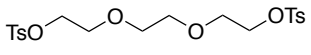

23

Compound (**23**) – bis-tosyl TEG

In a round bottom flask, tosyl chloride (3 eq., 19 g, 99.9 mmol) and triethylene glycol (1 eq., 5.0 g, 4.46 mL, 33.3 mmol) were dissolved in THF (70 mL). The solution was cooled to 0°C and a solution of potassium hydroxide (6.4 eq., 12.0 g, 213 mmol) in water (50 mL) was added dropwise trough a dropping funnel over 3 hours, while stirring. After addition, the mixture was allowed to reach room temperature and was stirred overnight. The reaction mixture was

then poured over a 70/30 mixture H_2O/CH_2Cl_2 (60 mL). The aqueous phase was extracted with dichloromethane (4 x 50 mL). The organic phases were combined and washed successively with water (2 x 50 mL) and brine (50 mL) then dried over sodium sulphate. The solvent was removed under reduced pressure affording compound **23** (12.8 g, 27.9 mmol, 84 %) as a white solid.

^{1}H NMR ($CDCl_3$, 400 MHz, 25 °C) δ = 7.78 (d, J = 8.5 Hz, 4H), 7.35 (d, J = 8.5 Hz, 4H), 4.14 (t, J = 5.0 Hz, 4H), 3.60 (t, J = 5.0 Hz, 4H), 3.45 (s, 4H), 2.44 (s, 6H).

^{13}C NMR ($CDCl_3$, 100 MHz, 25°C) δ = 145.2, 133.2, 130.1, 128.2, 71.1, 69.6, 69.0, 21.9.

MS (ESI): m/z calculated for $C_{20}H_{26}N_3O_8S_2$ $[M+H]^+$: 458.11, Found 458.20.

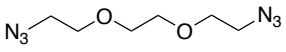

24

Compound (**24**) – bis-azide TEG

In a round-bottom flask under an argon atmosphere, compound **23** (1 eq., 2.0 g, 4.36 mmol) and sodium azide (4 eq., 1.13 g, 0.613 mL, 17.4 mmol) were dissolved in dry DMF (40 mL). The solution was heated to 65°C and stirred for 24 hours. After cooling down to room temperature, the reaction mixture was concentrated under reduced pressure. The crude residue was purified by column chromatography (silica gel, cyclohexane:EtOAc = 1:4) affording compound **24** (0.67 g, 3.35 mmol, 77%) as a colourless liquid.

R_f = 0.3 (cyclohexane:EtOAC = 1:4)

^{1}H NMR ($CDCl_3$, 400 MHz, 25 °C) δ = 3.70-3.68 (m, 8H), 3.40-3.38 (m, 4H).

^{13}C NMR ($CDCl_3$, 100 MHz, 25°C) δ = 70.9, 70.4, 50.9.

MS (ESI): m/z calculated for $C_6H_{12}N_6O_2$ $[M+H]^+$: 200.10, Found 200.30.

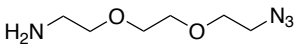

25

Compound (**25**) – amine, azide TEG

In a round-bottomed flask adapted with an addition funnel, to a solution of compound **24** (1 eq., 0.67 g, 3.35 mmol) in a mixture of ethyl acetate (11 mL) and HCl (1 M aqueous solution, 5.58 mL) was added dropwise, through an addition funnel, a solution of triphenylphosphine (1.1 eq., 0.966 g, 3.68 mmol) in ethyl acetate (10 mL). The reaction mixture was stirred overnight at room temperature. The solvent was evaporated under reduced pressure. The aqueous phase was washed with ethyl acetate (2 x 10 mL). The pH was then adjusted to 14 by adding sodium hydroxide (1M in aqueous solution, 10 mL). The aqueous solution was extracted with dichloromethane (3 x 10 mL). The combined organic phases were dried over sodium sulphate and the solvent was removed under reduced pressure affording compound **25** (0.46 g, 2.64 mmol, 79%) as a colourless oil.

^{1}H NMR ($CDCl_3$, 400 MHz, 25 °C) δ = 3.58-3.55 (m, 6H), 3.46 (t, *J* = 5.0 Hz, 2H), 3.30 (t, J = 5.0 Hz, 2H), 2.86 (br s, 2H), 2.81 (t, *J* = 7.0 Hz, 2H).
^{13}C NMR ($CDCl_3$, 100 MHz, 25°C) δ = 72.6, 70.7, 70.4, 70.2, 50.9, 41.5.
MS (ESI): m/z calculated for $C_6H_{14}N_4O_2$ $[M+H]^+$: 174.11, Found 174.35.

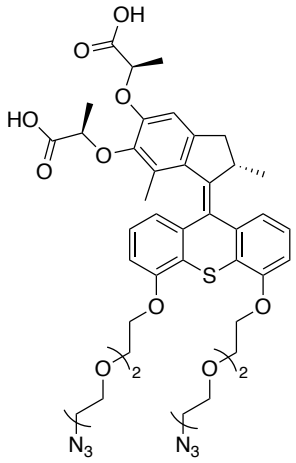

26

Compound (**26**) – (*S*) bis-acid bis-azide Motor

Compound **22** (1 eq., 98.9 mg, 0.108 mmol) and sodium hydroxide (5 eq., 21.52 mg, 0.54 mmol) were dissolved in 1/1/1 mixture of water/THF/methanol (5 mL). The solution was stirred overnight at 40°C . The reaction mixture was then cooled down to room temperature and acidified with HCl (2M aqueous solution, 1 mL). The aqueous phase was then extracted with dichloromethane (5 x 10 mL). The combined organic phases were dried over sodium sulphate and the solvent evaporated under reduced pressure affording compound **26** (85 mg, 98 µmol, 91%) as a green solid.
^{1}H NMR ($CDCl_3$, 400 MHz, 25°C) δ = 7.34 (d, *J* = 7.8 Hz, 1H), 7.23 (dd, *J* = 8.0, 8.0 Hz, 1H), 6.95 (dd, *J* =8.0, 8.0 Hz, 1H), 6.72 (d, *J* = 7.7 Hz, 1H), 6.72 (dd, *J* = 7.5, 1.0 Hz, 1H), 6.69 (s, 1H), 6.57 (dd, *J* = 7.5, 1.0 Hz, 1H), 4.89-4.78 (m, 1H), 4.53-4.48 (m, 1H), 4.34-4.25 (m, 2H), 4.25-4.08 (m, 3H), 4.03-3.90 (m, 4H), 3.89-3.79 (m, 4H), 3.78-3.67 (m, 8H), 3.63 (s, 1H), 3.38 (t, *J* = 5.5 Hz, 3H), 3.35-3.30 (m, 1H), 2.39 (d, *J* = 15.8 Hz, 1H), 1.65 (d, *J* = 7.0 Hz, 3H), 1.43 (d, *J* = 7.0 Hz, 3H), 1.25 (s, 3H), 0.64 (d, *J* = 6.7 Hz, 3H).
^{13}C NMR ($CDCl_3$, 100 MHz, 25°C) δ = 175.5, 175.3, 156.4, 153.5, 145.6, 145.2, 142.6, 141.5, 137.9, 131.1, 130.9, 128.7, 123.8, 126.7, 124.8, 124.5, 120.9, 120.3, 110.5, 109.8, 108.8, 71.3, 71.0, 70.9, 70.2, 69.9, 69.1, 68.9, 50.9, 39.7, 38.2, 32.1, 29.8, 22.8, 19.0, 18.5, 18.2, 15.2, 14.3.
HRMS: m/z calculated for $C_{42}H_{50}N_6O_{12}S$ $[M+Na]^+$: 885.311, Found: 885.312.

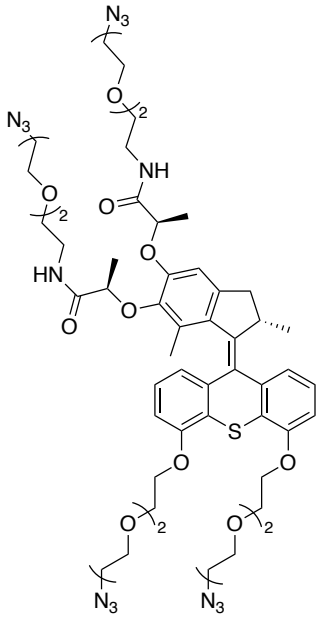

27

Compound (**27**) – (*S*) tetra-azide Motor

To a solution of compound **26** (1 eq., 30.0 mg, 0.0348 mmol) in dry dichloromethane (2.5 mL) was added EDC.HCl (6 eq., 40.1 mg, 0.201 mmol) and HOBt (2.29 eq., 10.7 mg, 0.080 mmol) at room temperature. After stirring for 30 min, compound **25** (2.27 eq., 17.2 mg, 0.079 mmol) in dichloromethane (2.5 mL) was added and the mixture was stirred overnight at room temperature. The reaction mixture was then diluted in water (10 mL) and extracted with dichloromethane (3 x 20 mL). The combined organic phases were dried over sodium sulphate. The solvent was removed under reduced pressure and the crude residue was purified by flash column chromatography (silica gel, CH_2Cl_2:MeOH = 100:1 --> 10:1) affording compound **27** (43 mg, 33.2 µmol, 82 %) as a green oil.

R_f = 0.21 (CH_2Cl_2:MeOH = 20:1).

^{1}H NMR ($CDCl_3$, 400 MHz, 25°C): δ = 7.12-7.05 (m, 2H), 7.03 (dd, *J* = 7.7, 2.2 Hz, 2H), 6.95 (dd, *J* = 7.1, 2.2 Hz, 2H), 6.69 (d, *J* = 0.9 Hz, 1H), 4.97-4.93 (m, 4H), 4.87 (q, *J* = 6.6 Hz, 2H), 4.20 (t, *J* = 4.9 Hz, 4H), 3.82 (t, *J* = 4.9 Hz, 4H), 3.76 (t, *J* = 5.1 Hz, 4H), 3.71-3.66 (m, 8H), 3.64-3.62 (m, 16H), 2.70-2.63 (m, 2H), 2.51 (s, 3H), 2.43-2.38 (m, 1H), 1.75 (s, 3H), 1.72 (s, 3H), 1.52-1.46 (m, 8H), 1.16-1.14 (m, 3H).

^{13}C NMR ($CDCl_3$, 100 MHz, 25°C): δ = 172.5, 172.1, 156.0, 155.4, 149.8, 145.5, 143.6, 142.9, 141.6, 137.9, 134.1, 130.9, 128.3, 126.7, 126.7, 124.9, 124.3, 120.9, 120.2, 109.6, 109.2, 109.1, 79.0, 76.1, 71.2, 70.8, 70.8, 70.7, 70.7, 70.6, 70.5, 70.5, 70.5, 70.3, 70.2, 70.1, 70.0, 69.8, 69.9, 68.9, 68.8, 50.7, 50.7, 39.7, 38.9, 38.0, 29.7, 19.1, 18.9, 15.2.

MS (ESI): m/z calculated for $C_{54}H_{72}N_{12}O_{16}S$ $[M+H]^+$: 1176.49, Found: 1176.50.

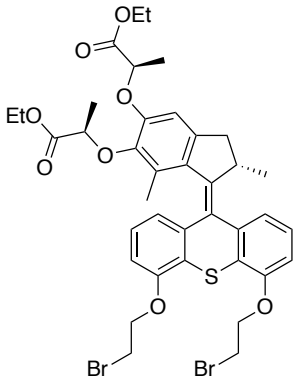

28

Compound (**28**) – bis-ester bis-bromo Motor

To a solution of compound **14** (1 eq., 60.0 mg, 0.099 mmol) in DMF (10 mL) under an argon atmosphere were added dibromoethane (6 eq., 112 mg, 0.051 mL, 0.6 mmol) and potassium carbonate (6 eq., 82 mg, 0.6 mmol). The solution was heated at 60°C for 2 days. The reaction mixture was then quenched with saturated NH_4Cl (10 mL). The aqueous phase was extracted with dichloromethane (3 x 20 mL). The combined organic layers were dried over sodium sulphate. The solvent was evaporated under reduced pressure. The crude residue was then purified by chromatography column (silica gel, CH_2Cl_2 --> CH_2Cl_2:MeOH = 99.5:0.5) affording compound **28** (30 mg, 37µmol, 37%) as a yellowish oil.

R_f = 0.8 (CH_2Cl_2)

^{1}H NMR (400 MHz, $CDCl_3$, 25°C) δ = 7.07-6.99 (m, 4H), 6.93 (dd, *J* = 7.1, 2.2 Hz, 2H), 6.66 (d, *J* = 0.9 Hz, 1H), 4.87 (q, *J* = 6.6 Hz, 2H), 4.33 (t, *J* = 3.5 Hz, 4H), 4.24 (qq, *J* = 6.3, 2.0 Hz, 4H), 3.79 (t, *J* = 3.5 Hz, 4H), 2.73-2.62 (m, 2H), 2.52 (s, 3H), 2.45-2.35 (m, 1H), 1.74 (d, *J* = 6.6 Hz, 6H), 1.21-1.12 (m, 3H), 1.03 (t, *J* = 6.4 Hz, 6H).

^{13}C NMR (100 MHz, $CDCl_3$, 25°C) δ = 170.9, 143.8, 156.8, 145.8, 144.5, 138.0, 132.6, 129.8, 127.8, 125.3, 122.4, 118.8, 115.3, 111.2, 108.3, 76.2, 75.8, 67.9, 61.5, 43.0, 29.1, 28.9, 21.8, 18.6, 14.3.

MS (ESI): m/z calculated $C_{38}H_{42}Br_2O_8S$ $[M+H]^+$ 816.10, Found 816.34.

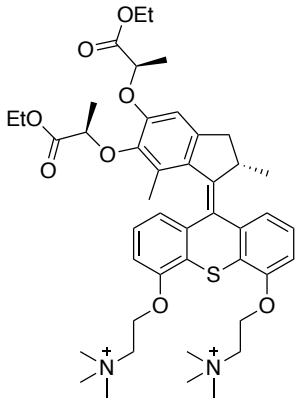

29

Compound (**29**) – bis-ester bis-ammonium Motor

To a solution of compound **28** (1 eq., 50.0 mg, 0.061 mmol) in EtOH (3 mL) under an argon atmosphere was added trimethylamine (346 eq., 5.0 mL, 21.15 mmol, 33% in EtOH). The solution was stirred overnight at 50 °C. After cooling down to room temperature, the reaction mixture was evaporated under reduced pressure affording compound **29** (47.5 mg, 61 µmol, 99%) as white solid.

^{1}H NMR (400 MHz, $CDCl_3$, 25°C) δ = 7.07-6.98 (m, 4H), 6.93 (dd, *J* = 7.1, 2.2 Hz, 2H), 6.66 (t, *J* = 0.8 Hz, 1H), 4.87 (q, *J* = 6.6 Hz, 2H), 4.39 (t, *J* = 5.2 Hz, 4H), 4.24 (qq, *J* = 6.3, 2.0 Hz, 4H), 3.85 (t, *J* = 5.2 Hz, 4H), 3.27 (s, 18H), 2.70-2.62 (m, 2H), 2.52 (s, 3H), 2.44-2.34 (m, 1H), 1.74 (d, *J* = 6.6 Hz, 6H), 1.14 (d, *J* = 5.8 Hz, 3H), 1.03 (t, *J* = 6.4 Hz, 6H).

^{13}C NMR (100 MHz, $CDCl_3$, 25°C) δ = 170.9, 159.0, 145.9, 144.6, 143.7, 141.0, 134.6, 134.1, 132.5, 129.9, 129.1,128.7, 128.0, 127.9, 126.8, 126.5, 125.2, 122.6, 118.1, 113.4, 108.4, 88.1, 76.3, 75.9, 72.3, 63.8, 61.7, 61.0, 57.3, 43.1, 28.7, 21.6, 18.5, 14.3, 14.1.

MS (ESI): m/z calculated for $C_{44}H_{60}N_2O_8S$ $[M]^{2+}$: 388.20, Found: 388.40.

Additional experimental procedure for Chapter II

Isomerization experiment

Isomers of the asymmetric motor **17** were isolated by HPLC using a Waters AutoPurify system. One of the isomers (17 mg) was then solubilized into a 11.8 mM solution of compound **17** in $CDCl_3$ (2 mL). The solution mixture was bubbled with argon for 5 min before being sealed in an NMR tube. Visible light irradiations were performed using a standard halogen lamp at a 10 cm distance. After a period of irradiation, the sample was kept in the dark while recording an NMR measurement.

Phosphorescence quenching experiment

Emission spectra were measured upon excitation at 532 nm with a 14 nm slit width, recorded in 1 nm increments integrated over 1 second using a 1 cm quartz cell. Lifetime measurements were recorded on the same instrument with excitation at 532 nm with a 14 nm slit width as

well as a monochromator at 700 nm, with 500 ns per channel. Fitting was performed to a single exponential with at least 1000 counts per measurement. All samples underwent three freeze-thaw-pump cycles before measurement to ensure the absence of dioxygen.

Gel formation

In a first vial, compound **26** (1 eq., 4.1 mg, 3.5 µmol) was dissolved in DMF (150 µL). In another vial, PEG-5600 bis-alkyne (2 eq., 39.2 mg, 6.99 µmol) was dissolved DMF (150 µL), under mild heating to allow solubilisation of the polymer. In the first vial containing the motor, CuBr (10 eq., 5.0 mg, 34.97 µmol) and PMDTA (10 eq., 6.1 mg, 7.31 µL, 34.97 µmol) were added, followed by the polymer solution. The resulting mixture was quickly transferred into a 0.5 mm thickness rheology mould. After 2 hours, the mould was opened and the gel transferred into an aqueous EDTA solution (20 mL). The solution was gently stirred for 10 min. After the complete discoloration of the material, the gel was transferred into water (20 mL) and washed several times in order to remove both EDTA and copper. The material was then placed subsequently into DMF:Water = 50:50 (20 mL) --> DMF:Water = 90:10 (20 mL) --> DMF (20 mL) --> 1,2,4-trichlorobenzene:DMF = 50:50 (20 mL) --> 1,2,3-trichlorobenzene (20 mL).

Gel Irradiation Experiments

Gel irradiations were performed using a home-made (**Figure Exp.12**) set-up consisting of cylindrical quartz cell with a 1 mm spacer, a Thorlabs 530 nm LED (M530F2), the corresponding fibre optic (M93L02) and a fibre adapter (SM1SMA). The whole set-up was powered by a Thorlabs LED driver (LEDD1B T-Cube). The contraction was recorded using a USB connected camera and VideoVelocity Free software. Fiji (*aka* ImageJ) was used to process the snapshots and to measure the size of the gel. Data were processed using Python and the Pyplot/Numpy library.

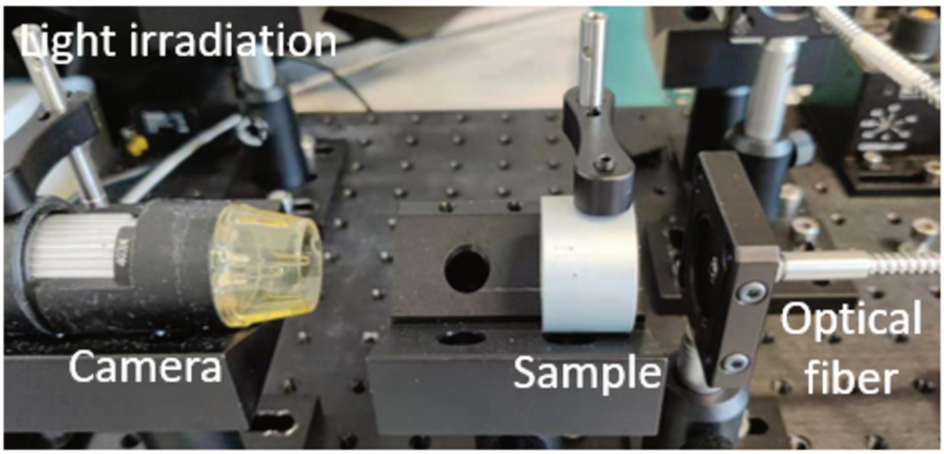

Figure Exp.12. *Photograph of the gel irradiation set-up. A LED irradiates at 530 nm the material while a camera records its contraction.*

Gel pieces (5 x 5 mm) were swollen in a solution of 1,2,4-trichlorobenzene containing Pd-TPP at a given concentration for at least 1 day. Argon was bubbled for 30 min before the sample was placed in a cylindrical quartz cell. The cell was then irradiated at a selected power while the contraction was monitored. During irradiation, the entire set-up was kept in the dark by a black cover.

Additional experimental procedures for Chapter III

Janus particles preparation

Janus particles were synthesized by Dr. Vauthier according to a protocol described in the literature.[156] They were received dispersed in an aqueous solution at 2 g/L.

Motor - Janus particles preparation

The aqueous solution of Janus particles is filtered through cotton before being diluted with miliQ water to a concentration of 0.2 g/L. In parallel, a solution of motor **29** at 1 g/L is prepared in miliQ water. The motor solution is then added to the JNPs solution in varying amounts. The resulting mixture is finally mixed gently and can be stored in the refrigerator for up to one month.

References

(1) Koumura, N.; Zijlstra, R. W. J.; van Delden, R. A.; Harada, N.; Feringa, B. L. Light-Driven Monodirectional Molecular Rotor. *Nature* **1999**, *401* (6749), 152–155. https://doi.org/10.1038/43646.

(2) Kassem, S.; van Leeuwen, T.; Lubbe, A. S.; Wilson, M. R.; Feringa, B. L.; Leigh, D. A. Artificial Molecular Motors. *Chem. Soc. Rev.* **2017**, *46* (9), 2592–2621. https://doi.org/10.1039/C7CS00245A.

(3) Dattler, D.; Fuks, G.; Heiser, J.; Moulin, E.; Perrot, A.; Yao, X.; Giuseppone, N. Design of Collective Motions from Synthetic Molecular Switches, Rotors, and Motors. *Chem. Rev.* **2020**, *120* (1), 310–433. https://doi.org/10.1021/acs.chemrev.9b00288.

(4) Klok, M.; Boyle, N.; Pryce, M. T.; Meetsma, A.; Browne, W. R.; Feringa, B. L. MHz Unidirectional Rotation of Molecular Rotary Motors. *J. Am. Chem. Soc.* **2008**, *130* (32), 10484–10485. https://doi.org/10.1021/ja8037245.

(5) Feringa, B. L. The Art of Building Small: From Molecular Switches to Motors (Nobel Lecture). *Angew. Chemie Int. Ed.* **2017**, *56* (37), 11060–11078. https://doi.org/10.1002/anie.201702979.

(6) Li, Q.; Fuks, G.; Moulin, E.; Maaloum, M.; Rawiso, M.; Kulic, I.; Foy, J. T.; Giuseppone, N. Macroscopic Contraction of a Gel Induced by the Integrated Motion of Light-Driven Molecular Motors. *Nat. Nanotechnol.* **2015**, *10* (2), 161–165. https://doi.org/10.1038/nnano.2014.315.

(7) Foy, J. T.; Li, Q.; Goujon, A.; Colard-Itté, J.-R.; Fuks, G.; Moulin, E.; Schiffmann, O.; Dattler, D.; Funeriu, D. P.; Giuseppone, N. Dual-Light Control of Nanomachines That Integrate Motor and Modulator Subunits. *Nat. Nanotechnol.* **2017**, *12* (6), 540–545. https://doi.org/10.1038/nnano.2017.28.

(8) Li, Q.; Foy, J. T.; Colard-Itté, J.-R.; Goujon, A.; Dattler, D.; Fuks, G.; Moulin, E.; Giuseppone, N. Gram Scale Synthesis of Functionalized and Optically Pure Feringa's Motors. *Tetrahedron* **2017**, *73* (33), 4874–4882. https://doi.org/10.1016/j.tet.2017.05.023.

(9) Cnossen, A.; Hou, L.; Pollard, M. M.; Wesenhagen, P. V.; Browne, W. R.; Feringa, B. L. Driving Unidirectional Molecular Rotary Motors with Visible Light by Intra- And Intermolecular Energy Transfer from Palladium Porphyrin. *J. Am. Chem. Soc.* **2012**, *134* (42), 17613–17619. https://doi.org/10.1021/ja306986g.

(10) Chen, J.; Kistemaker, J. C. M.; Robertus, J.; Feringa, B. L. Molecular Stirrers in Action. *J. Am. Chem. Soc.* **2014**, *136* (42), 14924–14932. https://doi.org/10.1021/ja507711h.

(11) Palagi, S.; Fischer, P. Bioinspired Microrobots. *Nat. Rev. Mater.* **2018**, *3* (6), 113–124. https://doi.org/10.1038/s41578-018-0016-9.

(12) Eberhard, W.; Wcislo, W. Plenty of Room at the Bottom? *Am. Sci.* **2012**, *100* (3), 226. https://doi.org/10.1511/2012.96.226.

(13) Erbas-Cakmak, S.; Leigh, D. A.; McTernan, C. T.; Nussbaumer, A. L. Artificial Molecular Machines. *Chem. Rev.* **2015**, *115* (18), 10081–10206. https://doi.org/10.1021/acs.chemrev.5b00146.

(14) Yamada, M.; Kondo, M.; Mamiya, J.; Yu, Y.; Kinoshita, M.; Barrett, C. J.; Ikeda, T. Photomobile Polymer Materials: Towards Light-Driven Plastic Motors. *Angew. Chemie Int. Ed.* **2008**, *47* (27), 4986–4988. https://doi.org/10.1002/anie.200800760.

(15) Baroncini, M.; Silvi, S.; Credi, A. Photo- and Redox-Driven Artificial Molecular Motors. *Chem. Rev.* **2020**, *120* (1), 200–268. https://doi.org/10.1021/acs.chemrev.9b00291.

(16) Motors, M. *Molecular Motors*; Schliwa, M., Ed.; Wiley, 2002. https://doi.org/10.1002/3527601503.

(17) Sherman, W. B.; Seeman, N. C. A Precisely Controlled DNA Biped Walking Device. *Nano Lett.* **2004**, *4* (7), 1203–1207. https://doi.org/10.1021/nl049527q.

(18) Cheng, C.; McGonigal, P. R.; Schneebeli, S. T.; Li, H.; Vermeulen, N. A.; Ke, C.; Stoddart, J. F. An Artificial Molecular Pump. *Nat. Nanotechnol.* **2015**, *10* (6), 547–553. https://doi.org/10.1038/nnano.2015.96.

(19) Leigh, D. A. Genesis of the Nanomachines: The 2016 Nobel Prize in Chemistry. *Angew. Chemie Int. Ed.* **2016**, *55* (47), 14506–14508. https://doi.org/10.1002/anie.201609841.

(20) Sweeney, H. L.; Houdusse, A. Structural and Functional Insights into the Myosin Motor Mechanism. *Annu. Rev. Biophys.* **2010**, *39* (1), 539–557. https://doi.org/10.1146/annurev.biophys.050708.133751.

(21) Hirokawa, N. Kinesin and Dynein Superfamily Proteins and the Mechanism of Organelle Transport. *Science (80-.).* **1998**, *279* (5350), 519–526. https://doi.org/10.1126/science.279.5350.519.

(22) Delius, M. Von; Leigh, D. A. Walking Molecules. *Chem. Soc. Rev.* **2011**, *40* (7), 3656–3676. https://doi.org/10.1039/c1cs15005g.

(23) Shin, J. S.; Pierce, N. A. A Synthetic DNA Walker for Molecular Transport. *J. Am. Chem. Soc.* **2004**, *126* (35), 10834–10835. https://doi.org/10.1021/ja047543j.

(24) Liu, M.; Cheng, J.; Tee, S. R.; Sreelatha, S.; Loh, I. Y.; Wang, Z. Biomimetic Autonomous Enzymatic Nanowalker of High Fuel Efficiency. *ACS Nano* **2016**, *10* (6), 5882–5890. https://doi.org/10.1021/acsnano.6b01035.

(25) Cha, T. G.; Pan, J.; Chen, H.; Salgado, J.; Li, X.; Mao, C.; Choi, J. H. A Synthetic DNA Motor That Transports Nanoparticles along Carbon Nanotubes. *Nat. Nanotechnol.* **2014**, *9* (1), 39–43. https://doi.org/10.1038/nnano.2013.257.

(26) He, Y.; Liu, D. R. Autonomous Multistep Organic Synthesis in a Single Isothermal Solution Mediated by a DNA Walker. *Nat. Nanotechnol.* **2010**, *5* (11), 778–782. https://doi.org/10.1038/nnano.2010.190.

(27) Omabegho, T.; Sha, R.; Seeman, N. C. A Bipedal DNA Brownian Motor with Coordinated Legs. *Science (80-.).* **2009**, *324* (5923), 67–71. https://doi.org/10.1126/science.1170336.

(28) Lund, K.; Manzo, A. J.; Dabby, N.; Michelotti, N.; Johnson-Buck, A.; Nangreave, J.; Taylor, S.; Pei, R.; Stojanovic, M. N.; Walter, N. G.; et al. Molecular Robots Guided by Prescriptive Landscapes. *Nature* **2010**, *465* (7295), 206–209. https://doi.org/10.1038/nature09012.

(29) Yin, P.; Yan, H.; Daniell, X. G.; Turberfield, A. J.; Reif, J. H. A Unidirectional DNA Walker That Moves Autonomously along a Track. *Angew. Chemie* **2004**, *116* (37), 5014–5019. https://doi.org/10.1002/ange.200460522.

(30) Loh, I. Y.; Cheng, J.; Tee, S. R.; Efremov, A.; Wang, Z. From Bistate Molecular Switches to Self-Directed Track-Walking Nanomotors. *ACS Nano* **2014**, *8* (10), 10293–10304. https://doi.org/10.1021/nn5034983.

(31) You, M.; Chen, Y.; Zhang, X.; Liu, H.; Wang, R.; Wang, K.; Williams, K. R.; Tan, W. An Autonomous and Controllable Light-Driven DNA Walking Device. *Angew. Chemie - Int. Ed.* **2012**, *51* (10), 2457–2460. https://doi.org/10.1002/anie.201107733.

(32) Bath, J.; Green, S. J.; Allen, K. E.; Turberfield, A. J. Mechanism for a Directional, Processive, and Reversible DNA Motor. *Small* **2009**, *5* (13), 1513–1516.

https://doi.org/10.1002/smll.200900078.

(33) Von Delius, M.; Geertsema, E. M.; Leigh, D. A. A Synthetic Small Molecule That Can Walk down a Track. *Nat. Chem.* **2010**, *2* (2), 96–101. https://doi.org/10.1038/nchem.481.

(34) Von Delius, M.; Geertsema, E. M.; Leigh, D. A.; Tang, D. T. D. Design, Synthesis, and Operation of Small Molecules That Walk along Tracks. *J. Am. Chem. Soc.* **2010**, *132* (45), 16134–16145. https://doi.org/10.1021/ja106486b.

(35) Barrell, M. J.; Campaña, A. G.; von Delius, M.; Geertsema, E. M.; Leigh, D. A. Light-Driven Transport of a Molecular Walker in Either Direction along a Molecular Track. *Angew. Chemie* **2011**, *123* (1), 299–304. https://doi.org/10.1002/ange.201004779.

(36) Campaña, A. G.; Leigh, D. A.; Lewandowska, U. One-Dimensional Random Walk of a Synthetic Small Molecule Toward a Thermodynamic Sink. *J. Am. Chem. Soc.* **2013**, *135* (23), 8639–8645. https://doi.org/10.1021/ja402382n.

(37) Kaplan, J. H. Biochemistry of Na,K-ATPase. *Annu. Rev. Biochem.* **2002**, *71* (1), 511–535. https://doi.org/10.1146/annurev.biochem.71.102201.141218.

(38) Brandt, U. Energy Converting NADH: Quinone Oxidoreductase (Complex I). *Annu. Rev. Biochem.* **2006**, *75* (1), 69–92. https://doi.org/10.1146/annurev.biochem.75.103004.142539.

(39) Amabilino, D. B.; Stoddart, J. F. Interlocked and Intertwined Structures and Superstructures. *Chem. Rev.* **1995**, *95* (8), 2725–2828. https://doi.org/10.1021/cr00040a005.

(40) Harrison, I. T.; Harrison, S. Synthesis of a Stable Complex of a Macrocycle and a Threaded Chain. *J. Am. Chem. Soc.* **1967**, *89* (22), 5723–5724. https://doi.org/10.1021/ja00998a052.

(41) Schill, G.; Zollenkopf, H. Rotaxan-Verbindungen, I1). *Justus Liebigs Ann. Chem.* **1969**, *721* (1), 53–74. https://doi.org/10.1002/jlac.19697210109.

(42) *Molecular Catenanes, Rotaxanes and Knots*; Sauvage, J. -P., Dietrich-Buchecker, C., Eds.; Wiley, 1999. https://doi.org/10.1002/9783527613724.

(43) Anelli, P. L.; Spencer, N.; Fraser Stoddart, J. A Molecular Shuttle. *J. Am. Chem. Soc.* **1991**, *113* (13), 5131–5133. https://doi.org/10.1021/ja00013a096.

(44) Benniston, A. C.; Harriman, A. A Light-Induced Molecular Shuttle Based on a [2]Rotaxane-Derived Triad. *Angew. Chemie Int. Ed. English* **1993**, *32* (10), 1459–1461. https://doi.org/10.1002/anie.199314591.

(45) Bissell, R. A.; Córdova, E.; Kaifer, A. E.; Stoddart, J. F. A Chemically and Electrochemically Switchable Molecular Shuttle. *Nature* **1994**, *369* (6476), 133–137. https://doi.org/10.1038/369133a0.

(46) Bottari, G.; Dehez, F.; Leigh, D. A.; Nash, P. J.; Pérez, E. M.; Wong, J. K. Y.; Zerbetto, F. Entropy-Driven Translational Isomerism: A Tristable Molecular Shuttle. *Angew. Chemie Int. Ed.* **2003**, *42* (47), 5886–5889. https://doi.org/10.1002/anie.200352176.

(47) Chatterjee, M. N.; Kay, E. R.; Leigh, D. A. Beyond Switches: Ratcheting a Particle Energetically Uphill with a Compartmentalized Molecular Machine. *J. Am. Chem. Soc.* **2006**, *128* (12), 4058–4073. https://doi.org/10.1021/ja057664z.

(48) Ashton, P. R.; Baxter, I.; Fyfe, M. C. T.; Raymo, F. M.; Spencer, N.; Stoddart, J. F.; White, A. J. P.; Williams, D. J. Rotaxane or Pseudorotaxane? That Is the Question! †. *J. Am. Chem. Soc.* **1998**, *120* (10), 2297–2307. https://doi.org/10.1021/ja9731276.

(49) Xue, M.; Yang, Y.; Chi, X.; Yan, X.; Huang, F. Development of Pseudorotaxanes and Rotaxanes: From Synthesis to Stimuli-Responsive Motions to Applications. *Chem. Rev.* **2015**, *115* (15), 7398–7501. https://doi.org/10.1021/cr5005869.

(50) Baroncini, M.; Silvi, S.; Venturi, M.; Credi, A.

Photoactivated Directionally Controlled Transit of a Non-Symmetric Molecular Axle Through a Macrocycle. *Angew. Chemie* **2012**, *124* (17), 4299–4302. https://doi.org/10.1002/ange.201200555.

(51) Ragazzon, G.; Baroncini, M.; Silvi, S.; Venturi, M.; Credi, A. Light-Powered Autonomous and Directional Molecular Motion of a Dissipative Self-Assembling System. *Nat. Nanotechnol.* **2015**, *10* (1), 70–75. https://doi.org/10.1038/nnano.2014.260.

(52) Odell, B.; Reddington, M. V; Slawin, A. M. Z.; Spencer, N.; Stoddart, J. F.; Williams, D. J. Cyclobis(Paraquat-p-Phenylene). A Tetracationic Multipurpose Receptor. *Angew. Chemie Int. Ed. English* **1988**, *27* (11), 1547–1550. https://doi.org/10.1002/anie.198815471.

(53) Li, H.; Cheng, C.; McGonigal, P. R.; Fahrenbach, A. C.; Frasconi, M.; Liu, W.-G.; Zhu, Z.; Zhao, Y.; Ke, C.; Lei, J.; et al. Relative Unidirectional Translation in an Artificial Molecular Assembly Fueled by Light. *J. Am. Chem. Soc.* **2013**, *135* (49), 18609–18620. https://doi.org/10.1021/ja4094204.

(54) Cheng, C.; McGonigal, P. R.; Liu, W.-G.; Li, H.; Vermeulen, N. A.; Ke, C.; Frasconi, M.; Stern, C. L.; Goddard III, W. A.; Stoddart, J. F. Energetically Demanding Transport in a Supramolecular Assembly. *J. Am. Chem. Soc.* **2014**, *136* (42), 14702–14705. https://doi.org/10.1021/ja508615f.

(55) Fahrenbach, A. C.; Barnes, J. C.; Lanfranchi, D. A.; Li, H.; Coskun, A.; Gassensmith, J. J.; Liu, Z.; Benítez, D.; Trabolsi, A.; Goddard, W. A.; et al. Solution-Phase Mechanistic Study and Solid-State Structure of a Tris(Bipyridinium Radical Cation) Inclusion Complex. *J. Am. Chem. Soc.* **2012**, *134* (6), 3061–3072. https://doi.org/10.1021/ja2089603.

(56) Qiu, Y.; Zhang, L.; Pezzato, C.; Feng, Y.; Li, W.; Nguyen, M. T.; Cheng, C.; Shen, D.; Guo, Q.-H.; Shi, Y.; et al. A Molecular Dual Pump. *J. Am. Chem. Soc.* **2019**, *141* (44), 17472–17476. https://doi.org/10.1021/jacs.9b08927.

(57) Qiu, Y.; Song, B.; Pezzato, C.; Shen, D.; Liu, W.; Zhang, L.; Feng, Y.; Guo, Q.-H.; Cai, K.; Li, W.; et al. A Precise Polyrotaxane Synthesizer. *Science (80-.).* **2020**, *368* (6496), 1247–1253. https://doi.org/10.1126/science.abb3962.

(58) Wasserman, E. The Preparation of Interlocking Rings: A Catenane. *J. Am. Chem. Soc.* **1960**, *82* (16), 4433–4434. https://doi.org/10.1021/ja01501a082.

(59) Schill, G.; Lüttringhaus, A. The Preparation of Catena Compounds by Directed Synthesis. *Angew. Chemie Int. Ed. English* **1964**, *3* (8), 546–547. https://doi.org/10.1002/anie.196405461.

(60) Beves, J. E.; Blight, B. A.; Campbell, C. J.; Leigh, D. A.; McBurney, R. T. Strategies and Tactics for the Metal-Directed Synthesis of Rotaxanes, Knots, Catenanes, and Higher Order Links. *Angew. Chemie - Int. Ed.* **2011**, *50* (40), 9260–9327. https://doi.org/10.1002/anie.201007963.

(61) Dietrich-Buchecker, C. O.; Sauvage, J. P. Interlocking of Molecular Threads: From the Statistical Approach to the Templated Synthesis of Catenands. *Chem. Rev.* **1987**, *87* (4), 795–810. https://doi.org/10.1021/cr00080a007.

(62) Crowley, J. D.; Goldup, S. M.; Lee, A.-L.; Leigh, D. A.; McBurney, R. T. Active Metal Template Synthesis of Rotaxanes, Catenanes and Molecular Shuttles. *Chem. Soc. Rev.* **2009**, *38* (6), 1530. https://doi.org/10.1039/b804243h.

(63) Gil-Ramírez, G.; Leigh, D. A.; Stephens, A. J. Catenanes: Fifty Years of Molecular Links. *Angew. Chemie Int. Ed.* **2015**, *54* (21), 6110–6150. https://doi.org/10.1002/anie.201411619.

(64) Prakasam, T.; Lusi, M.; Elhabiri, M.; Platas-Iglesias, C.; Olsen, J.-C.; Asfari, Z.; Cianférani-Sanglier, S.; Debaene, F.; Charbonnière, L. J.; Trabolsi, A. Simultaneous Self-Assembly of a [2]Catenane, a Trefoil Knot, and a Solomon Link from a Simple Pair of Ligands. *Angew. Chemie* **2013**, *125* (38), 10140–10144.

https://doi.org/10.1002/ange.201302425.

(65) Mendes, P. M.; Flood, A. H.; Stoddart, J. F. Nanoelectronic Devices from Self-Organized Molecular Switches. *Appl. Phys. A* **2005**, *80* (6), 1197–1209. https://doi.org/10.1007/s00339-004-3172-2.

(66) Xing, H.; Li, Z.; Wu, Z. L.; Huang, F. Catenane Crosslinked Mechanically Adaptive Polymer Gel. *Macromol. Rapid Commun.* **2018**, *39* (1), 1700361. https://doi.org/10.1002/marc.201700361.

(67) Cárdenas, D. J.; Livoreil, A.; Sauvage, J.-P. Redox Control of the Ring-Gliding Motion in a Cu-Complexed Catenane: A Process Involving Three Distinct Geometries. *J. Am. Chem. Soc.* **1996**, *118* (47), 11980–11981. https://doi.org/10.1021/ja962774e.

(68) Leigh, D. A.; Wong, J. K. Y.; Dehez, F.; Zerbetto, F. Unidirectional Rotation in a Mechanically Interlocked Molecular Rotor. *Nature* **2003**, *424* (6945), 174–179. https://doi.org/10.1038/nature01758.

(69) Hernandez, J. V. A Reversible Synthetic Rotary Molecular Motor. *Science (80-.).* **2004**, *306* (5701), 1532–1537. https://doi.org/10.1126/science.1103949.

(70) Wilson, M. R.; Solà, J.; Carlone, A.; Goldup, S. M.; Lebrasseur, N.; Leigh, D. A. An Autonomous Chemically Fuelled Small-Molecule Motor. *Nature* **2016**, *534* (7606), 235–240. https://doi.org/10.1038/nature18013.

(71) Boyer, P. D. THE ATP SYNTHASE—A SPLENDID MOLECULAR MACHINE. *Annu. Rev. Biochem.* **1997**, *66* (1), 717–749. https://doi.org/10.1146/annurev.biochem.66.1.717.

(72) Noji, H.; Yasuda, R.; Yoshida, M.; Kinosita, K. Direct Observation of the Rotation of F1-ATPase. *Nature* **1997**, *386* (6622), 299–302. https://doi.org/10.1038/386299a0.

(73) Zheng, J. Ultrafast Carbon-Carbon Single-Bond Rotational Isomerization in Room-Temperature Solution. *Science (80-.).* **2006**, *313* (5795), 1951–1955. https://doi.org/10.1126/science.1132178.

(74) Kelly, T. R.; De Silva, H.; Silva, R. A. Unidirectional Rotary Motion in a Molecular System. *Nature* **1999**, *401* (6749), 150–152. https://doi.org/10.1038/43639.

(75) Kelly, T. R.; Silva, R. A.; De Silva, H.; Jasmin, S.; Zhao, Y. A Rationally Designed Prototype of a Molecular Motor. *J. Am. Chem. Soc.* **2000**, *122* (29), 6935–6949. https://doi.org/10.1021/ja001048f.

(76) Mock, W. L.; Ochwat, K. J. Theory and Example of a Small-Molecule Motor. *J. Phys. Org. Chem.* **2003**, *16* (3), 175–182. https://doi.org/10.1002/poc.591.

(77) Fletcher, S. P. A Reversible, Unidirectional Molecular Rotary Motor Driven by Chemical Energy. *Science (80-.).* **2005**, *310* (5745), 80–82. https://doi.org/10.1126/science.1117090.

(78) Collins, B. S. L.; Kistemaker, J. C. M.; Otten, E.; Feringa, B. L. A Chemically Powered Unidirectional Rotary Molecular Motor Based on a Palladium Redox Cycle. *Nat. Chem.* **2016**, *8* (9), 860–866. https://doi.org/10.1038/nchem.2543.

(79) Tierney, H. L.; Murphy, C. J.; Jewell, A. D.; Baber, A. E.; Iski, E. V.; Khodaverdian, H. Y.; McGuire, A. F.; Klebanov, N.; Sykes, E. C. H. Experimental Demonstration of a Single-Molecule Electric Motor. *Nat. Nanotechnol.* **2011**, *6* (10), 625–629. https://doi.org/10.1038/nnano.2011.142.

(80) Perera, U. G. E.; Ample, F.; Kersell, H.; Zhang, Y.; Vives, G.; Echeverria, J.; Grisolia, M.; Rapenne, G.; Joachim, C.; Hla, S.-W. Controlled Clockwise and Anticlockwise Rotational Switching of a Molecular Motor. *Nat. Nanotechnol.* **2013**, *8* (1), 46–51. https://doi.org/10.1038/nnano.2012.218.

(81) Gmelin, L. *Hand-Book of Chemistry: Organic*

Chemistry, Vol. 6. Organic Compounds Containing Fourteen Atoms of Carbon; 1858; Vol. 12.

(82) Muszkat, K. A.; Fischer, E. Structure, Spectra, Photochemistry, and Thermal Reactions of the 4a,4b-Dihydrophenanthrenes. *J. Chem. Soc. B Phys. Org.* **1967**, No. 662, 662. https://doi.org/10.1039/j29670000662.

(83) Koumura, N.; Geertsema, E. M.; Meetsma, A.; Feringa, B. L. Light-Driven Molecular Rotor: Unidirectional Rotation Controlled by a Single Stereogenic Center. *J. Am. Chem. Soc.* **2000**, *122* (48), 12005–12006. https://doi.org/10.1021/ja002755b.

(84) Koumura, N.; Geertsema, E. M.; van Gelder, M. B.; Meetsma, A.; Feringa, B. L. Second Generation Light-Driven Molecular Motors. Unidirectional Rotation Controlled by a Single Stereogenic Center with Near-Perfect Photoequilibria and Acceleration of the Speed of Rotation by Structural Modification. *J. Am. Chem. Soc.* **2002**, *124* (18), 5037–5051. https://doi.org/10.1021/ja012499i.

(85) Kistemaker, J. C. M.; Štacko, P.; Visser, J.; Feringa, B. L. Unidirectional Rotary Motion in Achiral Molecular Motors. *Nat. Chem.* **2015**, *7* (11), 890–896. https://doi.org/10.1038/nchem.2362.

(86) Wezenberg, S. J.; Feringa, B. L. Supramolecularly Directed Rotary Motion in a Photoresponsive Receptor. *Nat. Commun.* **2018**, *9* (1), 1984. https://doi.org/10.1038/s41467-018-04249-x.

(87) Ruangsupapichat, N.; Pollard, M. M.; Harutyunyan, S. R.; Feringa, B. L. Reversing the Direction in a Light-Driven Rotary Molecular Motor. *Nat. Chem.* **2011**, *3* (1), 53–60. https://doi.org/10.1038/nchem.872.

(88) Augulis, R.; Klok, M.; Feringa, B. L.; Loosdrecht, P. H. M. van. Light-Driven Rotary Molecular Motors: An Ultrafast Optical Study. *Phys. status solidi* **2009**, *6* (1), 181–184. https://doi.org/10.1002/pssc.200879808.

(89) Conyard, J.; Addison, K.; Heisler, I. A.; Cnossen, A.; Browne, W. R.; Feringa, B. L.; Meech, S. R. Ultrafast Dynamics in the Power Stroke of a Molecular Rotary Motor. *Nat. Chem.* **2012**, *4* (7), 547–551. https://doi.org/10.1038/nchem.1343.

(90) Vicario, J.; Walko, M.; Meetsma, A.; Feringa, B. L. Fine Tuning of the Rotary Motion by Structural Modification in Light-Driven Unidirectional Molecular Motors. *J. Am. Chem. Soc.* **2006**, *128* (15), 5127–5135. https://doi.org/10.1021/ja058303m.

(91) Pollard, M. M.; Meetsma, A.; Feringa, B. L. A Redesign of Light-Driven Rotary Molecular Motors. *Org. Biomol. Chem.* **2008**, *6* (3), 507–512. https://doi.org/10.1039/B715652A.

(92) Fernández Landaluce, T.; London, G.; Pollard, M. M.; Rudolf, P.; Feringa, B. L. Rotary Molecular Motors: A Large Increase in Speed through a Small Change in Design. *J. Org. Chem.* **2010**, *75* (15), 5323–5325. https://doi.org/10.1021/jo1006976.

(93) Vicario, J.; Meetsma, A.; Feringa, B. L. Controlling the Speed of Rotation in Molecular Motors. Dramatic Acceleration of the Rotary Motion by Structural Modification. *Chem. Commun.* **2005**, No. 47, 5910. https://doi.org/10.1039/b507264f.

(94) Feringa, B. L.; Jager, W. F.; de Lange, B. Resolution of Sterically Overcrowded Ethylenes; a Remarkable Correlation between Bond Lengths and Racemization Barriers. *Tetrahedron Lett.* **1992**, *33* (20), 2887–2890. https://doi.org/10.1016/S0040-4039(00)78887-3.

(95) Kistemaker, J. C. M.; Lubbe, A. S.; Bloemsma, E. A.; Feringa, B. L. On the Role of Viscosity in the Eyring Equation. *ChemPhysChem* **2016**, *17* (12), 1819–1822. https://doi.org/10.1002/cphc.201501177.

(96) Conyard, J.; Cnossen, A.; Browne, W. R.;

Feringa, B. L.; Meech, S. R. Chemically Optimizing Operational Efficiency of Molecular Rotary Motors. *J. Am. Chem. Soc.* **2014**, *136* (27), 9692–9700. https://doi.org/10.1021/ja5041368.

(97) Lehn, J.-M. Conjecture: Imines as Unidirectional Photodriven Molecular Motors—Motional and Constitutional Dynamic Devices. *Chem. - A Eur. J.* **2006**, *12* (23), 5910–5915. https://doi.org/10.1002/chem.200600489.

(98) Greb, L.; Lehn, J.-M. Light-Driven Molecular Motors: Imines as Four-Step or Two-Step Unidirectional Rotors. *J. Am. Chem. Soc.* **2014**, *136* (38), 13114–13117. https://doi.org/10.1021/ja506034n.

(99) Guentner, M.; Schildhauer, M.; Thumser, S.; Mayer, P.; Stephenson, D.; Mayer, P. J.; Dube, H. Sunlight-Powered KHz Rotation of a Hemithioindigo-Based Molecular Motor. *Nat. Commun.* **2015**, *6* (1), 8406. https://doi.org/10.1038/ncomms9406.

(100) Kistemaker, J. C. M.; Lubbe, A. S.; Feringa, B. L. Exploring Molecular Motors. *Mater. Chem. Front.* **2021**, *5* (7), 2900–2906. https://doi.org/10.1039/D0QM01091J.

(101) Vives, G.; Tour, J. M. Synthesis of Single-Molecule Nanocars. *Acc. Chem. Res.* **2009**, *42* (3), 473–487. https://doi.org/10.1021/ar8002317.

(102) Morin, J.-F.; Shirai, Y.; Tour, J. M. En Route to a Motorized Nanocar. *Org. Lett.* **2006**, *8* (8), 1713–1716. https://doi.org/10.1021/ol060445d.

(103) Kudernac, T.; Ruangsupapichat, N.; Parschau, M.; Maciá, B.; Katsonis, N.; Harutyunyan, S. R.; Ernst, K.-H.; Feringa, B. L. Electrically Driven Directional Motion of a Four-Wheeled Molecule on a Metal Surface. *Nature* **2011**, *479* (7372), 208–211. https://doi.org/10.1038/nature10587.

(104) Rapenne, G.; Joachim, C. The First Nanocar Race. *Nat. Rev. Mater.* **2017**, *2* (6), 17040. https://doi.org/10.1038/natrevmats.2017.40.

(105) Eelkema, R.; Pollard, M. M.; Vicario, J.; Katsonis, N.; Ramon, B. S.; Bastiaansen, C. W. M.; Broer, D. J.; Feringa, B. L. Nanomotor Rotates Microscale Objects. *Nature* **2006**, *440* (7081), 163–163. https://doi.org/10.1038/440163a.

(106) Chen, J.; Leung, F. K.-C.; Stuart, M. C. A.; Kajitani, T.; Fukushima, T.; van der Giessen, E.; Feringa, B. L. Artificial Muscle-like Function from Hierarchical Supramolecular Assembly of Photoresponsive Molecular Motors. *Nat. Chem.* **2018**, *10* (2), 132–138. https://doi.org/10.1038/nchem.2887.

(107) Feldman, D. Polymer Weathering: Photo-Oxidation. *J. Polym. Environ.* **2002**, *10* (4), 163–173. https://doi.org/10.1023/A:1021148205366.

(108) Pattison, D. I.; Rahmanto, A. S.; Davies, M. J. Photo-Oxidation of Proteins. *Photochem. Photobiol. Sci.* **2012**, *11* (1), 38–53. https://doi.org/10.1039/C1PP05164D.

(109) Klajn, R. Spiropyran-Based Dynamic Materials. *Chem. Soc. Rev.* **2014**, *43* (1), 148–184. https://doi.org/10.1039/c3cs60181a.

(110) Berkovic, G.; Krongauz, V.; Weiss, V. Spiropyrans and Spirooxazines for Memories and Switches. *Chem. Rev.* **2000**, *100* (5), 1741–1754. https://doi.org/10.1021/cr9800715.

(111) Bléger, D.; Hecht, S. Visible-Light-Activated Molecular Switches. *Angew. Chemie - Int. Ed.* **2015**, *54* (39), 11338–11349. https://doi.org/10.1002/anie.201500628.

(112) Kaiser, W.; Garrett, C. G. B. Two-Photon Excitation in CaF2: Eu2+. *Phys. Rev. Lett.* **1961**, *7* (6), 229–231. https://doi.org/10.1103/PhysRevLett.7.229.

(113) Boustany, N. N.; Thakor, N. V. Light Scattering Spectroscopy and Imaging of Cellular and Subcellular Events. *Biomed. Photonics Handbook, Second Ed. Fundam. Devices, Tech.* **2014**, 461–488.

https://doi.org/10.1201/b17290.

(114) Roke, D.; Sen, M.; Danowski, W.; Wezenberg, S. J.; Feringa, B. L. Visible-Light-Driven Tunable Molecular Motors Based on Oxindole. *J. Am. Chem. Soc.* **2019**, *141* (18), 7622–7627. https://doi.org/10.1021/jacs.9b03237.

(115) Gerwien, A.; Mayer, P.; Dube, H. Photon-Only Molecular Motor with Reverse Temperature-Dependent Efficiency. *J. Am. Chem. Soc.* **2018**, *140* (48), 16442–16446. https://doi.org/10.1021/jacs.8b10660.

(116) Van Delden, R. A.; Koumura, N.; Schoevaars, A.; Meetsma, A.; Feringa, B. L. A Donor-Acceptor Substituted Molecular Motor: Unidirectional Rotation Driven by Visible Light. *Org. Biomol. Chem.* **2003**, *1* (1), 33–35. https://doi.org/10.1039/b209378b.

(117) Van Leeuwen, T.; Pol, J.; Roke, D.; Wezenberg, S. J.; Feringa, B. L. Visible-Light Excitation of a Molecular Motor with an Extended Aromatic Core. *Org. Lett.* **2017**, *19* (6), 1402–1405. https://doi.org/10.1021/acs.orglett.7b00317.

(118) Wezenberg, S. J.; Chen, K.-Y.; Feringa, B. L. Visible-Light-Driven Photoisomerization and Increased Rotation Speed of a Molecular Motor Acting as a Ligand in a Ruthenium(II) Complex. *Angew. Chemie, Int. Ed.* **2015**, *54* (39), 11457–11461. https://doi.org/10.1002/anie.201505781.

(119) Pfeifer, L.; Scherübl, M.; Fellert, M.; Danowski, W.; Cheng, J.; Pol, J.; Feringa, B. L. Photoefficient 2nd Generation Molecular Motors Responsive to Visible Light. *Chem. Sci.* **2019**, *10* (38), 8768–8773. https://doi.org/10.1039/c9sc02150g.

(120) Danowski, W.; Castiglioni, F.; Sardjan, A. S.; Krause, S.; Pfeifer, L.; Roke, D.; Comotti, A.; Browne, W. R.; Feringa, B. L. Visible-Light-Driven Rotation of Molecular Motors in a Dual-Function Metal-Organic Framework Enabled by Energy Transfer. *J. Am. Chem. Soc.* **2020**, *142* (19), 9048–9056. https://doi.org/10.1021/jacs.0c03063.

(121) Eastwood, D.; Gouterman, M. Porphyrins. *J. Mol. Spectrosc.* **1970**, *35* (3), 359–375. https://doi.org/10.1016/0022-2852(70)90179-7.

(122) London, G.; Carroll, G. T.; Fernández Landaluce, T.; Pollard, M. M.; Rudolf, P.; Feringa, B. L. Light-Driven Altitudinal Molecular Motors on Surfaces. *Chem. Commun.* **2009**, No. 13, 1712–1714. https://doi.org/10.1039/b821755f.

(123) Pollard, M. M.; Ter Wiel, M. K. J.; Van Delden, R. A.; Vicario, J.; Koumura, N.; Van Den Brom, C. R.; Meetsma, A.; Feringa, B. L. Light-Driven Rotary Molecular Motors on Gold Nanoparticles. *Chem. - A Eur. J.* **2008**, *14* (36), 11610–11622. https://doi.org/10.1002/chem.200800814.

(124) Klok, M.; Browne, W. R.; Feringa, B. L. Kinetic Analysis of the Rotation Rate of Light-Driven Unidirectional Molecular Motors. *Phys. Chem. Chem. Phys.* **2009**, *11* (40), 9124–9131. https://doi.org/10.1039/b906611j.

(125) Tirado-Rives, J.; Jorgensen, W. L. Performance of B3LYP Density Functional Methods for a Large Set of Organic Molecules. *J. Chem. Theory Comput.* **2008**, *4* (2), 297–306. https://doi.org/10.1021/ct700248k.

(126) Pritchard, B. P.; Altarawy, D.; Didier, B.; Gibson, T. D.; Windus, T. L. New Basis Set Exchange: An Open, Up-to-Date Resource for the Molecular Sciences Community. *J. Chem. Inf. Model.* **2019**, *59* (11), 4814–4820. https://doi.org/10.1021/acs.jcim.9b00725.

(127) Paier, J.; Marsman, M.; Kresse, G. Why Does the B3LYP Hybrid Functional Fail for Metals? *J. Chem. Phys.* **2007**, *127* (2), 024103. https://doi.org/10.1063/1.2747249.

(128) Sivasankar, M. Brief Review on Nano Robots in Bio Medical Applications. *Adv. Robot. Autom.* **2012**, *01* (01), 1–4. https://doi.org/10.4172/2168-9695.1000101.

(129) Li, J.; Esteban-Fernández de Ávila, B.; Gao, W.; Zhang, L.; Wang, J. Micro/Nanorobots for Biomedicine: Delivery, Surgery, Sensing, and Detoxification. *Sci. Robot.* **2017**, *2* (4), eaam6431. https://doi.org/10.1126/scirobotics.aam6431.

(130) Soto, F.; Wang, J.; Ahmed, R.; Demirci, U. Medical Micro/Nanorobots in Precision Medicine. *Adv. Sci.* **2020**, *7* (21), 2002203. https://doi.org/10.1002/advs.202002203.

(131) Wu, Z.; Troll, J.; Jeong, H.-H.; Wei, Q.; Stang, M.; Ziemssen, F.; Wang, Z.; Dong, M.; Schnichels, S.; Qiu, T.; et al. A Swarm of Slippery Micropropellers Penetrates the Vitreous Body of the Eye. *Sci. Adv.* **2018**, *4* (11), eaat4388. https://doi.org/10.1126/sciadv.aat4388.

(132) Garcia-Gradilla, V.; Sattayasamitsathit, S.; Soto, F.; Kuralay, F.; Yardımcı, C.; Wiitala, D.; Galarnyk, M.; Wang, J. Ultrasound-Propelled Nanoporous Gold Wire for Efficient Drug Loading and Release. *Small* **2014**, *10* (20), n/a-n/a. https://doi.org/10.1002/smll.201401013.

(133) Kim, K.; Guo, J.; Liang, Z.; Fan, D. Artificial Micro/Nanomachines for Bioapplications: Biochemical Delivery and Diagnostic Sensing. *Adv. Funct. Mater.* **2018**, *28* (25), 1705867. https://doi.org/10.1002/adfm.201705867.

(134) Vilela, D.; Cossío, U.; Parmar, J.; Martínez-Villacorta, A. M.; Gómez-Vallejo, V.; Llop, J.; Sánchez, S. Medical Imaging for the Tracking of Micromotors. *ACS Nano* **2018**, *12* (2), 1220–1227. https://doi.org/10.1021/acsnano.7b07220.

(135) Vilela, D.; Parmar, J.; Zeng, Y.; Zhao, Y.; Sánchez, S. Graphene-Based Microbots for Toxic Heavy Metal Removal and Recovery from Water. *Nano Lett.* **2016**, *16* (4), 2860–2866. https://doi.org/10.1021/acs.nanolett.6b00768.

(136) Donald, B. R.; Levey, C. G.; McGray, C. D.; Paprotny, I.; Rus, D. An Untethered, Electrostatic, Globally Controllable MEMS Micro-Robot. *J. Microelectromechanical Syst.* **2006**, *15* (1), 1–15. https://doi.org/10.1109/JMEMS.2005.863697.

(137) Hu, W.; Ishii, K. S.; Ohta, A. T. Micro-Assembly Using Optically Controlled Bubble Microrobots. *Appl. Phys. Lett.* **2011**, *99* (9), 094103. https://doi.org/10.1063/1.3631662.

(138) Ghosh, A.; Fischer, P. Controlled Propulsion of Artificial Magnetic Nanostructured Propellers. *Nano Lett.* **2009**, *9* (6), 2243–2245. https://doi.org/10.1021/nl900186w.

(139) Chen, X.-Z.; Hoop, M.; Mushtaq, F.; Siringil, E.; Hu, C.; Nelson, B. J.; Pané, S. Recent Developments in Magnetically Driven Micro- and Nanorobots. *Appl. Mater. Today* **2017**, *9*, 37–48. https://doi.org/10.1016/j.apmt.2017.04.006.

(140) Kagan, D.; Benchimol, M. J.; Claussen, J. C.; Chuluun-Erdene, E.; Esener, S.; Wang, J. Acoustic Droplet Vaporization and Propulsion of Perfluorocarbon-Loaded Microbullets for Targeted Tissue Penetration and Deformation. *Angew. Chemie Int. Ed.* **2012**, *51* (30), 7519–7522. https://doi.org/10.1002/anie.201201902.

(141) Ghosh, A.; Paria, D.; Rangarajan, G.; Ghosh, A. Velocity Fluctuations in Helical Propulsion: How Small Can a Propeller Be. *J. Phys. Chem. Lett.* **2014**, *5* (1), 62–68. https://doi.org/10.1021/jz402186w.

(142) Wu, Y.; Wu, Z.; Lin, X.; He, Q.; Li, J. Autonomous Movement of Controllable Assembled Janus Capsule Motors. *ACS Nano* **2012**, *6* (12), 10910–10916. https://doi.org/10.1021/nn304335x.

(143) BERG, H. C.; ANDERSON, R. A. Bacteria Swim by Rotating Their Flagellar Filaments. *Nature* **1973**, *245* (5425), 380–382. https://doi.org/10.1038/245380a0.

(144) de Gennes, P. G. Soft Matter. *Science (80-.).* **1992**, *256* (5056), 495–497. https://doi.org/10.1126/science.256.5056.495.

(145) Hu, J.; Zhou, S.; Sun, Y.; Fang, X.; Wu, L. Fabrication, Properties and Applications of

Janus Particles. *Chem. Soc. Rev.* **2012**, *41* (11), 4356. https://doi.org/10.1039/c2cs35032g.

(146) Takahara, Y. K.; Ikeda, S.; Ishino, S.; Tachi, K.; Ikeue, K.; Sakata, T.; Hasegawa, T.; Mori, H.; Matsumura, M.; Ohtani, B. Asymmetrically Modified Silica Particles: A Simple Particulate Surfactant for Stabilization of Oil Droplets in Water. *J. Am. Chem. Soc.* **2005**, *127* (17), 6271–6275. https://doi.org/10.1021/ja043581r.

(147) Glotzer, S. C.; Solomon, M. J. Anisotropy of Building Blocks and Their Assembly into Complex Structures. *Nat. Mater.* **2007**, *6* (8), 557–562. https://doi.org/10.1038/nmat1949.

(148) Berger, S.; Synytska, A.; Ionov, L.; Eichhorn, K.-J.; Stamm, M. Stimuli-Responsive Bicomponent Polymer Janus Particles by "Grafting from"/"Grafting to" Approaches. *Macromolecules* **2008**, *41* (24), 9669–9676. https://doi.org/10.1021/ma802089h.

(149) Wang, Y.-S.; Shao, D.; Zhang, L.; Zhang, X.-L.; Li, J.; Feng, J.; Xia, H.; Huo, Q.-S.; Dong, W.-F.; Sun, H.-B. Gold Nanorods-Silica Janus Nanoparticles for Theranostics. *Appl. Phys. Lett.* **2015**, *106* (17), 173705. https://doi.org/10.1063/1.4919454.

(150) Saini, S.; Kandasubramanian, B. Engineered Smart Textiles and Janus Microparticles for Diverse Functional Industrial Applications. *Polym. Technol. Mater.* **2019**, *58* (3), 229–245. https://doi.org/10.1080/03602559.2018.1466177.

(151) Liu, L.; Bai, T.; Chi, Q.; Wang, Z.; Xu, S.; Liu, Q.; Wang, Q. How to Make a Fast, Efficient Bubble-Driven Micromotor: A Mechanical View. *Micromachines* **2017**, *8* (9), 267. https://doi.org/10.3390/mi8090267.

(152) Gao, W.; Pei, A.; Wang, J. Water-Driven Micromotors. *ACS Nano* **2012**, *6* (9), 8432–8438. https://doi.org/10.1021/nn303309z.

(153) Palagi, S.; Mark, A. G.; Reigh, S. Y.; Melde, K.; Qiu, T.; Zeng, H.; Parmeggiani, C.; Martella, D.; Sanchez-Castillo, A.; Kapernaum, N.; et al. Structured Light Enables Biomimetic Swimming and Versatile Locomotion of Photoresponsive Soft Microrobots. *Nat. Mater.* **2016**, *15* (6), 647–653. https://doi.org/10.1038/nmat4569.

(154) García-López, V.; Chiang, P.-T.; Chen, F.; Ruan, G.; Martí, A. A.; Kolomeisky, A. B.; Wang, G.; Tour, J. M. Unimolecular Submersible Nanomachines. Synthesis, Actuation, and Monitoring. *Nano Lett.* **2015**, *15* (12), 8229–8239. https://doi.org/10.1021/acs.nanolett.5b03764.

(155) Bradley, L. C.; Stebe, K. J.; Lee, D. Clickable Janus Particles. *J. Am. Chem. Soc.* **2016**, *138* (36), 11437–11440. https://doi.org/10.1021/jacs.6b05633.

(156) Vauthier, M.; Schmutz, M.; Serra, C. A. One-Step Elaboration of Janus Polymeric Nanoparticles: A Comparative Study of Different Emulsification Processes. *Colloids Surfaces A Physicochem. Eng. Asp.* **2021**, *626* (June), 127059. https://doi.org/10.1016/j.colsurfa.2021.127059.

(157) Lubbe, A. S.; Böhmer, C.; Tosi, F.; Szymanski, W.; Feringa, B. L. Molecular Motors in Aqueous Environment. *J. Org. Chem.* **2018**, *83* (18), 11008–11018. https://doi.org/10.1021/acs.joc.8b01627.

(158) Fort, E.; Grésillon, S. Surface Enhanced Fluorescence. *J. Phys. D. Appl. Phys.* **2008**, *41* (1), 013001. https://doi.org/10.1088/0022-3727/41/1/013001.

(159) Teraoka, I. *Polymer Solutions*; John Wiley & Sons, Inc.: New York, USA, 2002; Vol. 67. https://doi.org/10.1002/0471224510.

(160) Berne, B. J.; Pecora, R. *Dynamic Light Scattering with Applications to Chemistry, Biology, and Physics*; Corporation, C., Ed.; Dover Publications INC.: Mineola, New York, 2000.

(161) Carlton, J. S. Propeller Blade Strength. In *Marine Propellers and Propulsion*; Elsevier, 2012; pp 397–414. https://doi.org/10.1016/B978-0-08-

097123-0.00019-8.

(162) Fischer, P.; Ghosh, A. Magnetically Actuated Propulsion at Low Reynolds Numbers: Towards Nanoscale Control. *Nanoscale* **2011**, *3* (2), 557–563. https://doi.org/10.1039/C0NR00566E.

(163) Dobitz, S.; Aronoff, M. R.; Wennemers, H. Oligoprolines as Molecular Entities for Controlling Distance in Biological and Material Sciences. *Acc. Chem. Res.* **2017**, *50* (10), 2420–2428. https://doi.org/10.1021/acs.accounts.7b00340.

(164) Amblard, M.; Fehrentz, J.-A.; Martinez, J.; Subra, G. Methods and Protocols of Modern Solid Phase Peptide Synthesis. *Mol. Biotechnol.* **2006**, *33* (3), 239–254. https://doi.org/10.1385/MB:33:3:239.

(165) Behrendt, R.; White, P.; Offer, J. Advances in Fmoc Solid-phase Peptide Synthesis. *J. Pept. Sci.* **2016**, *22* (1), 4–27. https://doi.org/10.1002/psc.2836.

(166) Pandey, A. K.; Naduthambi, D.; Thomas, K. M.; Zondlo, N. J. Proline Editing: A General and Practical Approach to the Synthesis of Functionally and Structurally Diverse Peptides. Analysis of Steric versus Stereoelectronic Effects of 4-Substituted Prolines on Conformation within Peptides. *J. Am. Chem. Soc.* **2013**, *135* (11), 4333–4363. https://doi.org/10.1021/ja3109664.

(167) To, W.-P.; Liu, Y.; Lau, T.-C.; Che, C.-M. A Robust Palladium(II)-Porphyrin Complex as Catalyst for Visible Light Induced Oxidative C-H Functionalization. *Chem. - A Eur. J.* **2013**, *19* (18), 5654–5664. https://doi.org/10.1002/chem.201203774.

Joakim HEISER

Intégration de moteurs moléculaires photo-activés dans des systèmes complexes pour le développement de matériaux actifs

Résumé

Cette thèse s'articule autour de l'intégration de moteurs moléculaires photo-activés en des systèmes complexes. Tout d'abord, nous nous sommes concentrés sur la mise à l'échelle de la synthèse d'un moteur tetrafonctionnalisé et orthogonalement protégé pour obtenir 40 g de produit en 12 étapes synthétiques.

Ensuite, nous avons cherché à augmenter la longueur d'onde d'irradiation nécessaire au fonctionnement du moteur pour passer de l'UV au visible en utilisant un photosensibilisateur à base de porphyrine. Nous avons démontré que cette unité était capable de réaliser un transfert d'énergie vers un moteur placé en solution mais également lorsque ce dernier est intégré comme centre de réticulation d'un gel chimique contractile.

Enfin, nous avons exploré le développement d'un nouveau mode de propulsion de nano-objets en fonctionnalisant la surface de nanoparticules de Janus avec des moteurs moléculaires. Les résultats préliminaires de diffusion statique de la lumière ont montré l'apparition d'un mouvement balistique lors d'une irradiation UV.

Mots-clés : chimie, synthèse organique, moteur moléculaire, porphyrine, photo-sensibilisateur, particule de Janus, système hors équilibre, transfert d'énergie, nano-robots.

Résumé en anglais

This thesis is centred on the integration of photoactivated molecular motors into complex systems. Firstly, we focused on scaling up the synthesis of a tetrafunctionalized and orthogonally protected motor to yield 40 g of product in 12 synthetic steps.

Secondly, we sought to increase the wavelength of irradiation required to operate the motor from UV to visible light using a porphyrin-based photosensitiser. We demonstrated that this photosensitiser was capable of transferring energy to a motor in solution and also when the latter is integrated as a cross-link into a contractile chemical gel.

Finally, we explored the development of a new mode of propulsion of nano-objects by functionalizing the surface of Janus nanoparticles with molecular motors. Preliminary static light scattering results showed the appearance of ballistic motion upon UV irradiation.

Keywords: chemistry, organic synthesis, molecular motor, porphyrin, photosensitizer, Janus particles, out-of-equilibrium, energy transfer, nano-bots.